Optimising Abdominal Computed Tomography: Radiation Dose, Contrast Media and Image Quality

Aho Fält, Tobias

2025

Document Version:
Publisher's PDF, also known as Version of record

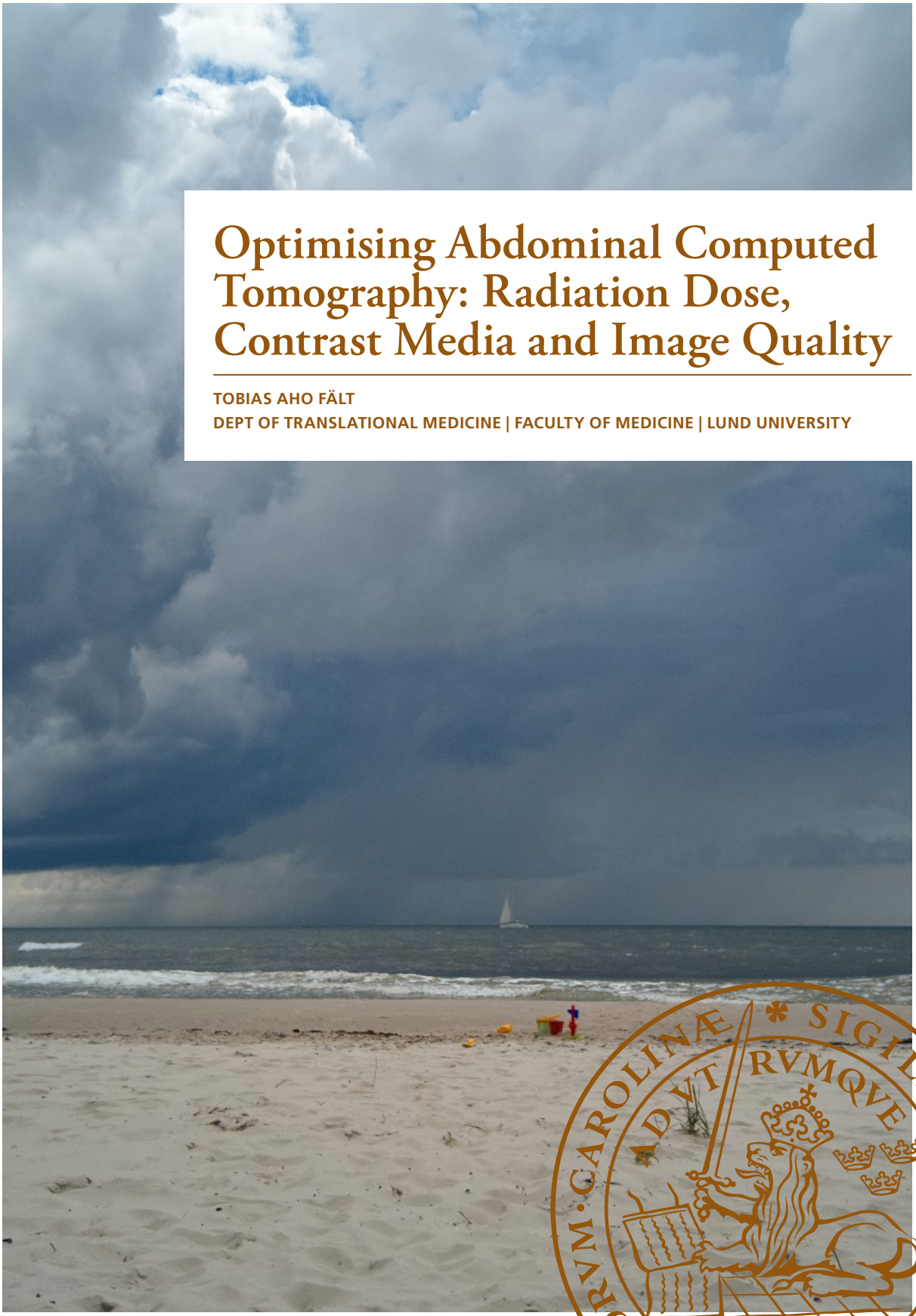

Optimising Abdominal Computed Tomography: Radiation Dose, Contrast Media and Image Quality

TOBIAS AHO FÄLT
DEPT OF TRANSLATIONAL MEDICINE | FACULTY OF MEDICINE | LUND UNIVERSITY

Optimising Abdominal Computed Tomography: Radiation Dose, Contrast Media and Image Quality

Optimising Abdominal Computed Tomography: Radiation Dose, Contrast Media and Image Quality

Tobias Aho Fält

LUND
UNIVERSITY

DOCTORAL DISSERTATION
Doctoral dissertation for the degree of Doctor of Philosophy (PhD) at the Faculty of Medicine at Lund University to be publicly defended on 24th of October at 13.00 in room 2005-2007, 2nd floor of the Medical Imaging department, Inga Marie Nilssons gata 47, at Skåne University Hospital in Malmö, Sweden

Faculty opponent
Professor Tomas Bjerner
Linköping University, Sweden

Organization: Department of Translational Medicine, Faculty of Medicine, Lund University

Document name: Doctoral dissertation **Date of issue:** 2025-10-24

Author: Tobias Aho Fält **Sponsoring organization:**

Title: Optimising Abdominal Computed Tomography: Radiation Dose, Contrast Media and Image Quality

Abstract:

Background: Abdominal computed tomography (CT) is a vital diagnostic tool in modern healthcare. Contrast media (CM)-enhanced CT carries risks of ionising radiation-induced cancer and kidney injury from iodinated CM in patients with pre-existing renal disease. Detecting small, low-contrast liver lesions, such as metastases, is challenging due to image noise. Recently introduced dual energy (DE) CT enables chemical element identification.

Aims: I. To assess image quality in a CT protocol balancing radiation and CM doses by age, reducing radiation for younger patients and CM for the elderly. II. To investigate attenuation properties of chemical elements at varying energy levels in DE CT, identifying candidates for dual-CM use with iodine. III. To evaluate the effect of simulated radiation dose reductions on liver metastasis detection and characterisation. IV. To explore detection of small, low-contrast lesions in low-dose phantom images using standard and sharp convolution kernels, with and without iterative reconstruction (IR).

Methods: I. Patients were stratified into four age groups, with radiation dose increasing and CM dose decreasing with age. Image quality was assessed objectively via contrast-to-noise ratio (CNR) and subjectively using visual grading characteristics (VGC) in an observer study. II. Alongside iodine, gadolinium (Gd), tantalum (Ta), tungsten (W), gold (Au), and bismuth (Bi) were examined across energy levels in a DE CT scanner. DE ratios were calculated, and material decomposition (MD) was performed using software. III. Patients with and without hypovascular metastases were included. Images with reduced doses (75%, 50%, 25%) were simulated by adding noise, and lesion detection/characterisation were analysed using JAFROC in an observer study. IV. Six phantoms, with and without lesions, were scanned at a low dose to produce high-noise images, with lesion detection assessed in an observer study, this time using JAFROC1.

Results and Conclusions: I. CNR remained consistent across groups, but subjective quality was poorer at the lowest radiation dose. Balancing radiation and CM is feasible, though noise impacts subjective quality. II. Ta, W, and Au are optimal for novel CM alongside iodine. III. Metastasis detection/characterisation was non-inferior at 75% dose, but benign lesion accuracy decreased; modest dose reduction is viable for younger patients. IV. A sharp kernel improved detection of small, low-contrast lesions, with no added benefit from IR.

Key words: Computed tomography, Radiation dose, Contrast media, Liver metastses, Material decomposition, Convolution kernels, Iterative reconstruction

Classification system and/or index terms (if any) Supplementary bibliographical

Language: English information **Number of pages:** 204

ISSN and key title: 1652-8220

ISBN: 978-91-8021-763-7

Recipient's notes Price Security classification

Signature Date 2025-09-16

Optimising Abdominal Computed Tomography: Radiation Dose, Contrast Media and Image Quality

Tobias Aho Fält

LUND
UNIVERSITY

Cover image by Tobias Aho Fält

Published by:

Department of Translational Medicine

Faculty of Medicine

Lund University

Lund 2025

ISBN 978-91-8021-763-7

ISSN 1652-8220

Printed in Sweden by Media-Tryck, Lund University
Lund, 2025

To my mother, Lena

In loving memory of my father, Lasse
and my mother-in-law, Aili

Table of Contents

“You've got to use the absolute minimum of mathematics but have a tremendous lot of intuition”

— Godfrey Hounsfield

Abstract

Background: Abdominal computed tomography (CT) is a vital diagnostic tool in modern healthcare. Contrast media (CM)-enhanced CT carries risks of ionising radiation-induced cancer and kidney injury from iodinated CM in patients with pre-existing renal disease. Detecting small, low-contrast liver lesions, such as metastases, is challenging due to image noise. Recently introduced dual energy (DE) CT enables chemical element identification.

Aims: I. To assess image quality in a CT protocol balancing radiation and CM doses by age, reducing radiation for younger patients and CM for the elderly. II. To investigate attenuation properties of chemical elements at varying energy levels in DE CT, identifying candidates for dual-CM use with iodine. III. To evaluate the effect of simulated radiation dose reductions on liver metastasis detection and characterisation. IV. To explore detection of small, low-contrast lesions in low-dose phantom images using standard and sharp convolution kernels, with and without iterative reconstruction (IR).

Methods: I. Patients were stratified into four age groups, with radiation dose increasing and CM dose decreasing with age. Image quality was assessed objectively via contrast-to-noise ratio (CNR) and subjectively using visual grading characteristics (VGC) in an observer study. II. Alongside iodine, gadolinium (Gd), tantalum (Ta), tungsten (W), gold (Au), and bismuth (Bi) were examined across energy levels in a DE CT scanner. DE ratios were calculated, and material decomposition (MD) was performed using software. III. Patients with and without hypovascular metastases were included. Images with reduced doses (75%, 50%, 25%) were simulated by adding noise, and lesion detection/characterisation were analysed using JAFROC in an observer study. IV. Six phantoms, with and without lesions, were scanned at a low dose to produce high-noise images, with lesion detection assessed in an observer study, this time using JAFROC1.

Results and Conclusions: I. CNR remained consistent across groups, but subjective quality was poorer at the lowest radiation dose. Balancing radiation and CM is feasible, though noise impacts subjective quality. II. Ta, W, and Au are optimal for novel CM alongside iodine. III. Metastasis detection/characterisation was non-inferior at 75% dose, but benign lesion accuracy decreased; modest dose reduction is viable for younger patients. IV. A sharp kernel improved detection of small, low-contrast lesions, with no added benefit from IR.

Populärvetenskaplig sammanfattning

Datortomografi, eller skiktröntgen som det också kallas, är en mycket viktig undersökningsmetod inom dagens sjukvård. Metoden bidrar med avgörande information i många olika situationer, såväl akuta sjukdomstillstånd som vid utredning av misstänkt eller känd allvarlig sjukdom, t.ex. cancer.

Vid datortomografiundersökning av buken är två faktorer avgörande för kvaliteten av de bilder röntgenläkaren skall bedöma – Hur mycket röntgenstrålning och mängden kontrastmedel som används. För lite röntgenstrålning ger brusiga bilder, vilket kan försvåra upptäckt av viktiga fynd, å andra sidan är röntgenstrålning en riskfaktor för cancer och måste alltid minimeras så mycket som möjligt. Risken för framtida cancer efter en datortomografundersökning är ytterst minimal för den enskilda patienten, men strålningen kan orsaka skador på arvsmassan i cellerna vilka, efter många år, kan utvecklas till en cancersjukdom.

Kontrastmedel i samband med datortomografi ges via en nål, direkt in i blodbanan. Därefter fördelas kontrasten i kroppens organ med blodcirkulationen. De kontrastmedel som idag används vid datortomografi innehåller grundämnet jod, vilket dämpar röntgenstrålarna och därför framträder ljust på bilderna. Den ökade kontrasten i bilden som kontrastmedel ger är avgörande för att kunna upptäcka många olika förändringar orsakade av sjukdom. Man kan likna det vid att man tänder en lampa som lyser upp datortomografibilderna. Även användning av kontrastmedel medför risk för biverkningar. Allergiska reaktioner kan uppstå, jodinnehållet kan påverka sköldkörteln, men den viktigaste risken är att jodkontrastmedel kan orsaka njurskada, främst hos patienter som redan har sjukdom eller skador i sina njurar och därigenom nedsatt njurfunktion.

När man utformar en datortomografiundersökning för en specifik patient är det därför viktigt att anpassa såväl mängden röntgenstrålning som vilken dos kontrastmedel som skall ges. Det är viktigt att med hög sannolikhet kunna besvara de frågeställningar som föreligger och samtidigt minimera de risker som undersökningen medför.

Jod är sedan lång tid tillbaka det grundämne som används i kontrastmedel via blodbanan i samband med datortomografi. Olika grundämnen har olika egenskaper vad gäller att dämpa röntgenstrålar. Ju större en atom är, desto mera energirik röntgenstrålning kan den dämpa. Energinivån i röntgenstrålarna som produceras i en

datortomograf är egentligen lite för höga för att jod på bästa sätt skall kunna dämpa dem. Till viss del kan man kompensera för detta genom att sänka energinivån så mycket som möjligt. Då blir jodkontrastmedlets nyans i bilderna ljusare, men dessvärre får röntgenstrålarna med låg energi samtidigt svårare att ta sig igenom kroppens vävnader varför bilderna får sämre kvalitet. Ett annat sätt att anpassa sig till energinivån i datortomografen hade varit att använda andra grundämnen i kontrastmedlet för att dämpa röntgenstrålarna. Denna idé är inte ny, det har under flera årtionden pågått forskning om nya kontrastmedel innehållande olika röntgentäta grundämnen. Det är dock inte känt vilket eller vilka grundämnen som är bäst lämpade för användning i dagens datortomografer. Utöver fördelen att alternativa kontrastmedel skulle kunna dämpa röntgenstrålarna mera effektivt, kan de också användas parallellt med jodkontrastmedel i en och samma undersökning. Moderna datortomografer kan känna igen olika grundämnen och om två kontrastmedel används samtidigt, t.ex. ett i blodbanan och ett annat i tarmen, skulle man kunna inhämta mera information på en och samma gång. Vilket eller vilka grundämnen som är bäst lämpade för användning parallellt med jod är dock inte fastställt.

Som beskrivits ovan medför exponering för röntgenstrålning en liten, men befintlig, risk för framtida cancerutveckling hos patienten. Det viktigaste är att alltid väga för och nackdelar för patienten med att över huvud taget genomgå en undersökning, att utföra en så kallad berättigandebedömning. I de flesta fall är nyttan med den kliniska informationen som undersökningen ger mycket större än den minimala risken för framtida cancer. Onödiga undersökningar bör dock undvikas och man skall överväga nyttan med datortomografi extra noga när det gäller unga patienter, då vissa vävnader är mera känsliga för röntgenstrålning när man är ung. Unga personer har även en längre kvarvarande livslängd, vilket ökar risken för att en skada på arvsmassan hinner utvecklas till cancer.

Datortomografi av buken är en mycket viktig undersökning vid utredning av många olika cancersjukdomar. En vanlig följdeffekt av olika cancerformer är metastaser, även kallat dottersvulster, i levern, vårt största inre organ. Metastaserna i levern kan vara svåra att upptäcka då de kan vara små och deras nyans i bildernas gråskala endast avviker diskret från omgivande levervävnad. En faktor som försvårar upptäckten är bruset i bilderna. Som nämndes ovan ökar bruset i bilderna när man använder sig av minskad mängd röntgenstrålning. Men var går gränsen? Hur mycket brus är för mycket för att vi med god säkerhet skall kunna upptäcka metastaserna? Om det skulle visa sig att man kan upptäcka metastaserna även när brusnivån är lite högre skulle de rutinmässiga undersökningarna kunna utföras med mindre mängd strålning.

Bruset i datortomografibilder avgörs dock inte enbart av stråldosen som använts. I en datortomografi sker väldigt avancerade matematiska beräkningar och procedurer där den ursprungliga informationen från de insamlade röntgenstrålarna omvandlas till bilder av patienten avbildad i olika plan. Ett steg inom dessa procedurer är en

matematisk filtrering av informationen. I detta steg kan olika typer av filter användas, vilket påverkar bildernas utseende. Filtren, som benämns med det engelska ordet ”kernels”, kan vara skarpa eller mjuka. Ett skarpt filter förbättrar upplösningen i bilderna och ger mera kantförstärkning av olika konturer i bilden, medan ett mjukare filter ger en lite mera suddig bild. Att använda ett skarpt filter medför dock också att mängden brus i bilden ökar och att bruset blir mera finkornigt. Ett mjukare filter ger lägre brusnivå och lite mera grovkornigt brus. Mjuka filter brukar användas vid undersökning av buk och lever. Det är dock oklart vilken typ av filter som är bäst när det gäller att upptäcka små metastaser i levern. Kanske kan ett skarpare filter på grund av den förbättrade upplösningen förbättra möjligheterna till upptäckt, trots att brusnivån samtidigt ökar?

Under det senaste decenniet har en helt ny typ av bildbearbetning inom datortomografi tillkommit. Metoden kallas ”iterativ rekonstruktion”, vilket betyder att bilderna bearbetas om och om tills bildkvaliteten uppnår en viss önskad nivå. Denna metod kan sänka brusnivån i bilderna ordentligt, men förändrar också upplösningen i bilderna och hur bruset ser ut, ungefär som när ett mjukt filter används. Det är därför oklart om och i så fall hur mycket användning av denna nya typ av bildbearbetning kan förbättra möjligheterna till upptäckt av metastaser i levern.

Denna doktorsavhandling består av fyra delarbeten, vars syfte och metodik är:

Delarbete I: Att undersöka om det går att balansera mängden röntgenstrålning och dosen av jodkontrastmedel mot varandra vid datortomografi av buken och erhålla likvärdig bildkvalitet. Genom att balansera dessa faktorer mot varandra skulle man kunna använda sig av olika undersökningsmetodik beroende på patientens ålder och på det viset minimera de risker som är viktigast för den aktuella åldern. Vid undersökning av unga patienter skulle stråldosen då kunna reduceras samtidigt som kontrastmedelsdosen ökas. För äldre patienter det omvända. Resultatet skulle bli lägre stråldos för unga patienter och att äldre patienter skulle få en lägre dos kontrastmedel, vilket är gynnsamt då äldre patienter oftare har nedsatt njurfunktion. Ett undersökningsprotokoll uppdelat i fyra åldersgrupper hade införts för akuta datortomografiundersökningar vid Skånes Universitetssjukhus i Malmö. Undersökningar av patienter i den yngsta åldersgruppen utfördes med halverad stråldos jämfört med en standardundersökning. Med stigande ålder ökades stråldosen samtidigt som kontrastmedelsdosen minskades. Den äldsta gruppen undersöktes med 50% ökad stråldos för att möjliggöra en 18%-ig sänkning av dosen kontrastmedel. 25 patienter i varje grupp (totalt 100) samlades in i efterhand och bildkvaliteten analyserades på två olika sätt: objektivt genom mätningar i bilderna och subjektivt genom att fyra röntgenläkare poängsatte hur väl olika organ och strukturer i buken avbildades.

Delarbete II: Att undersöka vilket eller vilka grundämnen som lämpar sig bäst som kontrastmedel att användas parallellt med jodkontrastmedel samt att se om ett

datorbaserat bildbehandlingsprogram därefter kan känna igen de olika grundämnena och färgkoda dem olika i bilderna. Flera olika grundämnen valdes ut genom att information om deras förmåga att bryta röntgenstrålar med olika energinivå inhämtades från tabeller. Jod, gadolinium, wolfram, tantalum, guld och vismuth valdes ut och lösningar av dessa ämnen undersöktes i en datortomograf med alla tillgängliga energinivåer. Utvalda kombinationer av grundämnen och energinivåer analyserades därefter i bildbehandlingsprogrammet för att se om de kunde färgkodas olika.

Delarbete III: Att undersöka om det går att minska mängden röntgenstrålning vid datortomografiundersökningar av buken, med bevarad förmåga att upptäcka metastaser i levern. En mjukvara som simulerar att en undersökning är utförd med lägre stråldos genom att lägga till brus i bilderna användes. Genom att använda redan befintliga bilder för att simulera undersökningar utförda med lägre stråldos undviker man risken att, som en del av studien, utföra undermåliga undersökningar. 39 patienter samlades in i efterhand, 19 med levermetastaser och 20 kontrollpatienter utan metastaser. Bilder motsvarande följande stråldosnivåer (jämfört standardprotokoll = 100%) simulerades: 75%, 50% och 25%. Möjligheten att upptäcka metastaser i levern bedömdes av fem röntgenläkare.

Delarbete IV: Att undersöka hur olika typer av brus i bilderna, skapade med olika filter, påverkar möjligheten att upptäcka små metastasliknande förändringar i ett konstgjort test-objekt. Test-objektet undersöktes i en datortomograf med väldigt lite röntgenstrålning för att skapa bilder med mycket brus. Därefter användes tre filter med olika grad av skärpa, utan och med ”iterativ rekonstruktion”. Möjligheten att upptäcka förändringarna bedömdes av fem granskare.

Resultat och bedömning:

I delarbete I visade den objektiva bedömningen av bildkvalitet likvärdiga resultat mellan alla åldersgrupper, oavsett hur röntgenstrålning och kontrastmedel balanserades mot varandra. Dessa resultat visar att det går att balansera röntgenstrålning och kontrastmedel och ändå erhålla likvärdig bildkvalitet. I den subjektiva bedömningen, där röntgenläkare betygsatte avbildningen av strukturer i buken fick dock den yngsta gruppen, där patienterna undersökts med lägst stråldos och brusnivån i bilderna var högst, sämre resultat än övriga grupper. Då objektiv och subjektiv bedömning inte överensstämmer avseende den yngsta gruppen är det svårt att avgöra om bildkvaliteten i den gruppen var tillräckligt bra. Det är möjligt att metoden som användes för subjektiv bildkvalitet inte riktigt lyckades bedöma den ljusare nyansen i bilderna från den ökade mängden kontrastmedel.

I delarbete II visade sig grundämnena tantalum, wolfram och guld vara optimala kandidater för kontrastmedel som kan användas samtidigt som jodkontrastmedel. Dessa grundämnen kunde urskiljas och färgkodas effektivt av bildbehandlings-programmet. Gadolinium och vismuth var däremot mindre lämpliga, då de ej kunde

separeras lika effektivt från jodkontrastmedlet. Det finns i dagsläget inga alternativa kontrastmedel baserade på de grundämnen som gav bäst resultat i studien, men forskning pågår och experimentella kontrastmedel är under utveckling.

I delarbete III visade resultaten att bilder med 75% simulerad stråldos, alltså motsvarande en minskning av mängden röntgenstrålning med 25%, vara lika bra som 100%-bilder för att upptäcka levermetastaser. Möjligheten att upptäcka metastaser var klart sämre i bilder med 50% och 25% stråldos. Redan vid 75% stråldos visade det sig dock vara svårare att skilja godartade förändringar från metastaser, en oönskad effekt som kan leda till onödig uppföljning av patienter.

I delarbete IV visade sig möjligheten att upptäcka små förändringar vara klart bättre i bilder skapade med det skarpaste filtret och tillägg av iterativa rekonstruktioner gav ingen ytterligare förbättring. Detta resultat är intressant då bilderna skapade med det skarpaste filtret även var de som hade den högsta brusnivån. Detta betyder sannolikt att det mera finkorniga bruset och den förbättrade upplösningen i bilderna underlättar upptäckt av metastaser trots att det samtidigt föreligger en ökning av den totala brusnivån.

Sammanfattningsvis visar resultaten från de fyra delarbetena att datortomografi-undersökningar av buken kan utföras på olika vis, där mängden röntgenstrålning och kontrastmedel balanseras mot varandra, med bevarad objektiv bildkvalitet. Upptäckt av levermetastaser är likvärdig vid undersökning med standardmässig och 25% reducerad stråldos. Tillsammans medför dessa resultat en möjlighet att undersöka unga patienter med lägre stråldos utan att riskera att man missar viktiga fynd. Att använda sig av skarpare filter i de bildskapande processerna kan ytterligare förbättra den diagnostiska bildkvaliteten. Slutligen är grundämnena tantalum, wolfram och guld optimala kandidater för att användas i framtida kontrastmedel, tillsammans med befintliga jodkontrastmedel.

List of papers

This thesis is based on the following papers, which will be referred to in the thesis by their Roman numerals, I-IV.

Paper I **Seesaw Balancing Radiation Dose and IV Contrast Dose: Evaluation of a New Abdominal CT Protocol for Reducing Age-Specific Risk**
Fält T, Söderberg M, Hörberg L, Carlgren I, Leander P
American Journal of Roentgenology, 200, 383 – 388, 2013

Paper II **Material Decomposition in Dual-Energy Computed Tomography Separates High-Z Elements From Iodine, Identifying Potential Contrast Media Tailored for Dual Contrast Medium Examinations**
Fält T, Söderberg M, Wassélius J, Leander P
Journal of Computer Assisted Tomography, 39, 975 – 980, 2015

Paper III **Simulated Dose Reduction for Abdominal CT With Filtered Back Projection Technique: Effect on Liver Lesion Detection and Characterization**
Fält T, Söderberg M, Hörberg L, Christoffersen C, Lång K, Abul-Kasim K, Leander P
American Journal of Roentgenology, 212, 84 – 93, 2019

Paper IV **Enhanced Detection of Low-Contrast Lesions in Low-Dose CT Using Sharper Convolution Kernels: A Phantom-Based Evaluation**
Fält T, Leander P, McMichael N, Senya S, Holmquist F, Lindvall H, Söderberg M
Manuscript

Related papers not included in this thesis

Post-Processing Image Filtration Enabling Dose Reduction in Standard Abdominal CT
Leander P, Söderberg M, Fält T, Gunnarsson M, Albertsson I
Radiat Prot Dosimetry. 139(1-3), 180 – 5, 2010

80-kVp Hepatic CT to Reduce Contrast Medium Dose in Azotemic Patients: a Feasibility Study
Holmquist F, Söderberg M, Nyman U, Fält T, Siemund R, Geijer M
Acta Radiol, 61(4), 441 – 449, 2020

Can Iterative Reconstruction Algorithms Replace Tube Loading Compensation in Low kVp Hepatic CT? Subjective versus Objective Image Quality
F Holmquist F, Söderberg M, Nyman U, Fält T, Siemund R, Geijer M
Acta Radiol Open. 9(3), 1 – 9, 2020

Author's contribution to the Papers

Paper I

I contributed to the planning of the study evaluating an existing examination protocol, prepared the ethical committee application, recruited patients, and participated in image reading and data analysis. Additionally, I wrote the manuscript and managed the publication process.

Paper II

My contributions included study design, collaboration on experimental object production, image acquisition and analysis, manuscript writing, and publication process management.

Paper III

I participated in study planning, drafted the ethical committee application, identified eligible patients, coordinated the multiple-reader study, contributed to data analysis, wrote the manuscript, and handled the publication process.

Paper IV

I oversaw all aspects of planning and execution, including phantom fabrication, image acquisition, and post-processing. I managed the multiple-reader study, performed data analysis and wrote the manuscript.

Declaration of generative artificial intelligence usage

The entirety of the text has been written by the author. Generative artificial intelligence (AI) tools, ChatGPT and Grok, were used solely for language refinement and style improvement. Additionally, a limited number of non-scientific illustrations were generated using the same tools.

Abbreviations

ADMIRE	Advanced Modeled Iterative Reconstruction
AKI	Acute kidney injury
ALARA	As low as reasonably achievable
ANOVA	Analysis of variance
AUC	Area under the curve
CIN	Contrast induced nephropathy
CKD	Chronic kidney disease
CM	Contrast medium
CNR	Contrast-to-noise ratio
$CTDI_{vol}$	Volume computed tomography dose index
DE	Dual energy
DLP	Dose-length product
eGFR	Estimated glomerular filtration rate
ERR	Excess relative risk
FBP	Filtered Back Projection
FOM	Figure-of-merit
HOCM	High-osmolar contrast media
HU	Hounsfield unit
ICC	Intraclass correlation coefficient
ICRP	International Commission on Radiological Protection
IR	Iterative reconstructions
JAFROC	Jackknife alternative free-response receiver operating characteristics
keV	Kiloelectronvolt
kVp	Peak kilovolt
LOCM	Low-osmolar contrast media
LNT	Linear no threshold
LSS	Life span study

MD	Material decomposition
MTF	Modulation transfer function
NPS	Noise power spectrum
PCDT	Photon counting detector technology
PSM	Propensity score matching
ROC	Receiver operating characteristics
SNR	Signal-to-noise ratio
VGC	Visual grading characteristics
ViewDEX	Viewer for digital evaluation of X-ray images
Z	Atomic number

Introduction

History of Computed Tomography

In 1971, at Atkinson Morley Hospital in London, a radiologist carefully removes the Polaroid camera from the small screen of the viewing unit attached to the first experimental computed tomography (CT) scanner. The camera has just captured an image displayed on the screen: an axial slice of a patient's head with a resolution of 80 x 80 pixels.

The image was produced two days after the patient's examination, during which she positioned the top of her head inside the water-filled gantry of the scanner. Each of the approximately eight slices took around five minutes to acquire. The delay between acquisition and final image production is due to the computational demands of image reconstruction, which had to be performed on an offsite mainframe computer—the only available system capable of handling such demanding calculations (1–4).

The difference between the scenario described above and today's incredibly fast CT scanners is remarkable—modern systems can scan large sections of a patient's body in just a few seconds and produce high-resolution multi-planar images almost instantly. In the following section the extraordinary progress of CT science and technology in the last half century will be briefly described, focusing on a few particularly influential individuals and important developments.

The two men being primarily recognised for the invention of computed tomography are Sir Godfrey Hounsfield and Allan MacLeod Cormack, sharing the 1979 Nobel Prize in Physiology or Medicine.

Allan MacLeod Cormack was a Cambridge-educated, South African physicist starting his academic career at Cape Town University and after a few years moving to Tufts University in the US. Here he got an opportunity to work in collaboration with the Harvard Cyclotron Laboratory. While the primary focus of Cormack's research was the polarization and scatter of proton beams, he pursued a long-standing side project in his personal time. This project stemmed from a problem he encountered during a brief period overseeing radiotherapy at Groote Schuur Hospital in Cape Town. To optimize radiation treatment, Cormack realized that knowledge of the attenuation properties of the tissues surrounding the target organ would be valuable. This led Cormack to

perform experiments using a basic setup with a gamma ray emitting Cobalt-60 source and a Geiger counter as the detector. The objects scanned in this experimental setup were discs made from different materials. The discs were first horizontally translated in 41 positions through the beam of gamma rays, whereafter the disc was rotated and the procedure repeated at 25 positions, 7.5 degrees apart. The data from these experiments gave Cormack the means to eventually find a solution to the "line integral problem" as he named it, i.e. to establish a mathematical solution making it possible to calculate the attenuation coefficients of the different materials within the disc using only data from external readings. Cormack assumed a solution to this mathematical problem already existed and he searched the literature as well as asking prominent physicists and mathematicians at prestigious Universities, but to no avail (5).

Cormack´s method was published in an article named "Representation of a Function by Its Line Integrals, with some Radiological Applications" in 1963 (5,6).

However, it is now recognized that earlier scientific research in diverse fields, including mathematics, astronomy, and electron microscopy, had already explored similar problems (3–5). The publication which today is considered most important is "Über die Bestimmung von Funktionen durch ihre Integralwerte längs gewisser Mannigfaltigkeiten" by Radon in 1917 (7). Radon describes a mathematical procedure now called the "Radon transfer" which, just like Cormack, describes a function, or object, by its line integrals from all angles. The Radon transfer is a foundation of image reconstruction techniques still used in computed tomography - more on that in a later section. Rediscovered after many years was also the work by Tetel'baum and colleagues in the Soviet Union in the 1950s. This group had theoretically and experimentally developed a working version of computed tomography (8). The research never led to any clinical implementations, though, and knowledge of its existence did not reach the western world until much later.

The person who undoubtedly played the most important part in the actual development of early computed tomography scanners was the British engineer Godfrey Hounsfield. Hounsfield was employed at EMI Ltd in London and had previously led EMI's development of the EMIDEC 1100 computer. In the late 1960s, after working several years on an eventually discontinued project trying to develop a new type of computer memory storage, Hounsfield was given freedom to explore ideas for new products. He was intrigued with the problem of determining the contents of a box by examining it from the outside. This led to Hounsfield inventing a computational method for determining individual values within the cells of small matrices such as 3 x 3 and up to 8 x 8, from the sums of horizontal, vertical and diagonal rows. Even if Hounsfield, just like Cormack before him, was unaware of the earlier research he soon realized that the most promising application for his ideas was to use X-ray in a new way, better determining the internal structures of a human (9). In a fascinating document, a project proposal asking for external funding, Hounsfield in 1968 describes

theories and possible practical applications of CT with astonishing clarity. The document contains description of his computational reconstruction method, as well as sketches of how a tumour within a body might be depicted with CT. Hounsfield even introduces the concept of "windowing" to be able to handle different levels of contrast within images (3,9).

At the time, many radiologists struggled to recognize the potential of Hounsfield's ideas. In radiology, detail resolution had long been considered one of the most critical image quality criteria. As a result, many radiologists could not see the value of Hounsfield's vision: lower-resolution images capable of accurately describing the X-ray properties of internal structures (2,3). This serves as an important lesson: we must remain curious and receptive to new ideas and technologies, even when their potential benefits are not immediately obvious. In today's world, where technological advancements occur at an unprecedented pace, this kind of open-mindedness is more crucial than ever. Eventually, Hounsfield struck a collaboration with neuroradiologist James Ambrose at Atkinson Morley Hospital who could envision the revolutionary potential in the technique.

Figure 1 EMI Record label

Contrary to the legend, the work of Godfrey Hounsfield's team at EMI, developing the first CT-scanners, had a very tight budget and did not receive any funds from EMI's music division. Copyright: KarleHorn From: https://commons.wikimedia.org/wiki/File:Label_LP_Sgt_Pepperjpg.jpg.

Another problem during this early development phase was the severely constrained budget for the project. EMI, at the time, did not have a division for medical technology

and the available funds at the research lab were limited. By using technical parts left over from earlier projects, keeping the team small and eventually securing some financial support from the government (Department of Health and Social Security) it was possible to carry on and in 1971 the first prototype of a clinical CT scanner, the one described in the first paragraph of this text, was produced. The famous first clinical examination, of a patient with a cystic brain lesion, was performed on October 1st 1971 (9).

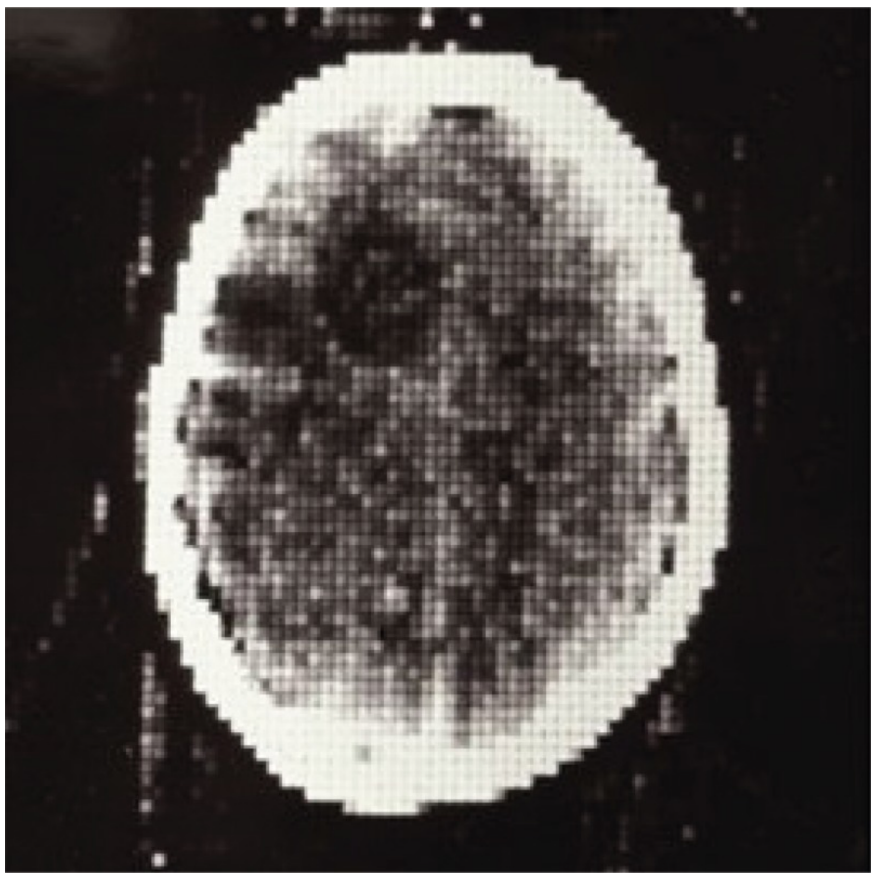

Figure 2 Early clinical CT scan of a brain with a lesion

One of the first images produced by the CT-scanners developed at EMI, revealing a cystic lesion within the right frontal lobe. Copyright Oliver Taubmann, Martin Berger, Marco Bögel, Yan Xia, Michael Balda, and Andreas Maier. Reproduced under Creative Commons CC BY-SA 4.0.

Figure 3 EMI Brain scanner
One of the first clinically used CT-scanners, located at Atkinson Morley Hospital, London in 1971. To reduce the attenuation difference between the head and its surroundings the top of the head is placed in a rubber cap within the gantry, surrounded by water. Copyright: Science Museum Group. EMI CT Brain Scanner. 1980-811 Science Museum Group Collection Online. Accessed 13 September 2025. https://collection.sciencemuseumgroup.org.uk/objects/co134790/emi-ct-brain-scanner. Reproduced under Creative Commons CC BY-SA 4.0.

As groundbreaking as Hounsfield's purely computational image reconstruction method was, it had a serious flaw - it was computationally demanding, making the reconstruction process on the computers of the era excruciatingly slow. Fortunately, there were other parallel developments that made the first commercial CT, the EMI Mark 1, possible, namely the launch of the "minicomputers" and more importantly the development of the filtered back projection (FBP) image reconstruction technique. Minicomputers were hardly small by today's standard, being the size of a cupboard, but compared to the off-site mainframe computers used prior, they made possible the commercial product of a CT scanner with its adjoining computer (3). FBP technique will be discussed in more detail in a later section, but it was a leap forward in terms of the reduced computational demand from image reconstruction, reducing the time needed manifold. It is not easy to establish exactly how FBP came into being as similar techniques were developed simultaneously but important work was performed by Ramachandran who in 1971 published mathematical works on how to reconstruct the structure of an object from its "shadowgrams" from different angles.(10) Soon thereafter FBP was demonstrated for positron images by Chesler et al and the

mathematician Christopher Lemay, working with Hounsfield at EMI, is often credited with creating the version used in the EMI scanners (1,11).

EMI presented their first commercial CT scanner at the annual meeting of the Radiological Society of North America (RSNA) in 1972 to a warm reception, and several orders of scanners were received (9).

Hounsfield and Ambrose each published one article in 1973 describing the system and early experiences from the clinical cases examined (12,13). From this point on a multitude of different producers entered the field of CT, small firms as well larger players already established in the field of radiology, and the progress accelerated further.

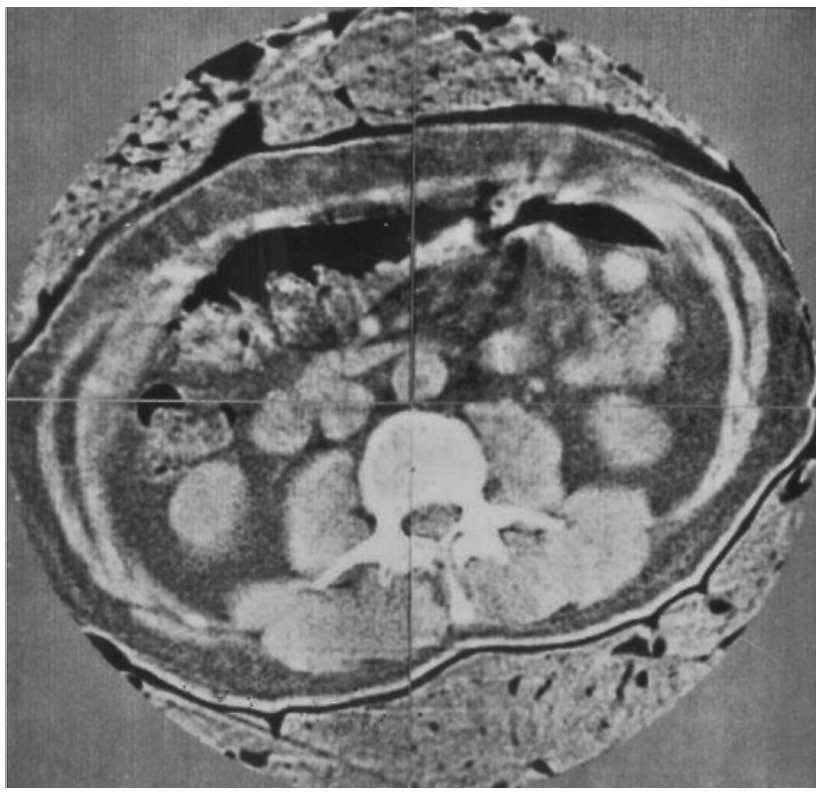

Figure 4 CT-scan of Godfrey Hounsfield's abdomen
A "portrait" of the main inventor of the CT-scanner is called for and what can be more appropriate than an image produced by his invention. This is one of the earliest CT-images of a human abdomen and was presented by Hounsfield himself at an international symposium in Bermuda in 1975. Copyright: Beckmann EC. CT scanning the early days. The British Journal of Radiology. 2006 Jan;79(937):5–8. Available from: https://academic.oup.com/bjr/article/79/937/5-8/7443496 Reproduced with permission from British Institute of Radiology.

CT-Scanner Generations

First generation

Early EMI scanners were so-called first-generation CT scanners as they were constructed with a pencil X-ray tube emitting a single ray through the object with a single detector on the opposite side of the gantry. Using the translate-rotate technique, the tube and detector were moved stepwise across the object measuring the linear attenuation one position at a time. Readings were made in 160 positions along the object after which the tube and detector setup was rotated one degree, and the process repeated. This way the scanner worked its way around the half circumference of the gantry producing in total 160 x 180 measurements per slice, a process of around 5 minutes (3,4). The X-ray tube had tube potential values of 100 – 140 kVp and the detector was a sodium iodide scintillator coupled to a photomultiplier tube. While still being considered first generation, the EMI scanners were soon equipped with two separate detectors placed on top of each other in the cranio-caudal direction, facilitating the data collection of two slices at one time (3).

The scanners of this first generation are long gone, but knowledge and understanding of these systems are still important as its basic geometry makes the principles of CT physics and reconstruction techniques more approachable as compared to the more complex later generations.

Second generation

The second generation of CT scanners added more detectors, placed in a row along the slice and collecting measurements from a fan shaped beam. For example, if the scanner had 6 detectors and a fan beam with an angular width of 6 degrees, each position of the tube and detectors along the circumference collected 6 rays traversing the object at different angles. In a first-generation scanner all these rays would have been measured one at a time. Therefore, in this example, the gantry positions can be reduced by a factor of 6, substantially decreasing the scan time (4,9). Within this second generation of scanners, the first whole body scanners were released. As the scan time was still long, scanning of the thorax and abdomen was very difficult due to e.g. breathing motion (2,3).

Third generation

If the first two generations of CT scanners were quite similar, the third generation was a big leap forward and made possible several succeeding developments. The defining attribute of the third generation was that the detector row now was so wide that the fan beam covered the whole object. This rendered the “translate”-part of translate-rotate obsolete (4). The now multiple detector elements were initially of the ionization chamber type, e.g. Xenon detectors. Siemens then introduced a detector constructed

from a solid scintillator coupled to a photodiode and this technique has since been the most commonly used type – at least until the recent emergence of photon counting detectors (3). More on detector technique later.

Slip ring and multislice scanning

There were fourth- and fifth- generation CT scanners, but they never became dominant and modern scanners are based on the third generation, with several important improvements. Among the most significant improvements are the slip ring technology and multislice scanning. The slip ring is a technical part within the gantry of a CT scanner transferring power to the X-ray tube and collecting data from the detector in a continuous manner obviating the need for cables. In this way the slip ring facilitates uninterrupted rotation of tube and detector as compared to the stop-and-reverse procedure needed when cables are used. The slip ring thereby opened the door for helical scanning covering larger part of the body in a single scan (1,4).

Multislice scanning is based on the introduction of multiple rows of detectors along the length of the patient, examining more "slices" at the same time. During the 1990's and 2000's the number of detector rows steadily increased to eventually reach todays levels of up to around 320 slices. These large numbers of detector rows enable very thin slices, to the sub-millimetre level. Thin slices in turn make the voxels (or volumetric pixels) of CT data isotropic and image reformation in multiple planes is possible, a functionality taken for granted in today's radiology practice (14). Even more important in the context of this thesis is how helical, multislice scanning, by covering a larger anatomic area in a shorter time, opened new avenues for the use of intravenous contrast media in abdominal and urological imaging. As a scan covering the liver or kidneys could be performed in less than 25 seconds it was possible, for most patients, to perform a scan during a single breath hold, minimizing motion artefacts. The improved temporal resolution also facilitated the introduction of multiphase examinations, capturing different contrast media phases, i.e. scanning performed as the peak of the contrast enhancement is situated within specific blood vessels and/or tissues. The most prominent challenge complicating the multislice scanning was that the fan beam now was turned into a cone beam adding new planes in which the radiation passes through the patient. The geometry to be handled by the image reconstruction algorithms hence became much more complicated. However, after a few years even this challenge was overcome and the reconstructions worked well even when handling data from multiple rows of detectors (14).

Figure 5 Modern CT-scanner
Copyright: Tomáš Vendiš. Reproduced under Creative Commons CC BY-SA 4.0.

Basic X-ray Physics

X-ray is a type of electromagnetic radiation with short wavelength and high energy. On the electromagnetic spectrum X-ray is located between ultraviolet light and gamma rays, with energies of about 10 – 150 kiloelectronvolt (keV).

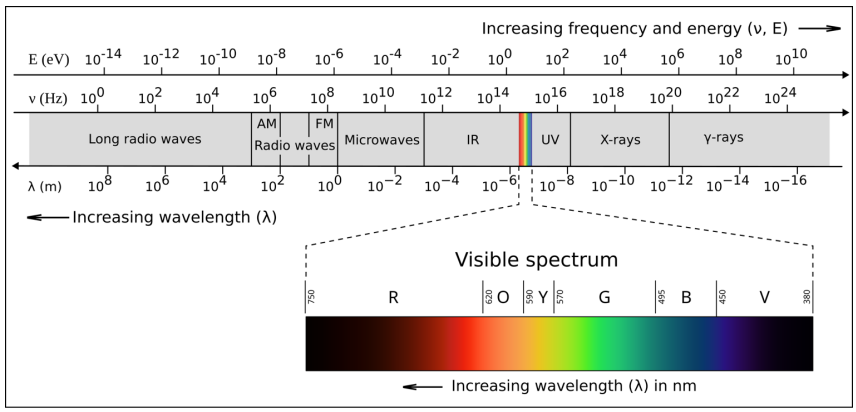

Figure 6 Electromagnetic spectrum
The electromagnetic spectrum extends from long radio waves, with low frequency and energy, to gamma radiation, with the highest frequency and energy levels. X-rays are positioned between ultraviolet light (UV) and gamma rays. The relevant energy range for photons used in CT imaging is 20–150 keV (note the use of the unit eV in the figure, hence CT photons fall within the range of 2×10^4–1.5×10^5 eV). Copyright: Philip Ronan. Reproduced under Creative Commons CC BY-SA 2.5.

X-rays were discovered by German physicist Wilhelm Conrad Röntgen in 1895. Mystified by the radiation he had produced in his laboratory, he named it X-ray – a name it still goes by in large parts of the world. However, in several European countries it is called "Röntgen rays" to honour its discoverer.

Just like light, X-rays are considered to travel through space and interact with particles in small units of energy, called photons. X-ray is a type of ionizing radiation as it has the potential for ejecting electrons from atoms it interacts with, creating positive ions. Different types of interaction between electrons, atoms, photons and transfers of energy are involved in the creation of X-rays as well as with how they interact with matter it passes through. For this reason, the following section will be an overview of the basic physics underlying X-ray (15).

Atomic structure

Atoms comprise a nucleus containing positively charged protons and neutral neutrons, with the atomic number (Z) determined by the number of protons. Surrounding the nucleus are negatively charged electrons, equal in number to the protons, arranged in shells. Contrary to the schematic representations familiar to all readers, atomic nuclei are exceedingly small, with a diameter of about 1/10,000th of the atom. If you picture the nucleus as a 1 cm marble, the nucleus of the neighbouring atom would be about 100 m away, roughly the length of a football field. This vast inter-nuclear space contains the electrons organised in various shells, exhibiting binding energies that diminish with increasing distance from the nucleus. The innermost shell, known as the K-shell, accommodates two tightly bound electrons. Subsequent shells, designated L, M, and so forth, house progressively greater numbers of electrons. The electrons in the outermost shell are weakly bound, and in certain metals, they have the potential to move freely (15).

X-ray generation

X-rays are generated by accelerating electrons and directing them to interact with a target material. This acceleration is achieved by applying a high electric potential, or voltage, between the cathode and anode in an X-ray tube. In computed tomography (CT), tube potentials typically range from 70 to 140 kVp, imparting maximum energies of 70–140 keV to the electrons striking the anode. The primary interactions producing X-rays are bremsstrahlung and characteristic radiation, though the process is highly inefficient, with over 99% of the energy dissipated as heat (15,16).

Bremsstrahlung is when an electron, travelling with high velocity and high energy, its trajectory is impacted by the attracting force of an atomic nucleus. As the electron changes direction, it loses energy, which is emitted in the form of an X-ray photon. Photons produced by bremsstrahlung can have any level of energy from the maximum (at the keV corresponding to the kVp-level), when an electron passes very close to a

nucleus and loses all of its energy, to zero. There are very few interactions producing maximum energy photons with increasing number of photons as the energy decreases (15,16).

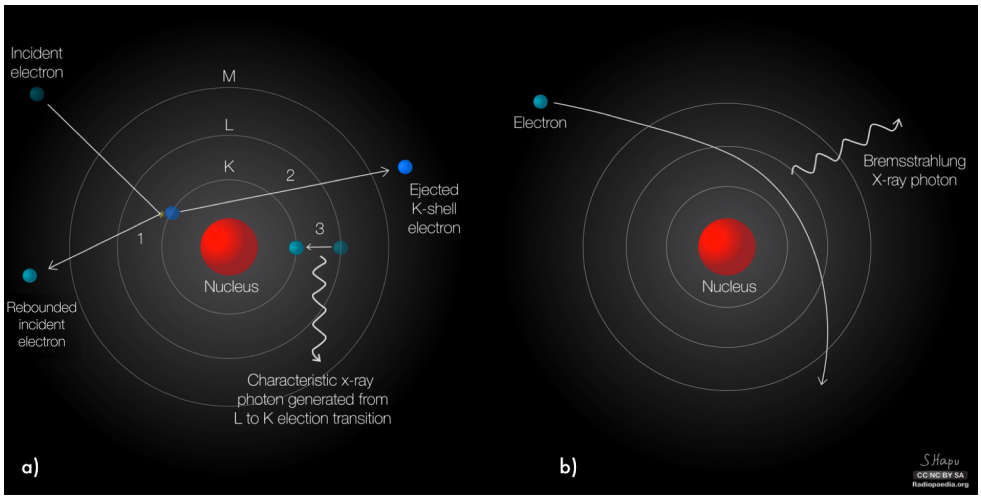

Figure 7 X-ray generation
The two primary interactions of accelerated incident electrons with target atoms: (a) Characteristic radiation, where the electron ejects an inner-shell electron, ionizing the atom; an outer-shell electron then fills the vacancy, emitting an X-ray photon with energy equal to the shell difference. (b) Bremsstrahlung, where the electron is deflected by the nucleus, decelerating and emitting a photon; the continuous X-ray spectrum arises from variable energy losses in this process. Copyright Hapugoda S, Characteristic radiation (diagram). Radiopaedia.org doi.org/10.53347/rID-51796 and Bremsstrahlung radiation (diagram) doi.org/10.53347/rID-51794.

Characteristic radiation occurs when an incident electron displaces a K-shell electron from the target atom, provided its energy surpasses the K-shell binding energy. This process ionises the atom, leaving it in an excited state with a vacancy in the K-shell. The vacancy is filled by an electron from an outer shell "dropping" into the position, releasing energy in the process. This energy is emitted as X-ray radiation at a specific energy level, corresponding to the difference in binding energy between the two shells involved (measured in keV). The incident electron and the ejected electron then share the remaining energy, minus the binding energy (15,16).

X-ray Spectrum

The resulting X-ray spectrum, unique to the anode material, combines bremsstrahlung and characteristic photons. Bremsstrahlung production scales with the square of the atomic number (Z) of the anode material. Tungsten, also known as wolfram (W; Z = 74), is often used due to its high Z and heat resistance. The X-ray spectrum of W is displayed in Figure 8. The peaks of the curve are formed by characteristic radiation,

representing the energy difference between the K-shell and the L- and M-shells respectively. The intensity of X-rays is reduced at the lower end of the energy spectrum due to filtration, which is partly attributable to the anode material and other components of the X-ray tube, as well as intentionally added filtration. Filtering out low-energy photons is advantageous, as they contribute to the radiation dose received by the patient without possessing sufficient energy to reach the detector (15,16).

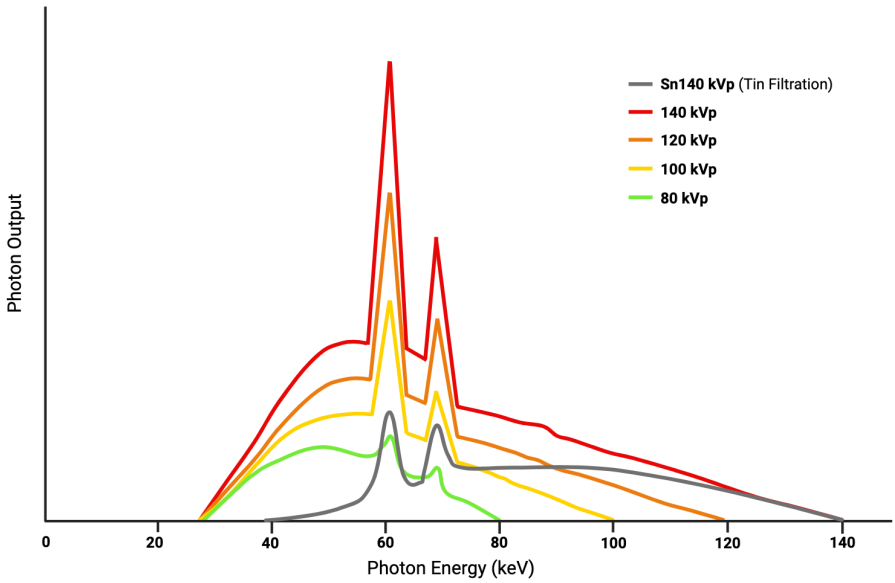

Figure 8 X-ray energy spectra at different peak kilovolt (kVp)-levels.
Schematic of X-ray spectra from a CT scanner at varying kVp settings. Decreasing kVp lowers the maximum photon energy, reduces mean energy, and substantially decreases total number of photons (area under curve) due to fewer effective electron-target interactions and lower photon yield. Adding tin (Sn) filtration removes low-energy photons, hardening the beam and raising the mean energy. Image created in BioRender. https://BioRender.com/65wsrbg.

X-ray Interaction with Matter

The interactions of X-rays with matter are similar to the processes involved in their production. In this context, highly energetic X-ray photons are incident, encountering a wide variety of target elements. X-ray photons within the energy spectrum employed in computed tomography (CT) interact with matter through two primary mechanisms: the photoelectric effect and Compton scatter (15,16).

Photoelectric Effect

The photoelectric effect occurs when a photon, possessing energy equal to or exceeding the binding energy of an inner-shell electron, transfers its entire energy to the electron, resulting in its ejection and ionisation of the atom. During this process, the photon is annihilated and will not reach the detector. The probability of this interaction peaks when the photon energy aligns with the binding energy of an electron shell within an atom. In CT, the binding energies of the K-shells of different elements are the most relevant, and consequently the K-edges the most important energy levels. Below the K-edge, the interaction probability diminishes sharply as the photon lacks sufficient energy to dislodge an electron; for instance, iodine's interaction likelihood drops to one-sixth just below its K-edge (17). At energies above an edge the probability for interaction is inversely proportional to the cube of the increasing photon energy. For low-Z elements prevalent in human soft tissues (such as oxygen, carbon, hydrogen, and nitrogen) the photoelectric effect is minimal due to their low K-edge energies, which fall well below typical CT X-ray spectra. Conversely, this interaction is the predominant mechanism for larger atoms with higher Z values.

The binding energies of other shells, located at much lower keV levels, are of lesser relevance in this context (15,16).

Compton Scatter

Compton scatter occurs when a photon collides with a loosely bound or free electron, transferring energy and scattering at an angle. The photon retains significant energy post-interaction, potentially interacting again or exiting the patient. This process is independent of binding energies, instead it is the electron density of the material that determines the likelihood of interaction. Compton scatter is the dominant type of interaction when photon energy is far above the K-edge, thus for most elements in the upper range of the X-ray spectrum and at levels as low as 30 keV for human soft tissue (15,16).

X-ray Tube and Detector

X-ray tube

The X-ray tube accelerates electrons from the cathode to the anode, where interactions generate X-rays. The anode, i.e. the positively charged pole, as described above, is typically made from W. The negatively charged cathode, heated by an independent circuit, releases electrons via thermal energy, with temperature and electron flux controlled by the cathode current. The generator applies the high voltage (70–140 kVp), driving electron acceleration. The other commonly adjusted setting of an X-ray tube is the tube load in milliampere-seconds (mAs). This is a measure of the number

of electrons accelerated across the tube and thereby the number of X-ray photons produced. The adjustment of the tube load is a complex interplay of the cathode current determining the number of available electrons and the tube potential. Modern X-ray tubes feature rotating anodes to distribute heat over a larger area. The angled anode surface aligns the X-ray beam perpendicular to the electron flow. The cathode and anode operate in a vacuum within a housing, ensuring efficient electron movement (15).

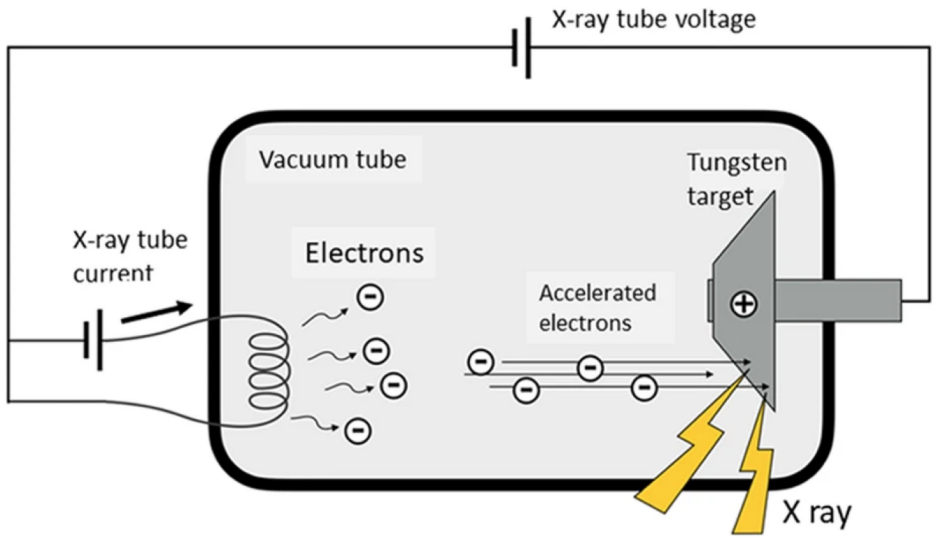

Figure 9 The CT X-ray tube

Schematic of the X-ray tube in a CT scanner. The anode ("Tungsten target") is a rotating disc to disperse heat generated during X-ray production. The cathode, a separate electrical circuit, heats a filament (coil in the diagram) to emit electrons. The emitted electrons are accelerated across the vacuum towards the anode by the tube potential ("X-ray tube voltage"). The flow of accelerated electrons is the tube current. X-ray photons, produced at the anode, are depicted in yellow. Used with permission of Springer Nature BV, from Tatsugami F, et al, Dual-energy CT: minimal essentials for radiologists. Vol. 40, Japanese Journal of Radiology. Springer; 2022. p. 547–59.

Energy-integrating detector technology

Like the X-ray tube, the function of the detector relies on the principles of X-ray physics. In contemporary CT scanners, the detector is made from solid scintillating material, most commonly gadolinium oxysulfide. When X-ray photons that have traversed the patient strike this material, photoelectric interactions occur, ejecting photoelectrons that travel a short distance within the scintillator. These photoelectrons excite neighbouring atoms, which subsequently return to their ground state, emitting visible light in the process. Essentially, the scintillating material converts X-ray photons into visible light (16,18). The detector consists of numerous small elements, each less than 1 millimetre (mm) in size, separated by reflective, non-transparent walls. These

walls minimise crosstalk between elements and direct the emitted light photons towards a photodiode, which converts the light into an electrical signal. The detector integrates the photodiode and the subsequent data acquisition system (DAS) (including amplifiers and analogue-to-digital converters) into a single chip attached to the scintillating material. Additional important parts of the detector are the collimator blades, mitigating noise from scattered photons arriving at an angle (16,18).

This type of detector is classified as energy-integrating, as it accumulates the energy from multiple X-ray photons striking a single detector element over the duration of a projection (typically less than one millisecond), without distinguishing the energy of individual photons. As a result, low-energy X-ray photons contribute disproportionately less to the overall signal, thereby diminishing the information from the lower end of the X-ray spectrum (18).

A limiting factor in the efficacy of this detector design is the necessity for non-transparent walls separating the elements. As these walls must maintain a certain width, they occupy a portion of the potential detector surface area, rendering photons striking these regions ineffective in generating a signal (18). The electronic noise has been reduced considerably by integrating all electrical parts in the detector but can still impair image quality as the number of X-ray photons diminishes in very low radiation dose scans.

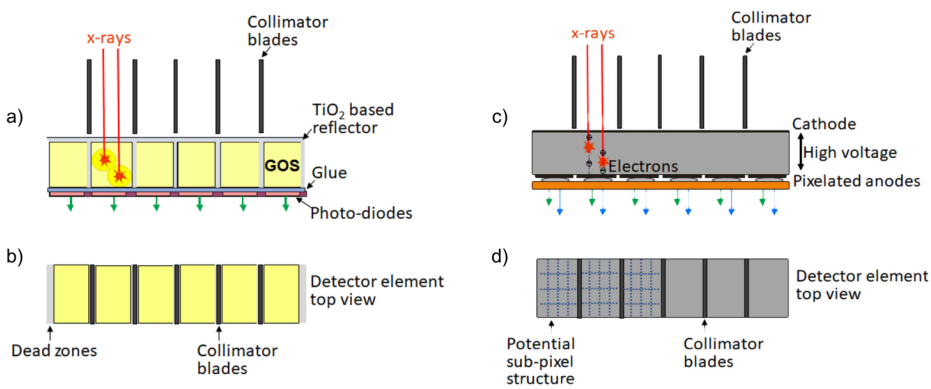

Figure 10 CT X-ray detectors

Schematic of an energy-integrating detector (left: a) side view, b) top view) and a photon-counting detector (right: c) side view, d) top view). In energy-integrating detectors, signals from photons of varying energies striking the detector during a projection are combined into a single output. Non-transparent walls create "dead zones," reducing the active detector area. In photon-counting detectors, made of semiconductor material under high voltage, the striking photons generate voltage spikes proportional to individual photon energies. The active area of the detector material is greater in this type of detector, and, as shown in the image, the anode is divided into sub-pixels, potentially enhancing spatial resolution. Copyright Springer Nature. Reproduced with permission. Flohr T,et al. Basic principles and clinical potential of photon-counting detector CT. Vol. 3, Chinese Journal of Academic Radiology. Springer; 2020. p. 19–34.

Photon-counting detector technology

Although photon-counting detector technology (PCDT) is not employed in the studies presented in this thesis, it warrants a brief overview due to its anticipated significant role in CT imaging in the near future.

The principle of photon-counting detectors is completely different from the energy-integrating type. It utilises a semiconductor material, such as cadmium telluride, as its detection medium. A high-voltage potential is applied over the semiconductor layer, between a cathode on the upper surface and an anode on the bottom surface. The anode is segmented into small, pixel-sized elements. Unlike scintillator-based detectors, the semiconductor material remains undivided, eliminating the need for separating walls and maximising the effective area available for X-ray photon detection (Figure 10) (18,19). When an X-ray photon strikes the semiconductor, it generates an electron-hole pair: the electron migrates towards the anode, while the "hole", which is not a real particle but rather the absence of an electron being transferred between atoms, drifts towards the cathode. This movement induces a voltage spike in the circuit, the magnitude of which correlates with the energy of the incident photon. These voltage spikes are sorted into multiple energy "bins," enabling the utilisation of individual photon energy data, which facilitates advanced applications such as spectral imaging. Electronic noise is mitigated by excluding the lowest energy bin, where noise is most prevalent. Additionally, the absence of physical segmentation enhances spatial resolution, offering potential superiority over scintillator-based detectors. Collimator blades remain necessary in front of the detector, but the spacing between them can be subdivided into sub-pixels defined by the anode pixel size, which can be as fine as 0.2 mm. There are potential issues with PCDT as well, most prominently the risk of photons interacting with the detector in the border zone of two anode pixels. In this case the energy from one X-ray photon can erroneously be split into two counts of lower energy photons (18,19).

Image reconstruction in CT

The CT Image

As discussed in the section on CT development, CT image data consists of voxels, each assigned a value on the Hounsfield unit (HU) scale. The Beer–Lambert law describes the exponential attenuation of X-ray intensity as it passes through matter:

$$I = I_0 e^{-\mu x}$$

where I is the intensity of the attenuated X-ray beam after traversing a material of thickness x cm with a linear attenuation coefficient μ. I_0 represents the initial, unattenuated beam intensity (15).

The purpose of CT image reconstruction algorithms is to determine the attenuation coefficient μ of the material within each voxel, based on the projection data measured by the detectors.

The HU assigned to a voxel is calculated as:

$$HU = \left(\frac{\mu_{material} - \mu_{water}}{\mu_{water}}\right) \cdot 1000$$

where $\mu_{material}$ and μ_{water} are the linear attenuation coefficients of the material and water, respectively. Using this formula, air has a HU of –1000 and water has a HU of 0, which are the fixed reference points of the HU scale (15). A hypothetical material with double the attenuation coefficient of water would have an HU of +1000.

Once HU values have been determined for all voxels, images are generated by mapping greyscale intensities to HU values, thereby creating a visual representation of the attenuation properties of tissues.

Filtered Back Projection

The following section is a simplified description of the algorithms used for image reconstruction in CT. As mentioned earlier, the work by Johann Radon laid the mathematical foundation for image reconstruction technologies still used in CT. The Radon transform is a procedure used to reconstruct a function from its line integrals from all angles (7). The line integrals in this context are represented by the attenuation of all parallel X-rays traversing the object, acquired at a particular angle, or "projection". These line integrals form an intensity profile of that particular projection. The collection of the intensity profile for all angles around the object is called the Radon transform and by "stacking" greyscale representations of them continuously next to one another a sinogram is produced. The sinogram is a graphical representation of the Radon transform (15,20,21). In the example in Figure 11, a line formed at each position on the x-axis of the sinogram corresponds to one detector element and the different projections are placed continuously along the y-axis (15).

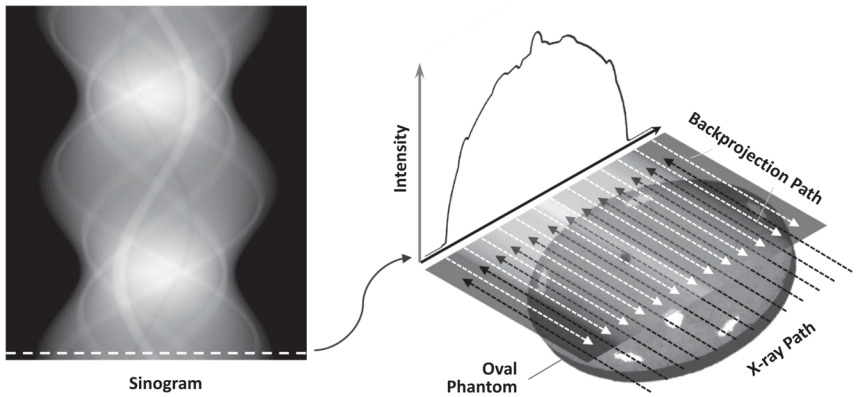

Figure 11 Back projection concept

Illustration of sinogram creation and back projection in CT imaging. Parallel black dashed arrows represent X-ray paths, generating an intensity profile. This profile, depicted as a two-dimensional greyscale strip, is placed in the sinogram along the white dashed line. Stacked intensity profiles from all projections form the complete sinogram. Back projection "smears" each profile's data along the original X-ray paths to reconstruct the image. Used with permission of SPIE. Hsieh J. Computed Tomography Principles, Design, Artefacts, and Recent Developments. Bellingham, Washington: SPIE; 2022. Permission conveyed through Copyright Clearance Center, Inc.

The term back projection means that the intensity profiles obtained from the scan of one CT-slice are "smeared" back across the potential image one by one, eventually forming an image including information collected at all angles. However, if back projection is performed using the raw, unfiltered projection data a very blurry image will be produced (Figure 12).

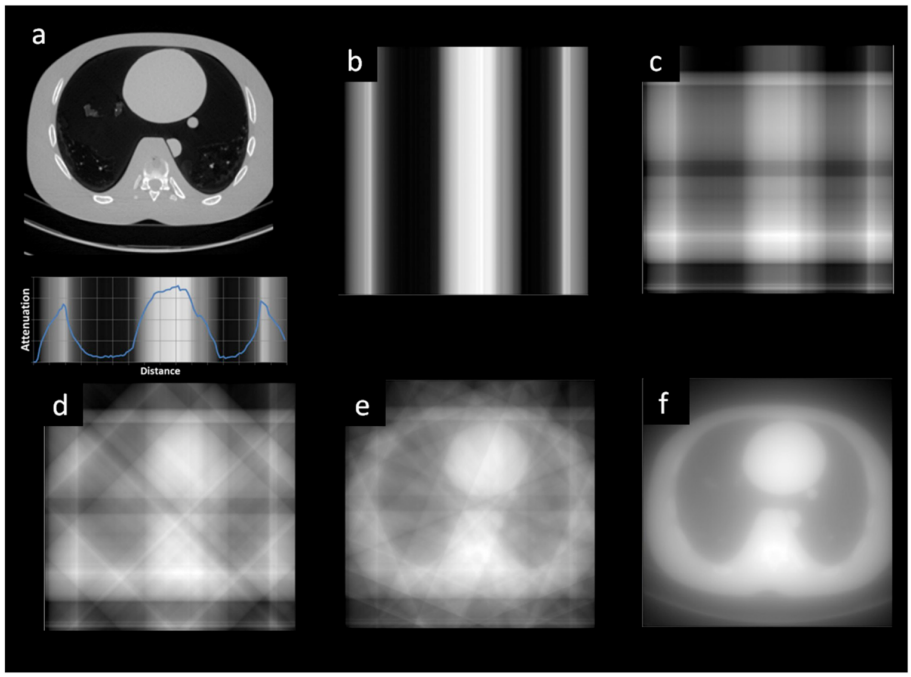

Figure 12 Back projection (without filtering)
Image reconstruction using simple back projection. The intensity profiles of all projections are sequentially "smeared" back along the original X-ray paths in a) – f). This technique yields blurry images as the information with the highest spatial frequencies are lost in relation to the lower frequencies.

A way to remedy this inferior image quality is to instead perform the FBP. This requires the data to be transformed into the frequency domain through a Fourier transform, which in this instance means that the intensity profiles from the Radon transform are deconstructed into their frequency content. For all angles (θ) the frequency function resulting from the Fourier transform of the intensity profile of the same angle is plotted in a graph with polar coordinates (i.e. a "circular" graph with the frequency curves for each θ radiating evenly on each side of the origin). This is called the "Fourier slice theorem". The lowest frequencies are placed centrally in the graph, with frequencies getting higher towards the periphery (Figure 13) (15,21,22).

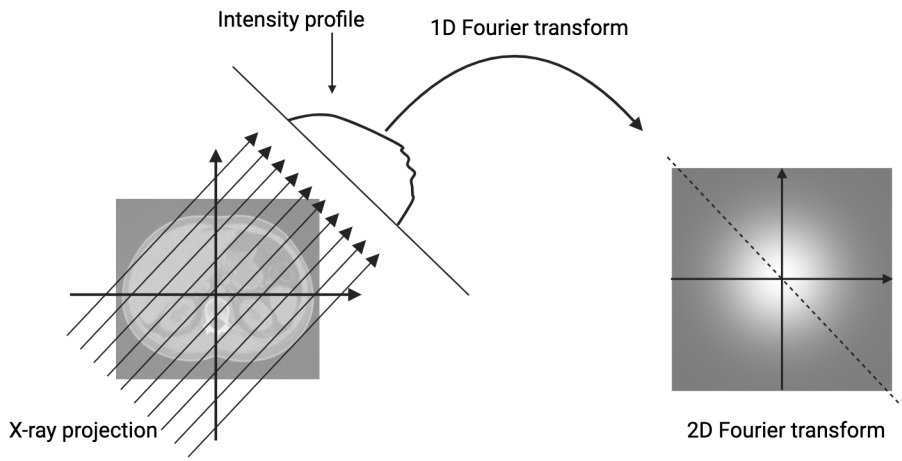

Figure 13 Fourier slice theorem
The one-dimensional (1D) Fourier transform of a CT projection's intensity profile is positioned at the corresponding angle within the two-dimensional (2D) Fourier transform. Created in BioRender. (2025) https://BioRender.com/4tk6msr.

Having transformed the data in this way, filters can be applied in a process called convolution. In the frequency domain Fourier transforms of different functions can be combined or "convolved" by basic multiplication. The most elementary filters are called Ramp- or RamLak-filters and consist of linearly increasing amplification of signal intensities with increasing frequencies. This amplification of the higher frequencies results in improved depiction of details and edges. After filters are applied, the frequency function of each angle θ is returned to intensity profiles in projection space through an inverse Fourier transform. Back projection can then be performed using the filtered, "sharper" intensity profiles of each projection, i.e. FBP. This process yields an improved depiction of the scanned object (Figure 14) (20,21,23,24).

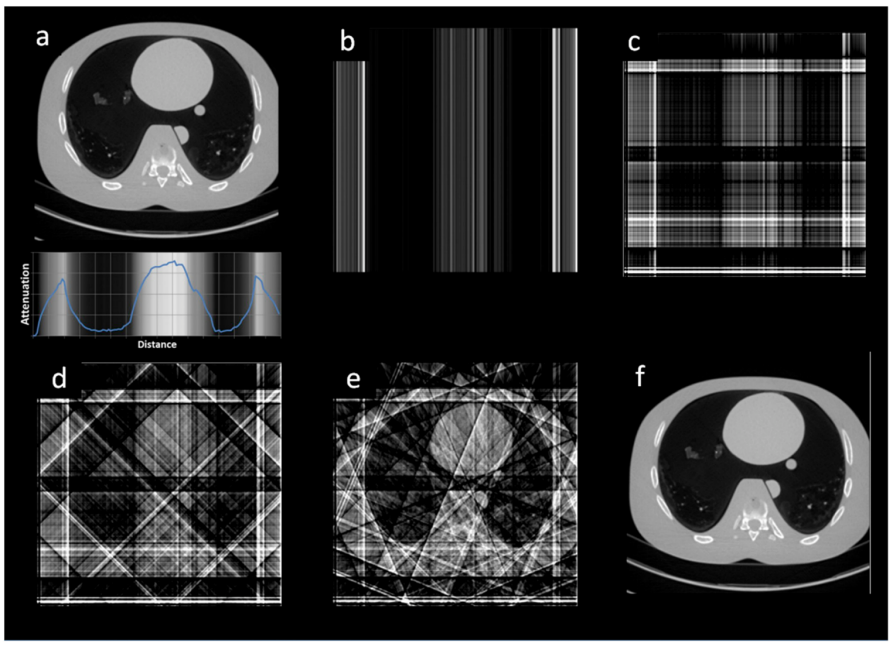

Figure 14 Filtered back projection
Adding a filtering step to the back projection process amplifies the high spatial frequency information, enhancing edges and increase the clarity in the images. The more pronounced edges in the intensity profiles and the resulting image is obvious in comparison to the simple back projection in Figure 12.

The filters applied in the frequency domain impact image quality in two main ways, spatial resolution and the texture and magnitude of the noise. There are several different basic filters, all amplify mid-frequency data compared to low frequencies. The difference between the filters is to what degree they amplify the intensity at high-frequencies. For example, the Ramp-filter mentioned above, increasing the amplification linearly up to the highest frequencies, is considered sharp, while others (e.g. Hann-filter) amplify mid-range frequencies but not the high frequency range and are accordingly called soft. This leads to differences in image appearance, with the sharp type yielding better spatial resolution but at the cost of a higher noise level, and the soft type producing images with lower spatial resolution while reducing the noise level (15,23,24). In the reconstruction algorithms of commercial CT scanners, the filters are referred to as convolution kernels. The exact function of the commercial kernels is not disclosed by the manufacturers, and they all use different nomenclature. However, all vendors have several different kernels ranging from sharp to soft, optimised for different imaging tasks. Traditionally sharper kernels are used when depicting anatomy with large inherent contrast, such as lungs or bone. Softer kernels are often recommended for examinations aimed at soft tissues.

Iterative Reconstructions

FBP has been a cornerstone reconstruction technique in CT for decades, valued for its stability and speed. However, its performance is limited by simplifying assumptions that fail to fully reflect the reality of image acquisition. FBP assumes an idealised CT system geometry and measurements free from fluctuations, which deviates from reality, leading to noise and artefacts in reconstructed images. To address these limitations, iterative reconstruction (IR) methods were developed, and over the past decade, they have become the primary reconstruction approach in most modern CT scanners (22,25,26).

CT manufacturers have developed their own versions and the information available on their inner workings is sparse. However, the underlying principle of iterative reconstructions is known and shared by the different versions: The repeated alterations of the image data between projection space and image space iteratively improving image quality during image reconstruction. Figure 15 demonstrates an overview of the iterative reconstruction process.

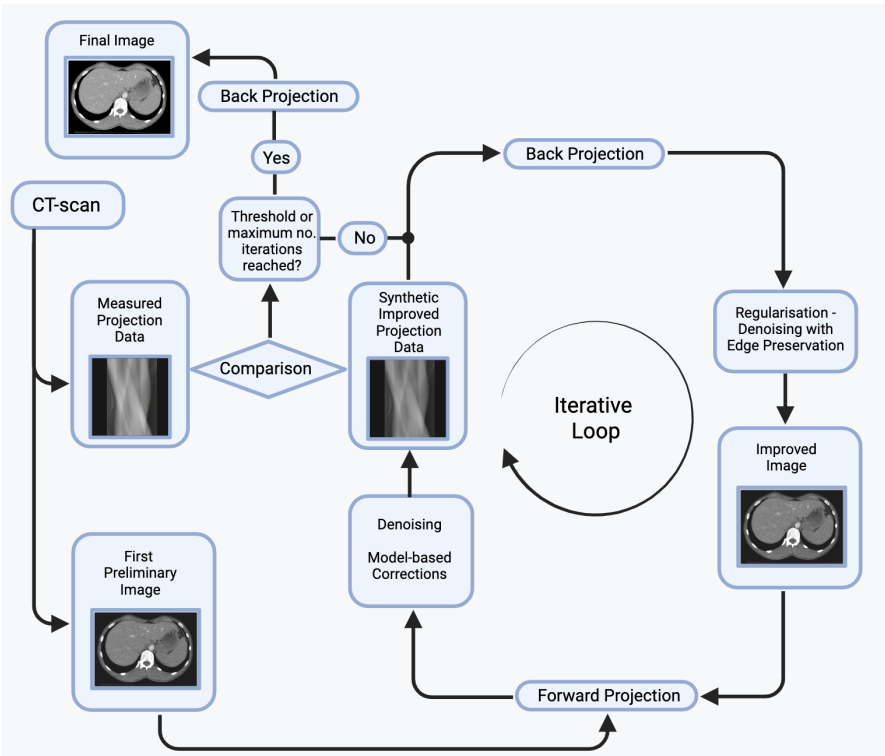

Figure 15 Iterative reconstruction
Schematic illustration of the iterative reconstruction process. Created in BioRender. (2025) https://BioRender.com/i3hy0o9

The IR process begins with raw data from the scan and an initial image is generated via back projection. In image space, a process called regularization is applied to denoise the image while preserving edges. This involves smoothing unrealistic large attenuation differences between adjacent voxels, enhancing overall clarity. The updated images are then forward projected to form synthetic, improved projection data in projection space, where further denoising is performed. Model-based corrections can also be implemented here, accounting for CT system geometry (e.g., X-ray tube focal spot, detector element size etc.), X-ray physics, and photon-object interactions. The updated, synthetic projection data is compared to measured, original data and unless the difference is below a threshold or a maximum number of iterations is reached, the cycle repeats with new back-projected images (22,25,26).

Early IR algorithms, known as statistical iterative reconstructions, focused on noise reduction using statistical models, as use of the model-based corrections was too computationally demanding. Statistical methods rely on comparing measured projection data fluctuations to expected noise distributions and are paired with regularization in image space (25,26).

More advanced full model-based IR incorporates detailed system and physics models, while hybrid iterative reconstructions blend elements of both, striking a balance between image quality, speed, and computational load. ADMIRE by Siemens, used in **Paper IV** of this thesis is considered a hybrid iterative reconstruction algorithm (22,26).

Despite their advantages, IR methods face drawbacks. Initial versions suffered from prolonged reconstruction times and overly smooth image textures, which some radiologists found suboptimal. Recent advancements have mitigated these issues, improving efficiency and texture preservation. However, research reveals inconsistent findings on IR's impact on detecting small, low-contrast lesions, partly due to the non-linear nature of edge-preserving denoising. This can lead to heterogeneous spatial resolution and noise, potentially affecting diagnostic accuracy for such tasks, highlighting an area for further investigation (25,26).

Dual Energy CT

The concept of using more than one X-ray energy spectrum to differentiate materials based on their attenuation properties dates back to the early days of CT. In his 1973 paper, Godfrey Hounsfield described an approach to approximate the atomic number of materials within a CT slice:

"It is possible to use the machine for determining approximately the atomic number of the material within the slice. Two pictures are taken of the same slice, one at 100 kV and the other at 140 kV. If the scale of one picture is adjusted so that the values of

normal tissue are the same on both pictures, then the picture containing material with a high atomic number will have higher values at the corresponding place on the 100 kV picture. One picture can then be subtracted from the other by the computer so that areas containing high atomic numbers can be enhanced" (12).

This early insight highlights Hounsfield's visionary understanding of CT technology. Today, the concepts he described are referred to as "Dual energy CT" and "Material decomposition" or "Spectral imaging".

The added value from dual energy CT (DECT) is the information that can be deduced from the difference in attenuating properties of different elements, when examining the same object using two different X-ray energy levels. Using this information applications such as material decomposition (MD), monoenergetic images and virtual non-contrast images can be produced. Ideally, the two different datasets should be spatially and temporally matched and acquired with sufficient energy separation. The quality of the data in the two datasets should also be as equal as possible, i.e. the noise level should be similar (27). Several different technical solutions to these demands have been introduced, of which the following are the most commonly used types of dual-energy technology (Figure 16):

- Dual Source DECT, employs two X-ray tubes and detector arrays positioned at approximately 90° to each other within the gantry enabling simultaneous acquisition. As the kVp of the two tubes and the filtration of the X-ray spectra are adjusted individually, many different kVp combinations can be used, and large energy separation can be achieved. Drawbacks of this technology is that the field of view is limited as the secondary detector is slightly smaller due to limited space in the gantry. As there are two X-ray sources and detectors working concurrently, there is a risk of scattered photons reaching the wrong detector causing noise. Use of dual energy also demands specialised protocols that must be selected while planning the examination (27,28).

- Rapid kVp Switching alternates the tube voltage between high and low settings thousands of times per second, facilitating near-simultaneous dual-energy data collection. A single X-ray tube and detector is used, and the dual energy data collection covers the whole field of view. The spectral separation is more limited, though, and it is hard for the tube load to increase swiftly enough to sustain the low kVp-setting. To compensate for this and achieve similar image quality between the datasets, asymmetric sampling is used, with longer interval for the low energy level (27,28).

- Dual-Layer detectors use a single X-ray tube paired with a two-layered detector that separates high- and low-energy photons based on penetration depth. The lower energy photons from the single polychromatic spectrum are collected in the superficial layer of the detector while the high energy photons penetrate to,

and are detected by, the deeper layer. Combining the information from the two layers yield single energy data. This technology facilitates continuous use of standard examination protocols, and the dual-energy data can be retrieved retrospectively when needed. However, also this technology suffers from limited spectral separation and the noise level can differ between the datasets (27,28).

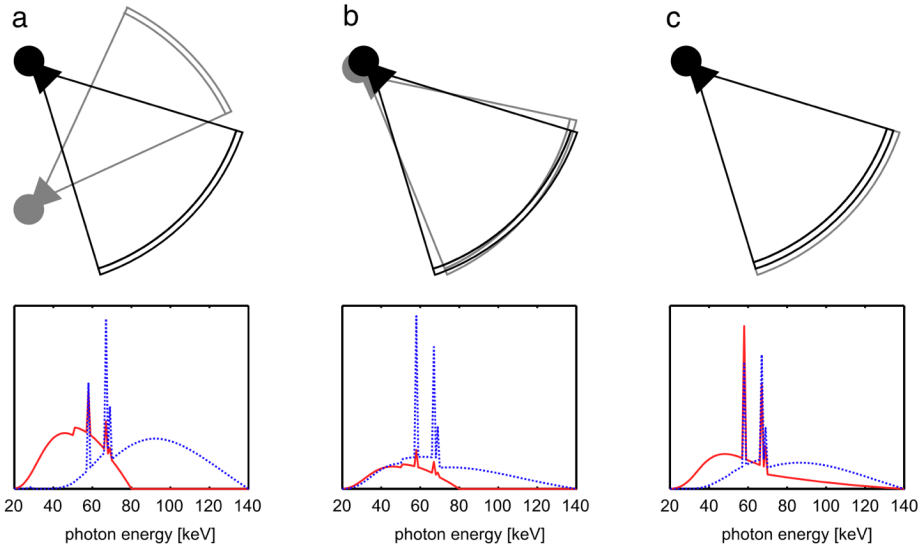

Figure 16 Dual energy CT technologies

Illustration of the three most common dual energy CT technologies. a) Dual source; b) Rapid kVp switching c) Dual layer detectors. In the bottom row the photon energy spectra of the two different scans/datasets is visualised. The technologies have different advantages, but regarding the separation of the energy spectra, dual source is the better performer due to the possibility for varying filtration of the two X-ray sources. Modified from Fredenberg E. Spectral and dual-energy X-ray imaging for medical applications. Vol. 878, Nuclear Instruments and Methods in Physics Research, Section A. Elsevier B.V.; 2018. p. 74–87. Used with permission of Elsevier Science & Technology Journals.

Material Decomposition

As MD constitutes a primary application of DECT and forms the focus of **Paper II** within this thesis, the following section provides a brief overview of this technique.

A variety of algorithms have been developed for MD of DECT-acquired data, with processing options available in either projection space or image space. These algorithms enable the separation of two or three materials, depending on the underlying assumptions and data utilised (27,28).

In two-material decomposition, it is assumed that the linear attenuation coefficients are composed of the photoelectric effect and Compton scatter and that their sum decreases linearly with increasing photon energy. By analysing the attenuation coefficients of a voxel derived from two distinct energy spectra (e.g., 80 kVp and 140 kVp), the contributions of two selected basis materials, such as water and iodine, can be computed. For three-material decomposition, reliant on the same dual-energy dataset, additional information is needed. This is addressed by assuming that the voxel's volume or mass in its entirety is composed of three basis materials, allowing the determination of each material's contribution to the total linear attenuation coefficient of the voxel (21,28–30). The calculations involved in MD are complicated, but vector-based graphical methods, as illustrated in Figure 17, provide a more accessible means of understanding the process (28–30).

In current abdominal CT practice, MD supports clinically important applications. One is the identification and isolation of iodine, generating "iodine maps" and virtual unenhanced images. Another is the production of virtual monoenergetic images - simulated CT acquisitions at user-selected monoenergetic levels. These images amplify the iodine content at lower energy levels and mitigate beam-hardening artefacts at higher energies. Monoenergetic images are generated by assessing the composition of basis materials within each voxel and calculating their attenuation at the specified keV level, based on the established relationships between linear attenuation and energy (28–30).

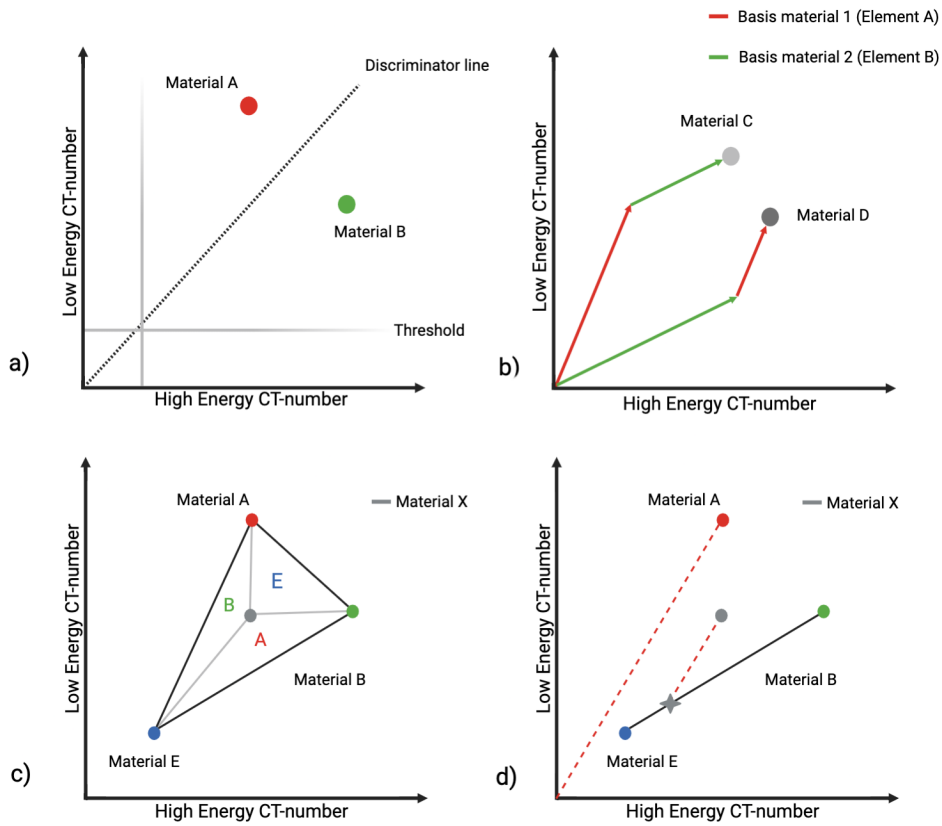

Figure 17 Material decomposition

a) Two-Material Decomposition: This method visualises the attenuation of two distinct materials at low and high peak kilovoltage (kVp) settings within a scatterplot. Provided the ratios of CT-numbers at low to high kVp levels for the two materials differ sufficiently, a discriminator line can be drawn between them, enabling the materials to be separated and colour-coded in all voxels. Threshold levels must be established for both kVp settings, below which no colour-coding is applied.

b) Basis Material Decomposition: The CT-number of any voxel can be broken down into the contributions from two selected basis materials, such as water and iodine. This principle underpins widely used applications, including iodine maps and virtual non-contrast images.

c) Three-Material Decomposition: Separating three materials using only two datasets requires the assumption that the voxel's volume or mass comprises solely these three materials. If the unknown element X is positioned close to material A, the area attributed to A increases, indicating a greater contribution from material A.

d) Subtraction of material A from the unknown material X, the star signifies the resulting CT-number made up from materials B and E.

Created in BioRender. (2025) https://BioRender.com/1qw63o1

Dosimetry in CT

Given that X-ray radiation is ionising, and CT examinations deliver significantly higher doses than conventional X-ray, accurate dosimetry is critical to monitor patient radiation exposure effectively. The two primary metrics for assessing CT radiation dose are the Volume CT dose index ($CTDI_{vol}$) and the dose-length product (DLP).

Computed tomography dose index

CT dosimetry has evolved in tandem with advancements in scanner technology (detailed in a later section), necessitating adaptations to the CTDI metric. Across all iterations, CTDI has been measured using standardised phantoms with diameters of 16 centimetre (cm) (head) and 32 cm (body), employing an ionisation chamber placed in centrally and peripherally located holes to directly measure deposited dose. The radiation output of all CT-scanners is measured and calibrated using this standardised method (31,32).

In its original form CTDI quantified the radiation energy per unit mass delivered during a single axial scan, expressed in milligray (mGy). However, abdominal scans reveal a highly inhomogeneous dose distribution, with peripheral doses at least double those at the centre. To address this, the weighted CTDI ($CTDI_w$) was introduced, combining one-third of the central dose with two-thirds of the peripheral dose (31).

$CTDI_{vol}$, a version adapted to helical scans in multislice scanners, adjusts $CTDI_w$ by dividing it by the helical pitch, i.e. the ratio of table movement per rotation to beam width. A pitch of 1 indicates uniform coverage, while a pitch above 1 "stretches" the spiral (reducing dose) and below 1 "compresses" it (increasing dose) (31,32).

Modern CT-scanners automatically display $CTDI_{vol}$ post-scan. However, a limitation to consider is that $CTDI_{vol}$ only truly reflects what the dose would have been in a 32 cm phantom, given the X-ray output of the scan. $CTDI_{vol}$ therefore potentially overestimates dose in larger patients, while underestimating it in smaller ones (31).

Dose-length Product and Effective Dose

Dose-length product (DLP) is a measurement of the total amount of radiation energy transferred to the patient. It is calculated by multiplying the $CTDI_{vol}$ with the scan length in cm. The unit consequently is mGy×cm.

The DLP further enables the calculation of effective dose, measured in Sieverts (Sv), by applying region-specific conversion factors (e.g., 0.015 mSv/mGy×cm for the adult abdomen and pelvis). The effective dose provides an approximate estimate of radiation-induced risks, predominantly cancer and hereditary effects and the International Commission on Radiological Protection (ICRP) estimates the risk at 5% per sievert. However, effective dose was primarily designed for radiation protection purposes,

representing average risk in a population, necessitating cautious application to individual cases (16,33).

Image quality analysis

Noise

Image noise in CT refers to the random variation in CT-number caused by different steps in the image acquisition and reconstruction process. Noise can be characterised in different ways, most commonly by determining its magnitude by using the standard deviation (SD) of a measurement of CT-number as a proxy value for the magnitude. The measurement is performed by placing a region of interest in a homogeneous area of the image. The major contribution to image noise is the randomness in the number of photons contributing to image information, called quantum noise. This is caused by the random interactions involved in X-ray generation as well as their attenuation and detection processes. Quantum noise is inversely proportional to the square root of the number of X-ray photons, i.e. radiation dose.

Contrast-to-Noise ratio and Signal-to-Noise ratio

One of the most commonly used image quality metrics is the contrast-to-noise ratio (CNR) conveying information on contrast resolution and noise magnitude in one numerical value. CNR can be calculated in different ways, where the standard method is to use the difference in CT-number between two adjacent structures as contrast, divided by the noise magnitude described above. CNR has long been considered to be proportional to detectability of lesions as it describes a balance between contrast facilitating detection and noise acting to its detriment (34–36). A schematic description of CNR is presented in Figure 18.

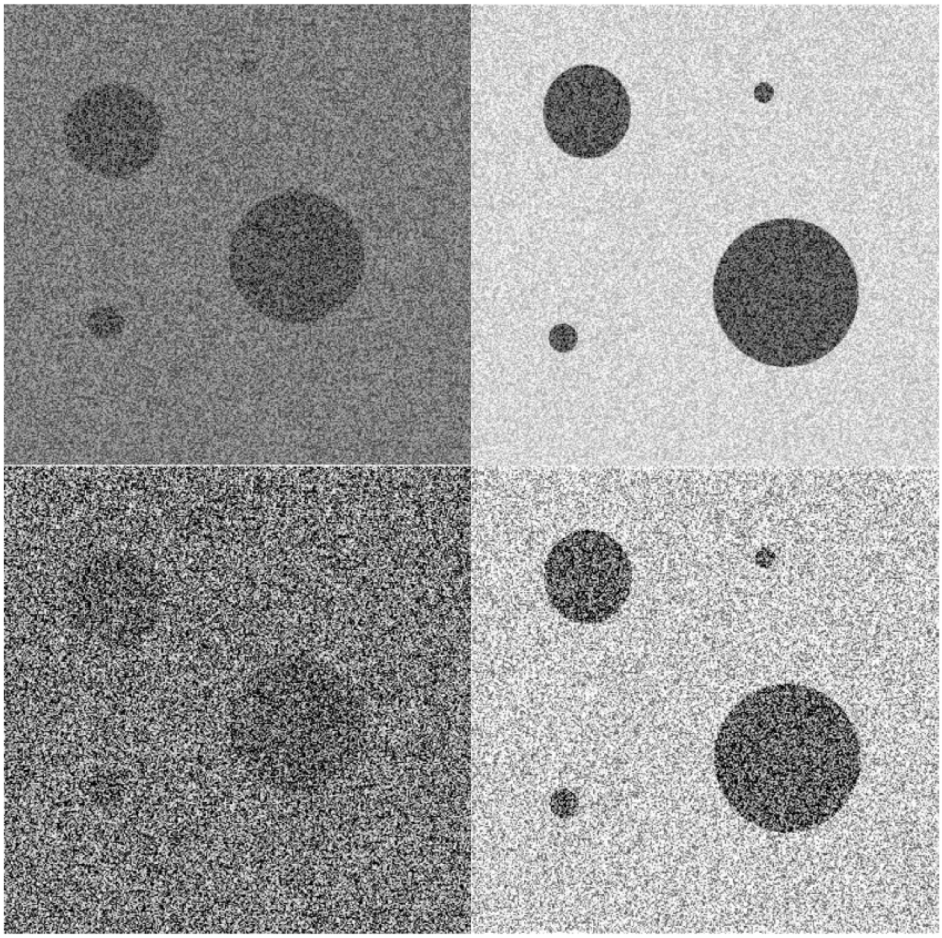

Figure 18 Schematic presentation of contrast-to-noise ratio (CNR)
Four image panels with varying CNR. Noise magnitude is higher in the bottom row and lower in the top row. In the left column the contrast between lesions and background is smaller, while it is larger in the right column. This results in the highest CNR being present in the top right panel and the lowest bottom, left. Note that the smallest lesion cannot be detected in the image with the lowest CNR. Copyright Peter Leander, reproduced with permission.

Signal-to-noise ratio (SNR) is a metric used in many types of analyses involving signal in different fields of science. In its most basic form, it is defined as the ratio of the measured signal to the noise. In the context of CT, the signal is the CT-number measured within a region of interest and the noise is the SD of the measurement (37,38).

Noise Power Spectrum (NPS)

In addition to magnitude, image noise can also be characterised by its texture, i.e. its spatial frequency content. Noise can be coarse with large grains, or it can have a finer structure. To describe this quality of the noise, the NPS is used. The NPS is produced by performing a Fourier transform of the measured variation within a ROI, after subtraction of the mean CT-number. This yields a curve where the noise is distributed by its spatial frequency. Image noise with a coarse structure leads to an NPS-curve with a larger fraction of its noise located at low spatial frequencies, while more noise at higher spatial frequencies equals a finer noise texture (39). For a visual representation of noise with different texture and the matching NPS-curves, see Figures 35 and 36 in the Results section.

Image quality analysis using observer studies

In the context of this thesis two different types of observer studies employing human readers are important to mention. One type focuses on the visualisation of normal anatomic structures within the images and the grading of the visualisation of these normal structures is considered a proxy for image quality. Visual Grading Analysis (VGA) and Visual Grading Characteristics (VGC) are two closely related methods based on this type of image quality rating. VGC is an evolution of VGA that by using a non-parametric receiver operating characteristics (ROC)-like analysis more statistically correctly treats the ordinal data from the rating scale. A common critique of VGA/VGC is that these methods analyse image appearance rather than their performance in clinical decision making. Analyses more focused on specific diagnostic tasks, such as detection of a particular type of lesions, might be more important when comparing the performance of different types of examinations. However, a strength of VGC is that images of patients without a particular type of pathology can be used. Hence, these methods are economical with time and resources as the cumbersome process of identifying and including particular patients is avoided. VGC was developed at Gothenburg University by M. Båth and colleagues (40).

Different types of ROC-based analyses are important in evaluating task-based performance of diagnostic methods. In image quality analysis ROC requires the use of a grading scale, rating, for example, the probability of a particular type of pathology. In basic ROC this probability is rated on a per patient basis, i.e. the probability graded is that the pathology is present anywhere in the images of the patient. Individual lesions are not graded or analysed. The free-response ROC (FROC) and the further development jackknife alternative FROC (JAFROC), on the other hand, are methods in which the observer localises and grades individual lesions within the images. This is a task very similar to image reading in clinical practice.

In ROC the true positive fraction (sensitivity) is plotted against the false positive fraction (1 – specificity) (Figure 19). A test with high sensitivity detects a large fraction of the pathological entities. High specificity, on the other hand, means that the test performs well when ruling out the condition. When deciding on a threshold level determining positive and negative outcome of a test, a trade-off between sensitivity and specificity has to be made. A high threshold means that positive cases with a low rating will be classified as negative, reducing sensitivity. Reversely, the same high threshold leads to fewer negative cases being classified as positive – specificity increases. The ROC-curve can be seen as a visualisation of this balance between sensitivity and specificity when adjusting the threshold level (39–41). An ideal test without any overlap in ratings between positive and negative cases gives an ROC AUC of 1, whereas a test performing no better than pure chance has a AUC of 0.5. Apart from the demanding process of identifying suitable patients, ROC-studies also demand a well-established gold standard for comparison of the observer ratings (39).

JAFROC, being a version of ROC, is also based on the same type of curve, and the AUC is the figure of merit of the analysis.

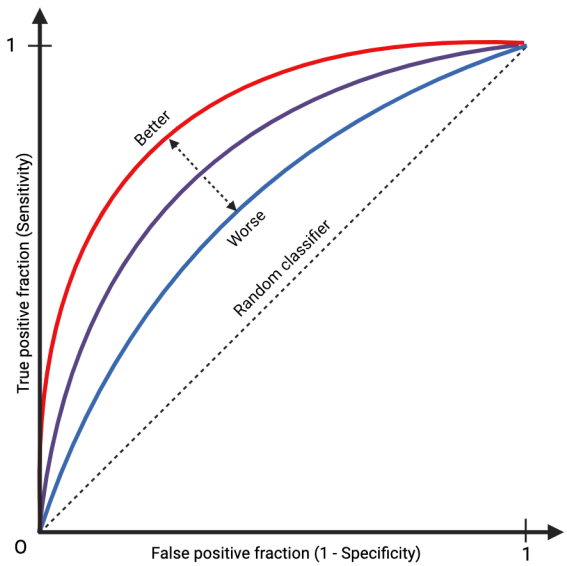

Figure 19 Receiver operating chacteristics (ROC)-curve

The ROC curve plots the true positive rate against the false positive rate. An ideal operator's curve rises vertically along the y-axis to the top-left corner, then horizontally to the point (1, 1), yielding an area under the curve (AUC) of 1. The diagonal, dashed line, with an AUC of 0.5, represents random guessing. The red ROC curve indicates the best-performing test among the three shown in the graph. Created in BioRender. Fält, T. (2025) https://BioRender.com/h3fyn1d

Ionising Radiation and Risk of Cancer Induction

The effects from radiation on humans fall into two categories: deterministic effects of acute high radiation doses and stochastic effects that are more important after exposure to lower doses. The deterministic effects are caused by tissue damage due to cell death and inactivation and, above a threshold, their severity are proportional to the radiation dose. Stochastic effects, mainly cancer induction via DNA damage, happen by chance and their probability increase with increasing radiation dose, but the severity of the outcome does not (33).

The association between ionising radiation and an increased incidence of cancer has been recognised for approximately a century. One of the earliest documented connections emerged among workers who, in the early 20th century, applied luminous, radium-containing paint to watches and dials. The workers often used their mouths to point the brushes, increasing the exposure of the mouth and jaw and within a decade several cases of osteosarcoma were identified (42). However, the primary epidemiological evidence linking radiation exposure to cancer incidence and mortality in humans stems from studies of survivors of the atomic bomb detonations over Hiroshima and Nagasaki, Japan, in 1945. This cohort was exposed to ionising radiation, predominantly high-energy gamma and neutron radiation, in a single, brief event. The survivor cohort is investigated through the Life Span Study (LSS), including individuals exposed to doses up to 2 gray (Gy), though the mean exposure was approximately 200 milligray (mGy). The gray is the SI unit for absorbed radiation energy per unit mass (absorbed dose), calculated as energy in joule divided by kilogram.

The LSS cohort, tracked for nearly 70 years, has provided robust epidemiological evidence linking radiation exposure to increased incidence and mortality from various cancers (43). Among these, leukaemia exhibits the highest relative risk elevation, though a significant association is also observed with solid cancers (43). Leukaemia also has a risk profile over time differing from solid cancers. The mortality from excess cases of leukaemia was highest during the first decade following the bombings, and then decreased gradually. Solid cancer mortality, on the other hand, has been shown to increase with age, with the risk from radiation adding to the baseline risk of cancer increasing with age. The magnitude of the risk increase regarding solid cancers is strongly influenced by the age at radiation exposure, with individuals exposed at younger ages exhibiting a heightened risk that persists throughout their lifetime (43,44).

Occupational Exposure to Radiation

Another well-studied population comprises individuals monitored over several years following occupational radiation exposure. This group primarily includes nuclear

power plant workers, alongside those employed in other sectors such as the nuclear and weapons industries.

Unlike the Japanese atomic bomb survivors this group has predominantly been exposed to low doses of radiation over extended periods, known as low dose-rate exposure. The cumulative radiation dose within this group varies considerably, as does the type of radiation to which they have been exposed (45). A large cohort-study including over 300,000 nuclear workers in France, the United Kingdom (UK) and the USA has been ongoing for many years. The most recent analysis demonstrates a clear relationship between radiation dose and cancer mortality, including leukaemia and solid cancers, despite a mean cumulative dose as low as 18 mGy (46,47).

Low-Dose Radiation and the Linear No-Threshold Model

As outlined above, high doses of radiation are well-established as increasing cancer risk. However, the relationship between lower radiation doses, particularly below 100 mGy, and cancer risk remains less certain. This is of major importance in the context of this thesis, as the radiation dose from a CT examination of the abdomen is well below this level. For decades, it has been assumed that the linear relationship observed at high doses extends to lower doses, down to zero, forming the basis of the Linear No-Threshold (LNT) model. This model describes a linear dose-risk relationship without a threshold below which radiation exposure would be deemed harmless (48–50). However, it is important to recognise that the LNT model constitutes a broad assumption for radiation doses below 100 mSv and low dose rates (below 0.1 mGy / min), and there is still a lively scientific and regulatory debate regarding the cancer risks associated with low radiation doses. Some research groups propose the existence of a threshold dose, below which radiation may pose no harm - or could even have beneficial effects (51–53).

The terms Low Dose Effectiveness Factor (LDEF) and Dose Rate Effectiveness Factor (DREF) have been introduced for estimations of the cancer risk after exposure to radiation at low doses and/or low dose rates. A numerical value above 1 means that the risk linearly approximated from higher dose levels is divided by this number at low doses and dose rates, reducing the risk assumptions (33). The International Commission on Radiological Protection (ICRP) has combined these two entities into the Dose and Dose-rate Effectiveness Factor (DDREF) and assigned it a value of 2 (33). The debate is still not settled though, and there is ongoing work by "Task force 91" appointed by ICRP. A preliminary report was released in 2025, and it reaffirms the view that there is a real risk of cancer from radiation at low doses and low dose rates. A carefully worded, preliminary conclusion says "an LDEF of much more than 3 is not supported, and much less than 1 likewise. Similarly, it is concluded that a DREF value much larger than 3 or less than 1 is also unlikely." (54)

One reason the association between radiation exposure and cancer at doses below 100 mGy has remained uncertain for many years is that any potential increase in risk is likely to be very small. Establishing such a relationship necessitates large-scale epidemiological studies with sufficient statistical power and extended follow-up periods to adequately assess potential cancer development.

Early Evidence Linking CT Radiation to Cancer Risk

At roughly the same time as this somewhat long-running thesis work started, the first epidemiological study establishing a direct relationship between radiation exposure from CT-examinations and an increased cancer incidence was published (55). A cohort study involving 170,000 patients in the United Kingdom (UK) who had undergone CT examinations during childhood or early adulthood (up to 22 years of age) reported a modestly elevated incidence of leukaemia and brain tumours. Increased risk is often quantified using Excess Relative Risk (ERR), defined as: "The rate of disease in an exposed population divided by the rate of disease in an unexposed population, minus 1.0." This is typically expressed as the excess relative risk per Gy or per Sv" (ICRP, 2007) (33). The ERR for leukaemia was 0.036 per mGy, while that for brain tumours was 0.023 per mGy. This association was observed at radiation doses as low as 30–50 mGy, corresponding to an absolute risk increase of approximately one additional case of leukaemia and one additional case of brain tumour per 10,000 head CT examinations (56).

Iodinated Contrast Media

This section will focus on iodinated contrast media, starting with a summary of its history followed by a more in-depth analysis of the potential and much disputed relationship between intravenously administered iodinated contrast media and risk of subsequent kidney injury. Finally, the physical properties, such as the cross section at different levels of photon energy, of iodine and other potential contrast media elements will be discussed.

History of Iodinated Contrast Media

Since the early days of radiology, iodine has been used as a contrast medium, owing to its significantly greater ability to attenuate X-ray photons compared to most human tissues. The first commercially available iodinated contrast medium, Lipiodol, an iodine-containing oil, was introduced in the early 1920s and was predominantly utilized for the opacification of the subarachnoid space (57).

Within a few years, iodide salts, such as sodium iodide, were introduced for use in retrograde pyelography, replacing colloidal silver, which had been demonstrated to induce renal damage and even fatalities. During the early 20th century, sodium iodide was also employed in the treatment of infectious diseases, including syphilis. Osborne and colleagues at the Mayo Clinic in the USA observed that the urinary bladder occasionally appeared radiopaque on X-ray images following such treatments. This observation prompted the hypothesis that sodium iodide could be used for excretory urography following intravenous administration. However, initial experiments proved unsuccessful, as the opacification of the urinary tract was inadequate (58).

During this period, chemists in Germany were synthesizing a variety of novel organic compounds, some of which incorporated iodine atoms. Although these compounds were primarily developed as antimicrobial agents, Moses Swick, a young American physician undertaking a fellowship in Germany, observed that the urine of animals administered these experimental substances had high concentrations of iodine. This discovery prompted him, in 1929, to propose the use of a pyridine derivative containing an integrated iodine atom as a contrast agent for excretory urography. While the first version caused severe adverse effects, subsequent iterations were developed, and di-iodinated pyrimidine compounds were found to be well-tolerated. These compounds became the standard contrast media for urography and angiography in the decades that followed (58,59).

The next advancement in the development of iodinated contrast media was the introduction of a new type of iodine containing organic compounds, based on a benzene ring. Once again, Dr. Swick played a pivotal role as one of the innovators, developing the initial, though unsuccessful, version as early as the 1930s. Not until two decades later the contrast media molecules based on the benzene ring were sufficiently refined to be introduced - but when they were, it was in the form of tri-iodinated molecules. This represented a significant leap forward and this type of molecule forms the basis for the iodinated contrast media still in use today. Well known molecules of this type are diatrizoate and iothalamate, among others (57–59).

The initial versions of tri-iodinated molecules were ionic in nature and used as contrast media in the form of salts, typically bonded to sodium or meglumine ions. In solution, these salts dissociate into two ions, generating two osmotically active particles. At the concentrations required to achieve sufficient X-ray attenuation from the iodine atoms, the contrast media produce a markedly elevated osmolality - several times greater than that of blood plasma. Consequently, this class of agents is designated as high osmolar contrast media (HOCM). While the introduction of HOCM was a significant breakthrough and they remained a cornerstone of clinical practice for many years, these agents were associated with several adverse effects. The most severe adverse effects were painful intra-arterial injections, frequent allergy-like reactions, and an increased risk of

renal injury. Less severe, commonly reported side effects included nausea and a sensation of warmth following injection (59–61).

The pain experienced by patients during angiographic procedures led Swedish radiologist Torsten Almén to investigate the underlying cause of this specific adverse effect (Figure 20). Drawing an analogy to the burning sensation in the eyes encountered while swimming in saline ocean water, Dr. Almén hypothesised that the high osmolality of contrast media solutions, when injected into the blood vessel, was responsible for the associated pain. Dr. Almén made the effort to study chemistry outside his work as a radiologist and formulated a theoretical approach to convert existing ionic contrast agents into non-ionic forms. He proposed that this transformation could be achieved by removing the dissociating carboxyl group and incorporating hydrophilic hydroxyl groups. These modifications were intended to eliminate the cation, thereby halving the number of osmotically active particles, while simultaneously enhancing the molecule's water solubility. Despite his efforts to engage the industry with these innovations, Dr. Almén encountered scepticism, reminiscent of the initial resistance faced by Godfrey Hounsfield when he introduced his concept of computed tomography to the radiological community, delaying widespread acceptance of his ideas for an extended period (58,59).

Figure 20 Torsten Almén and the King

All theses on contrast media, written in Malmö, must include a picture of Torsten Almén. Here he is, in 1987, honoured with the prestigious Fernström Prize, a distinguished Nordic award for medical research, presented by the King of Sweden. Copyright Unknown.

Eventually, though, by the late 1960s, Dr. Almén established a collaboration with the Norwegian company Nyegaard & Co., leading to the development of the first non-ionic, low-osmolar iodinated contrast agent, metrizamide, marketed under the name Amipaque. Despite its groundbreaking nature, Amipaque had significant limitations that restricted its commercial potential. It was considerably more expensive than existing HOCM and was supplied as a powder that had to be dissolved in fluid before injection.

Nevertheless, by introducing low-osmolar contrast media (LOCM) to the market, Amipaque represented a major advancement, inspiring other manufacturers to develop new compounds. In the early 1980s, several new LOCM agents were introduced, including iopamidol (Iopamiron, Bracco), iohexol (Omnipaque, Nyegaard & Co.), and ioxaglate (Hexabrix, Guerbet) (Figure 21). Over the following decades, LOCM gradually became the predominant class of contrast agents and remains the standard in clinical practice today.

Nyegaard & Co., later rebranded as Nycomed, continued innovating in contrast media development. In the 1990s, the company introduced iodixanol (Visipaque), a molecule consisting of two tri-iodinated benzene rings fused into a single molecule. This design incorporates six iodine atoms per osmotically active particle, again reducing osmolality by half. Iodixanol is considered iso-osmolar to plasma, classifying it as an iso-osmolar contrast medium (57–59).

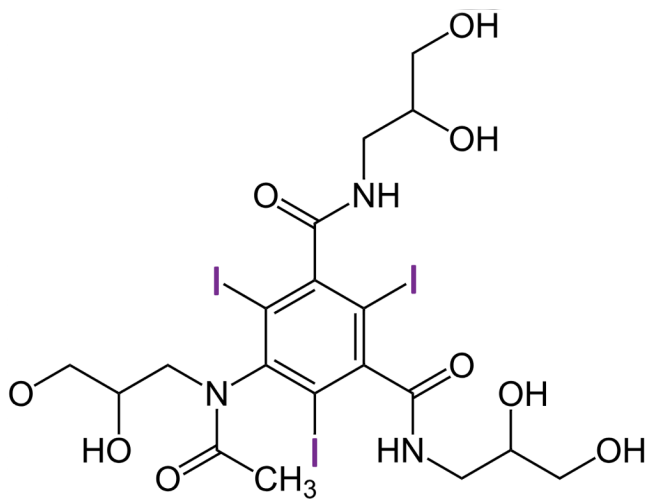

Figure 21 Iohexol molecule
The chemical structure of Iohexol. Note the three iodine atoms in purple, located on the central benzene ring. From: https://commons.wikimedia.org/wiki/File:Iohexol_Structural_Formula_V.1.svg

Risks associated with low-osmolar contrast media

The pain experienced during injections of HOCM is no longer a concern, as it was directly caused by the high osmolality of older agents. However, LOCM are not without side effects.

Iodine atoms in iodinated contrast media are covalently bound to large molecules, but the solutions inevitably contain a small concentration of free iodide ions. This free iodide can influence thyroid function, posing a significant risk for patients with hyperthyroidism by exacerbating their symptoms. Additionally, iodide exposure can saturate thyroid iodine uptake for several months, potentially diminishing the effectiveness of radioiodine therapy for thyroid tumours or hyperthyroidism. While these complications can be serious, they affect only a very small subset of patients (62).

Allergy-like hypersensitivity reactions to LOCM range from mild symptoms such as urticaria to severe, life-threatening anaphylactic shock. Even though they still exist, hypersensitivity reactions are considerably less frequent after administration of LOCM as compared to HOCM (60,63).

Contrast Induced Kidney Injury

The most significant risk associated with LOCM - and the subject of extensive research over many decades - is kidney injury, both acute and long-term. Assessing this risk is an important task during a radiologist's daily practice, as each contrast enhanced CT examination requires carefully balancing the assumed impact on renal function against the diagnostic value of contrast enhancement.

Since the early days of HOCM, it has been well established that, following distribution in the extracellular space, contrast agents are almost exclusively eliminated by the kidneys, via glomerular filtration, in direct proportion to the individual's glomerular filtration rate (GFR) (64). Early animal studies demonstrated the nephrotoxic potential of both HOCM and LOCM, particularly when combined with other renal stressors, such as ischaemia or dehydration, when injected directly into the renal artery or when administered repeatedly (65–67). Several case reports also documented instances of renal failure following intravenous contrast administration in urography and CT examinations (68–70).

Collectively, these findings contributed to a widely accepted consensus that contrast media pose a risk of inducing kidney injury, particularly in patients with preexisting chronic kidney disease (CKD). According to an article published by Stacul et al in 2011, reporting updated guidelines from the Contrast Media Safety Committee of the European Society of Urogenital Radiology patients with estimated GFR (eGFR) below 45 ml/min/1.73m^2 were identified as at risk of contrast media-induced nephropathy (CIN). Additional risk factors included diabetes mellitus, dehydration, moderate-to-severe congestive heart failure (New York Heart Association Grade 3–4), and advanced

age (71) A 2012 meta-analysis by Kooiman et al., encompassing 40 studies, reported a 6% overall incidence of CIN following intravenous administration of LOCM. Patients with CKD (eGFR <60 ml/min/1.73m^2) or diabetes mellitus exhibited a higher incidence of 9%. Recently updated guidelines from the Swedish Society of Urogenital Radiology designate eGFR thresholds of <30 mL/min/1.73 m² or <45 mL/min/1.73 m² as indicators of increased risk for acute kidney injury, depending on the presence of concurrent risk factors and the volume of contrast media administered (72).

Kidney Function and Acute Kidney Injury - Definitions

Kidney function is most often classified by GFR, either as an absolute value in ml/min or normalised to the body surface area, relative GFR, with the unit ml/min/1.73 m^2. eGFR means that kidney function is estimated from blood samples of either creatinine or cystatin C using formulae including other factors such as age and gender.(73)

According to the Kidney Disease: Improving Global Outcomes (KDIGO) guidelines a relative GFR > 90 is considered normal kidney function. Below this value there are different categories of decreased function, with the most important in this context being: Category G3b, GFR 30 – 45: Moderately to severely decreased kidney function; Category G4, GFR 15 – 29: Severely decreased kidney function and Category G5, GFR < 15: Kidney failure (73).

The KDIGO definition for AKI is: Increase in serum creatinine (SCr) by ≥ 26.5 μmol/l within 48 hours; or increase in SCr to ≥ 1.5 times baseline, which is known or presumed to have occurred within the prior 7 days; or urine volume < 0.5 ml/kg/h for 6 hours (74).

High-Z elements as contrast media

As outlined in the previous section, iodine serves as the attenuating element in currently available intravenously administered CM. Iodinated CM possess several advantageous properties, including high water solubility, molecular stability that allows for autoclaving, and complete renal elimination without metabolic alteration (75). However, from a purely physical standpoint, iodine is not the optimal element for CT contrast media.

With an atomic number (Z) of 53, iodine's K-edge at 33 keV lies below the energy of most photons in a CT scanner's polychromatic X-ray spectrum. Consequently, the attenuation effect of iodinated contrast media increases as the kVp-level of the CT scanner decreases. This property is exploited in clinical practice, where low kVp protocols are often used to maximize LOCM attenuation, particularly when aiming to minimise CM dose in patients with CKD. However, lowering the kVp also increases the proportion of photons that undergo photoelectric interactions with atoms in

patient tissues, leading to a higher absorbed radiation dose. Additionally, low kVp settings significantly degrade image quality in obese patients, where adequate penetration of X-rays is challenging as a smaller fraction of the photons reach the detector. Therefore, relying on iodine-based CM inherently limits optimisation of CT imaging.

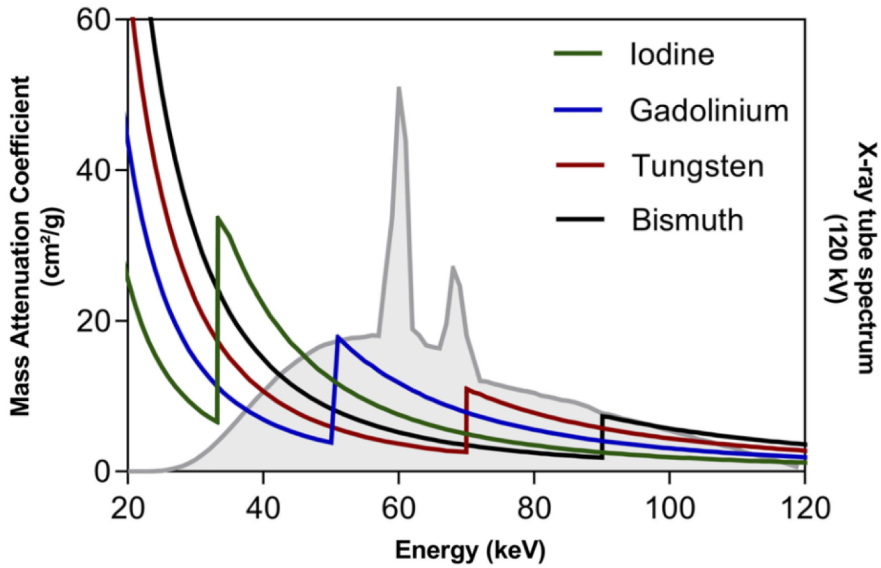

Figure 22 Photon energy spectrum at 120 kVp and mass attenuation coefficient at different keV of four elements

The mass attenuation coefficients (MAC) of iodine, gadolinium, tungsten (wolfram) and bismuth superimposed over a 120 kVp CT photon energy spectrum. The abrupt changes in levels of the MAC curves represent the K-edges. This figure illustrates the complex interaction underlying attenuation of different elements at a particular kVp-level. Copyright Wolters Kluwer Health, Inc. Jost G, New Contrast Media for K-Edge Imaging with Photon-Counting Detector CT. Vol. 58, Investigative Radiology. Lippincott Williams and Wilkins; 2023. p. 515–22.

An alternative approach involves exploring contrast media containing elements other than iodine. Ideally, such elements would have K-edge energies more closely aligned with the X-ray spectrum of CT scanners, maximizing attenuation efficiency without necessitating reductions in kVp (Figure 22). This concept presents an appealing opportunity for future contrast media development.

The X-ray attenuation characteristics of chemical elements are well-documented, with cross-sections and mass attenuation coefficients (indicating the probability of photon interaction at varying energy levels) readily available in reference tables (76). Elements with higher atomic numbers (high-Z elements) exhibit higher K-edge energies, more

closely aligning with the mean energy of CT X-ray spectra. In theory, these elements could attenuate photons more efficiently per atom and per unit mass compared to iodine, making them compelling candidates for alternative CM - up to Z ≈ 80, beyond which most elements are radioactive (76,77).

For several decades, research has explored the use of high-Z elements in CM, though efforts have been impeded by toxicity or prolonged bodily retention, hindering the development of viable agents (78).

Contemporary approaches to mitigate toxicity and enhance water solubility as well as renal excretion include nanoparticle formulation and the utilization of chelate-ligand complexes, as exemplified by gadolinium-based contrast media in magnetic resonance imaging (75,79). High-Z elements also constitute potential candidates for CM tailored for use in MD. Due to their high K-edge energies the X-ray properties of high-Z elements vary considerably from iodine at different kVp-levels. This facilitates separation of these potential CM from iodine. In 2012 two noteworthy papers were published, both exploring the use of dual contrast media - iodine and a high-Z element, either W or bismuth (Bi). Mongan et al demonstrated, in an animal model, the feasibility of separating two CM, either both intravascular, in different phases, or located in different organ systems, i.e. one given orally and the other intravascularly. Qu et al also explored the latter concept, but in a phantom study (80,81).

However, the complex interplay between CT X-ray energy spectra and the intricate attenuation curves of individual elements complicates the identification of elements optimally suited for use in alternative CM (82).

Aims

The overall aim of this thesis was to explore different aspects of optimisation of abdominal CT examinations, particularly regarding detection of liver metastases.

Specific aims of each paper included in the thesis:

Paper I To test the hypothesis that radiation dose and intravenous contrast medium dose can be balanced against each other, resulting in constant image quality - by evaluating an abdominal CT examination protocol in which patients were stratified by age. Young patients were examined using low radiation dose and high CM dose, while elderly were examined with high radiation dose and low CM dose.

Paper II Primary: To determine the potential of different high-Z chemical elements to be used alongside iodine in dual-CM, DECT examinations.

Secondary: To evaluate the possibility to separate the investigated elements using MD in an image-based software.

Paper III Primary: To investigate how different levels of simulated radiation dose reduction in abdominal CT affect detection and characterisation of hypovascular liver metastases.

Secondary: To evaluate the relationship between lesion size, CNR, radiation dose and lesion detection rate.

Paper IV Primary: To test the hypothesis that using a sharper convolution kernel in FBP, producing higher frequency noise and a better spatial resolution lead to improved detection of small, low-contrast lesions in low dose CT images, compared to the standard, softer kernel.

Secondary: To evaluate if using IR (ADMIRE) combined with standard as well as sharp kernel improves lesion detection, compared to FBP.

Materials and Methods

This doctoral thesis comprises four papers: two retrospective observational studies involving patients who underwent computed tomography (CT) examinations (**Papers I and III**), and two experimental phantom studies (**Papers II and IV**).

Study Population

Papers I and III were retrospective observational studies conducted on patients examined using the clinically implemented CT protocols at Skåne University Hospital, Malmö.

In **Paper I**, patients aged 16 years and above who underwent intravenous contrast-enhanced (CE) abdominal CT for suspected acute illness, between May and December 2009 were included. The protocol employed age-specific parameters by categorising patients into four age groups: 16–25, 26–50, 51–75, and >75 years. The target sample was 25 patients per group (100 in total).

In **Paper III**, patients who underwent CE thoracoabdominal CT during one of four discrete periods totalling 138 days (from 17 January 2011 to 4 September 2012) were included. The division into separate periods was due to repeated technical disruptions affecting image processing hardware. Inclusion criteria were patients undergoing follow-up examinations for known malignancy with hypovascular liver metastases. Patients with more than 10 metastases were excluded to minimise clustering bias. To mitigate memory bias during observer assessments, patients with large lesions (>3 cm), or distinctive features such as prior liver surgery, large calcified gallstones, or significant ascites were also excluded. The study aimed to enrol 20 patients with hypovascular liver metastases and 20 controls without liver metastases. A study coordinator (a gastrointestinal radiologist with 5 years of experience in abdominal CT) reviewed all images, including thin slices and multiplanar reconstructions, recording lesion location and maximum diameter in the transverse plane.

Lesion characterisation was performed collaboratively with a senior gastrointestinal radiologist (31 years' experience), incorporating data from all available prior

radiological examinations and referral information. The study coordinator also reviewed subsequent CT or MRI scans within 3 years of the index examination.

Phantoms

In **Paper II**, an online resource was used to assess the X-ray attenuation properties of high atomic number (high-Z) elements. The key parameters were the energy level of the K-edge and total cross section (cm^2/g) at specific keV values. Based on this data, five elements - gadolinium (Gd, Z=64), tantalum (Ta, Z=73), tungsten (W, Z=74), gold (Au, Z=79), and bismuth (Bi, Z=83) - were selected for comparison with iodine. Solutions (0.02 M) were prepared and placed into 20 ml plastic syringes. Due to solubility limitations, tantalum was suspended in a solid gelatinous medium at a similar concentration. To evaluate MD in detail, one syringe was prepared containing both a semi-cylindrical cast of the Ta-containing medium and a 0.02 M iodine solution. A non-anthropomorphic chest phantom (30 cm diameter, 10 cm length) made from Nylatron GSM Blue Nylon (Quadrant Engineering Plastic Products, Los Angeles, CA, USA) with cork inlays, housed the syringes in preformed slots.

In **Paper IV**, six homogeneous agar-based phantoms containing 3.5 mg I/mL iodinated contrast medium (Omnipaque, GE Healthcare, Amersham, United Kingdom) were fabricated in-house, each containing 3.5 mg I/mL iodinated contrast. To simulate low-contrast lesions, three phantoms included randomly placed 8 mm acrylic spheres, two contained 11 mm spheres (4D Modelshop, London, United Kingdom) and one served as a lesion-free control.

Image Acquisition

Papers I and III utilised a 16-slice CT scanner (SOMATOM Sensation 16, Siemens Healthcare, Forchheim, Germany) with a tube voltage of 120 kVp, pitch of 0.65, and collimation of 16 × 1.5 mm.

In **Paper III**, the tube load was 200 Quality Reference mAs, and the contrast dose was 420 mg I/kg body weight (Omnipaque, GE Healthcare, Amersham, UK)

In **Paper I**, both the tube load, which is linearly proportional to radiation dose, and contrast dose were adapted according to a theoretical model accounting for age-specific risk profiles. The rationale was that risks from ionizing radiation are greater for younger patients, while older patients more often have reduced renal function making them more susceptible to contrast induced acute kidney injury. Radiation dose (tube load in mAs) was plotted linearly proportional to age, with quantum noise inversely related to

the square root of the radiation dose. To counteract resulting changes in image noise, a matching age-adjusted contrast dose curve was applied. This aimed to maintain consistent CNR for all age groups. (Figure 23) The 51–75 years group, using parameters identical to the previous standard protocol, served as the reference.

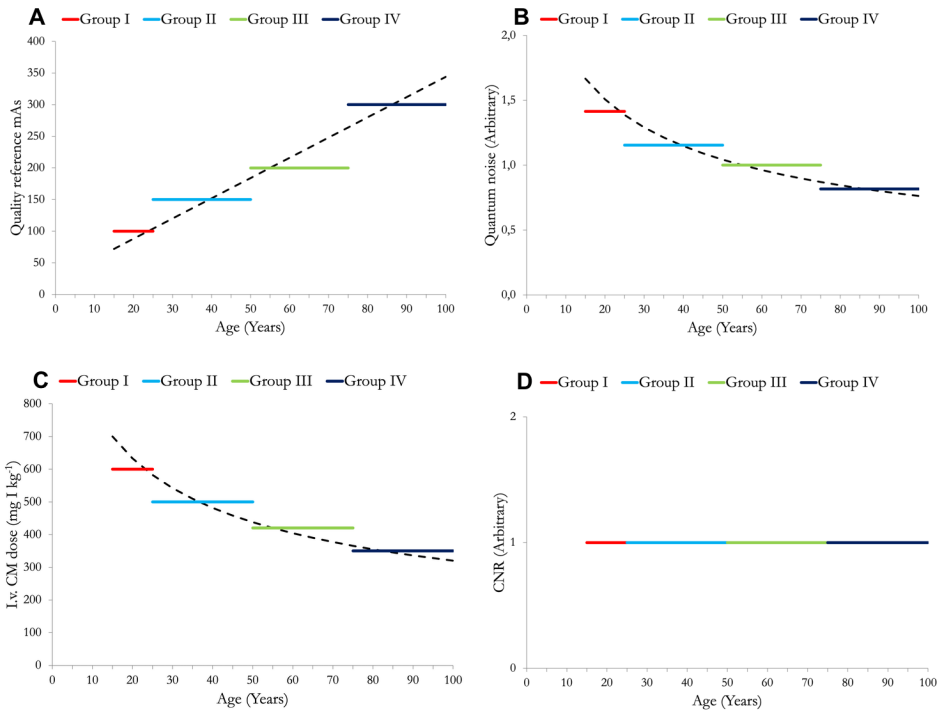

Figure 23 Theoretic model behind the age-stratified CT-protocol in Paper I

To determine the examination parameters for the age-stratified abdominal CT protocol in Paper I, this theoretical model was employed. The various age groups are represented by coloured bars: Group I (16–25 years), Group II (26–50 years), Group III (51–75 years), and Group IV (>75 years). The previously utilised protocol featured a tube load of 200 mAs. From this baseline, the radiation dose was plotted, increasing linearly with age (A). The resulting arbitrary quantum noise, which is inversely proportional to the square root of the radiation dose, is depicted in (B). To counteract the rising noise levels in younger groups and enable dose reduction in older individuals, the contrast media doses were adjusted to align with the noise curve (C). In theory, this approach maintains a consistent contrast-to-noise ratio (CNR) across all age groups (D). Copyright Marcus Söderberg. Reproduced with permission.

In **Paper III** artificial noise was added to the raw data prior to filtering and reconstruction, to simulate examinations performed at lower radiation dose levels. The software used was Dose Tutor version 4.7.0 (VAMP Gmbh, Erlangen, Germany), which had previously been validated at our institution and found to introduce noise with realistic magnitude and NPS (83). Images with simulated radiation dose levels of 100% (DL100); 75% (DL75); 50% (DL50) and 25% (DL25) were produced.

In **Paper II** the phantom containing the solutions of different elements was scanned using a dual source, dual energy scanner (Siemens SOMATOM Definition Flash, Siemens Healthcare, Forchheim, Germany). Scanning was performed using all available kVp-settings in single energy mode, as follows (the mean energy level of the X-ray spectrum given in parenthesis): 70 kVp (49 keV), 80 kVp (54 keV), 100 kVp (62 keV), 120 kVp (69 keV) and 140 kVp (76 keV). Two different dual energy settings were used: 80 kVp / 140 kVp and 80 kVp / Sn140 kVp. The "Sn140 kVp" setting means that an additional tin filter has been applied, more effectively filtering the low energy photons and thereby increasing the mean keV of the spectrum to 92 keV (Information on mean energies of the X-ray spectra was received in personal communication with Siemens Healthcare Sector Sweden on November 5, 2012). Tube load was set to 100 mAs for all single energy scans and for the high kVp tube in DE scans. Rotation time was 0.28 s and collimation 64 x 0.6 mm.

In **Paper IV** the phantoms were scanned in six positions, rotated 60° between scans, to produce multiple images with varying lesion locations. A dual source CT scanner (Siemens SOMATOM Drive, Siemens Healthineers, Forchheim, Germany) was used. Low radiation dose scans were performed of the phantoms in all positions to yield images with a high level of image noise, using the following parameters: tube voltage 90 kVp, tube load 10 mAs, rotation time 0.5 s and pitch 1.4. A subsequent high-dose scan generated low-noise reference images.

Image Reconstruction

In **Papers I, II, and III**, images were reconstructed using FBP with kernel B30f, 5 mm slice thickness, and a 512 × 512 image matrix size.

In **Paper IV**, three different convolution kernels were employed for image reconstruction. Br38, the standard kernel used in clinical practice, served as the reference. Two sharper kernels, Bf42 and Br43, were selected to test the hypothesis that higher-frequency noise with finer texture may improve the detection of small, low-contrast lesions. Each of the three kernels was applied using FBP as well as ADMIRE at strengths 3 and 5 (maximum strength = 5), resulting in a total of nine reconstruction methods. Images were reconstructed in 3 mm slices with a 2 mm slice interval, and the image matrix size was 512 × 512.

Objective Image Quality Evaluation

In **Papers I and III**, a region of interest (ROI) was placed in a homogeneous region of the right liver lobe in all patients, and simulated dose levels, to record CT-numbers and SD as a measure of noise. Measurements in **Paper I** were performed using the institutional Picture Archiving and Communication System (Sectra PACS, Sectra, Linköping, Sweden), while **Paper III** employed OsiriX DICOM viewer (version 3.9.2, Geneva, Switzerland).

In **Paper I** SNR were calculated by dividing the CT-number in the right liver lobe by the SD representing the noise. Due to a lack of liver lesions a hypothetical hypovascular liver metastasis with a CT-number of 40 HU was used for CNR calculation.

In **Papers III** and IV CT-numbers were measured by placing a ROI within all lesions. An additional ROI was placed in a homogeneous area in the adjacent parenchyma/medium measuring the CT-number, again with SD representing noise. CNR was calculated as the difference in CT-numbers divided by noise.

Noise Power Spectrum

In **Paper IV** the NPS-curves of the nine different reconstruction methods were generated using Auto QA Plus (version 1.8.11, QA Benchmark, LLC, Frederick, MD, USA). To generate NPS of all reconstruction methods, scans of the control phantom were used excluding 5 slices in either end of the phantom. Measurements of the central 29 slices were averaged to yield representative NPS-curves. The area under the curve (AUC) was calculated using the trapezoidal rule in R (R Foundation for Statistical Computing, Vienna, Austria). Frequencies at the 10th, 50th, and 90th percentiles of the AUC were determined to help describe curve shapes.

Dual-Energy Ratios and Material Decomposition

In **Paper II** dual-energy ratios of the investigated elements were calculated as an objective descriptor of attenuation properties at different kVp-settings. The difference in attenuation between different elements, when exposed to distinct X-ray energy spectra, is the foundation of MD in DE CT. Therefore, the numerical value given by a ratio of the attenuation at low and high kVp can be used to compare elements, indicating the potential for separation using MD. Dual-energy ratios were calculated for the following kVp-combinations: 80/140; 80/Sn140, 70/140 and 70/Sn140.

MD experiments were performed using "VEn workflow, advanced VEn tool" in the software Aquarius iNtuition viewer (TeraRecon, Foster City, California, USA). DE data were loaded into the software and ROIs placed within the element-containing syringes, two at a time. As the most useful MD-application would be to separate a distinct element from iodine, MD of the five evaluated elements from iodine was investigated. Scatterplots with low kVp on the Y-axis and high kVp on the X-axis were generated.

A manually placed discriminatory line through origo was placed between elements in the scatterplot, with voxels in image space colour-coded (green/red) based on their position relative to the line. (Figure 17)

Subjective Image Quality Evaluation

Papers I, III, and IV employed ViewDEX software (Region Västra Götaland and University of Gothenburg; versions 2.0 and 2.57) for observer studies. ViewDEX, an acronym for "Viewer for Digital Evaluation of X-ray images", integrates a DICOM viewer with customisable tools for image evaluation and lesion localisation. Thus, the software makes it possible to set up different reader tasks in different studies.

In **Paper I** a Visual Grading Characteristics (VGC) study was conducted with four readers (radiologists with 3 – 20 years of experience reading CT images) grading seven image quality criteria in pseudonymised images from all age-groups. The image quality criteria were selected from the European guidelines on quality criteria for CT and are displayed in Table 1 (84). A five-grade Likert scale was used, with the following grades: 1 – unacceptable; 2 – substandard; 3 – acceptable; 4 – above average and 5 – superior. Readers completed a calibration session and were allowed to adjust image settings while reading the images. A sub-analysis included 20 patients aged 16 – 25 and examined using the previous standard protocol employing the same parameters as age-group 51-75. This sub-group was compared to age groups 16 – 25 years and 51 – 75 years to analyse the impact on image quality from radiation dose reduction versus age-dependent differences in body constitution, i.e. the smaller amount of intraabdominal fat in young patients.

Table 1 Image quality criteria from the European guidelines on quality criteria for CT

Number	Image Quality Criteria
1	Visually sharp reproduction of liver parenchyma and the intrahepatic portal veins
2	Visually sharp reproduction of the pancreatic contours
3	Visually sharp reproduction of the kidneys and proximal ureters
4	Reproduction of the gallbladder wall
5	Visually sharp reproduction of the right adrenal gland from adjacent structures
6	Visually sharp reproduction of the structures in the liver hilum
7	Reproduction of of the ductus choledochus in the pancreatic parenchyma

Lesion Localisation and Characterisation

In **Papers III and IV** ViewDEX was set up to facilitate lesion localisation studies.

In **Paper III**, five radiologists (4–20 years of experience) localised liver lesions and rated their malignancy probability on a 5-grade Likert scale: 5 – very high probability; 4 – high probability; 3 – moderate probability; 2 – low probability and 1 – very low probability.

160 image stacks were read in total, divided into four sessions of 40 image stacks, presented in random order, with at least one month interval between sessions to minimize memory bias. Patients were included once per session and presented in random order. A localization mark placed within a lesion was considered a true positive marking and a mark placed outside of a lesion was recorded as a false positive.

The results from the observer study in **Paper III** were analysed using Jackknife Free-response Receiver Operating Characteristics (JAFROC) in a non-inferiority analysis (see Statistical methods below for further description).

Lesion detection and characterisation were further explored in **Paper III** by applying two different cut-off levels to the Likert scale: below grade 3 and below grade 4. This approach was intended to simulate clinical practice, in which radiologists typically report lesions with a moderate or higher probability of malignancy as suspicious. Fractions of metastases graded above the cutoff levels were compared between the simulated radiation dose levels. The 100% radiation dose level served as reference in all analyses.

To assess whether the relationship between lesion size, CNR and lesion detection remained consistent at different dose levels, lesions were stratified into nine groups based on size and CNR. The proportion of correctly localised lesions within each subgroup was calculated.

In **Paper IV**, 8-slice image stacks—each containing either one lesion or no lesion—were extracted from the full image datasets using the free software Horos (version 3.3.6;

Nimble Co LLC d/b/a Purview, Annapolis, MD, USA). These image stacks were imported into ViewDEX for the observer study. A pilot study involving two readers who assessed 45 image stacks was first conducted. Based on the results, a sample size analysis using RJafroc (R Foundation for Statistical Computing, Vienna, Austria) indicated that a study with five readers and 80 cases would achieve a statistical power of 0.854, assuming a significance level of 0.05 and an effect size of 0.05.

Five readers were subsequently recruited: four radiologists with 3 to 20 years of experience in CT interpretation, and one CT-specialised medical physicist with 15 years of experience. Eighty 8-slice image stacks were selected for the observer study from images reconstructed using each of the nine reconstruction methods, resulting in a total of 720 unique image stacks. An additional 80 image stacks were duplicated to assess intra-reader agreement.

The image stacks were evaluated in ViewDEX across five reading sessions, each comprising 160 image stacks, presented in random order. A minimum interval of one week between sessions was enforced to reduce memory bias. Reader markings were compared with lesion locations identified in the corresponding high-dose reference scans. Markings placed within a lesion boundary were classified as true positives; those outside lesions were considered false positives (Figure 24).

A separate analysis of lesion detection performance among reconstruction methods was conducted by calculating and comparing the proportion of true and false positive markings with a confidence score of 2–4 on the Likert scale.

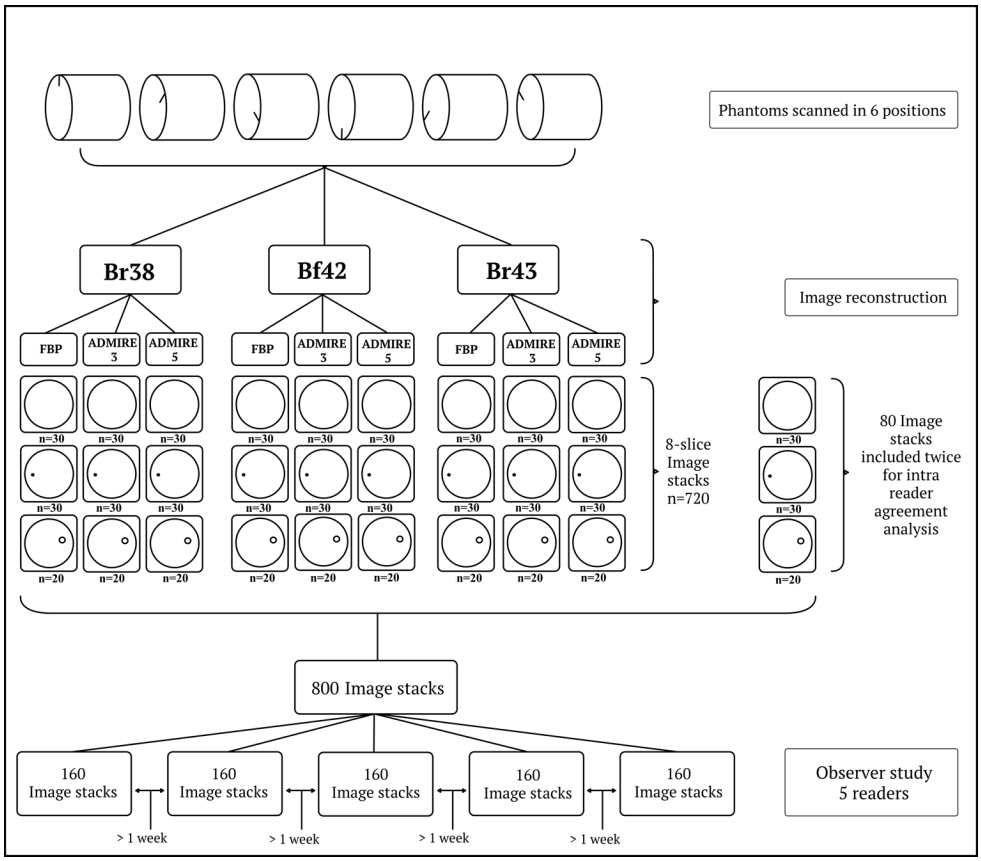

Figure 24 Overview of study in Paper IV
Copyright: The Authors.

Ethical considerations

The studies described in **Papers I and III** are retrospective observational studies involving patients who had previously undergone standard clinical imaging procedures at our institution. No modifications to examination techniques or patient care were made for the purposes of these studies. The age-stratified abdominal CT protocol evaluated in **Paper I** had already been implemented as standard clinical practice prior to the initiation of the study. Nevertheless, the selection and inclusion of patients in these studies raise considerations regarding patient integrity. This must be balanced against the benefits of conducting research potentially improving CT imaging protocols, thereby enhancing the quality of care for future patients. All images were

pseudonymised following selection, and patient-identifiable information was securely stored in coded lists.

The studies were approved by the Regional Ethics Committee in Lund, and the requirement for informed consent was waived (Ethical approvals: Dnr 2011/571 and Dnr 2014/266). The studies presented in **Papers II and IV** are phantom-based and, therefore, did not require ethical approval.

Statistical methods

Visual Grading Characteristics (VGC)

VGC was used in **Paper I** to compare and analyse the image quality between the four different age groups examined using different parameters. VGC is a non-parametric, rank-invariant method suitable for analysing ordinal data such as grades on a Likert scale from an observer study (40). This is important as it is incorrect to calculate means or assume normal distribution of ordinal data. A VGC-curve is produced in a procedure similar to receiver operating characteristic (ROC). To compare two different types of images, e.g. age-groups in **Paper I**, ordinal rating data from the different age-groups are plotted against each other in a diagram to produce a VGC-curve. The evaluated image type on the y-axis and the reference on the x-axis, both with a range from 0 to 1. Data are plotted cumulatively from origo starting with the highest ratings, with the curve ending up at the point (1, 1) in the top right corner. A line along the diagonal of the diagram means equal performance of the evaluated image types. An AUC larger than 0.5 means that the evaluated system performs better. Observers will interpret a rating scale somewhat differently, why ratings cannot be compared across readers. Individual AUC for each reader and image quality criterion is therefore produced. The mean and confidence interval (CI) are then determined using a statistical resampling method called bootstrapping. The software "VGC analyzer" was used (85).

Jackknife Alternative Free-Response Operating Characteristic (JAFROC)

The studies in **Papers III and IV** investigated lesion localisation and grading. JAFROC is an appropriate method for data analysis in this type of studies. In JAFROC the figure-of-merit (FOM) is the quantitative metric of observer performance. q is equivalent to the AUC of a ROC-curve, where, for each rating scale level, the fraction of true positive lesion localisations (relative to all lesions) is plotted on the y-axis against the fraction of cases with at least one false positive marking at that rating on the x-axis. Thus, q can be defined as the likelihood that a true positive localization is rated higher than any false

positive localisation. The plotting of the ROC-curve can be described as starting at origo, highest ratings first and then cumulatively and stepwise adding true and false positives with lower rates. This way correct localisations with high ratings are awarded by increasing the AUC while false positives with high ratings and missed lesions (false negatives) are penalised by lowering the AUC. JAFROC calculates an AUC for each reader and evaluated modality. The jackknife-procedure is a type of resampling in which one case is excluded while a new AUC (so called pseudovalue) is calculated for the remaining cases. This is repeated excluding all cases one at a time and the difference in mean pseudovalue between the evaluated modalities is then analysed using analysis of variance (ANOVA). ANOVA performs significance testing on a global level as well as between all modalities compared to one another. A difference between two modalities is only deemed significant if the p-value of the comparison of their FOMs and the global p-value of the ANOVA test both are < 0.05 (86).

There are a few options within the JAFROC-methodology. In "standard JAFROC" only false positive localisations from non-diseased, control, cases are included in the analysis. "JAFROC1" is the other variant, where false positive localisations from all cases are included. This yields a higher statistical power. Initially the use of JAFROC1 was not recommended by the developer as it was not deemed reliable. However, in a later simulation JAFROC1 was validated and approved for use (87). There are also "weighted" versions of JAFROC and JAFROC1. This means that lesions are weighted in a way that compensates for the varying number of lesions per case, so that each patient has equal influence on the results. This is desirable as multiple lesions in the same case cannot be regarded as independent from each other (87).

JAFROC was developed by D. Chakraborty at the University of Chicago. In **Paper III** the JAFROC software for Windows (version 4.2.1) was used, in **Paper IV** RJafroc package version 2.1.2 in R (R Foundation for Statistical Computing, Vienna, Austria).

The post hoc sample size analysis in **Paper III** was performed using the "Multi-reader sample size program for diagnostic studies" software by Hillis and Schartz at the Medical Image Perception Laboratory at the University of Iowa (88).

Analysis of variance and Tukey's test

In **Paper I**, the difference in means of SNR and CNR between the age-groups was analysed using ANOVA and Tukey's test. ANOVA is a parametric statistical method for comparison of differences between the means of multiple groups. The analysis calculates the ratio of the variance between the groups to the variance within groups. The resulting numerical value is the F-statistic which analysed together with the degrees of freedom gives the significance level of the null hypothesis test that there is no difference between the groups. A statistically significant result in an ANOVA analysis

indicates a significant difference between any of the groups included but does not specify where this significant difference is to be found. Therefore, if ANOVA yields a significant result, a post hoc analysis needs to be carried out, such as Tukey's test. Tukey's test compares all groups to each other specifying which are significantly different from each other, while at the same time correcting for multiple significance testing (89).

Intraclass Correlation Coefficient

In **Papers III and IV**, the Intraclass Correlation Coefficient (ICC) was employed to evaluate inter-reader agreement. In **Paper IV**, the ICC was additionally used to assess intra-reader agreement. The ICC is computed as the ratio of variance arising from differences between cases to the total variance, which encompasses both case and reader variance. When reader agreement is high, the variance attributable to differences between readers is minimal, thereby reducing the denominator in the calculation and yielding a higher ICC value. Consequently, the ICC ranges from 0 to 1, with higher values indicating greater agreement (90,91).

Several forms of ICC are available, each appropriate for different study designs. For the inter-reader analyses, a two-way random-effects model with average measures and a consistency definition was used. For the intra-reader analysis, a two-way mixed-effects model with single measures and an absolute agreement definition was applied.

A commonly cited guideline for interpreting ICC values was proposed by Koo and Li (2016): < 0.50: Poor reliability; 0.50–0.75: Moderate reliability; 0.75–0.90: Good reliability and > 0.90: Excellent reliability (90).

Chi-squared test

The chi-squared (χ^2) test was used in **Paper III** to evaluate differences in the proportions of detected lesions between the various radiation dose levels. The χ^2 test is a statistical method designed to assess differences in proportions of categorical variables between groups. In its most common application, data are arranged into a 2 x 2 contingency table, where observed numbers within each cell are compared to expected numbers under the null hypothesis of no difference in proportions. For each cell, the squared difference between observed and expected frequencies is divided by the expected frequency, and these values are summed across all cells. The resulting test statistic, combined with the degrees of freedom, is compared to the chi-squared distribution to determine the p-value. The test assumes sufficiently large sample sizes, with a minimum expected number of five in each cell, and independent observations.

The test assumes sufficiently large sample sizes, with an expected frequency of at least five in each cell, and that the observations are independent (89).

McNemar's test

In **Paper IV**, McNemar's test was used to analyse differences in rates of true and false positive markings between the different reconstruction methods. McNemar's test is applicable to paired, dichotomous data and uses only discordant pairs in a χ^2 analysis to analyse if there is a statistically significant difference between groups (89).

Student's t-test

The Student's t-test is a classical parametric test commonly used to determine whether there is a statistically significant difference between the means of two independent groups. It is suitable for small sample sizes and assumes that the data are normally distributed and that the groups are independent.

In **Paper III**, the Student's t-test was used to assess whether the mean number of incorrectly graded benign lesions and false-positive localisations differed significantly between the various radiation dose levels, based on assessments from the five readers.

Shapiro-Wilk test

The Shapiro–Wilk test is used to assess the normal distribution of a sample. If the resulting p-value is >0.05 the sample can be considered to follow normal distribution. In **Paper IV** the Shapiro-Wilk test was used to test the normality of the measurements of CT-numbers, noise and CNR (89).

Mann-Whitney U-test and Wilcoxon signed rank test

As some of the data from measurement of CT-number, noise and CNR in **Paper IV** did not meet the assumption of normal distribution, it was not appropriate to use t-test and paired t-test. Instead, the non-parametric counterparts Mann-Whitney U-test and Wilcoxon signed rank test were used. The Mann-Whitney U-test compares two independent samples by analysing their distribution in relation to one another. Wilcoxon signed rank test compares the if the median of the differences of each individual pair differs significantly from zero (89).

Results

Paper I

One hundred patients were recruited and allocated to four age groups: 16 – 25 years (Group 1); 26 – 50 years (Group 2); 51 – 75 years (Group 3) and >75 years (Group 4). Gender distribution within the groups, radiation dose and CM dose is presented in Table 2. The implementation of the investigated examination protocol, designed to reduce radiation dose for younger patients and IV CM dose for the elderly, resulted in a 58% reduction in radiation dose for patients in Group 1 and an 18% reduction in CM dose for those in Group 4.

Table 2. Gender distribution, mean radiation dose and IV contrast medium dose.
Presented for the four age groups, percentage difference to reference group 3 also included.

Group	Age (years)	Female-to-Male Ratio	CT Dose Index$_{vol}$ (mGy)	Effective Dose (mSv)	Change in Radiation Dose (Group 3 for reference)	IV Contrast Medium Dose (mg I/kg)	Change in IV Contrast Medium Dose (Group 3 for reference)
1	16 - 25	15:10	4.6 ± 0.62	3.6 ± 0.60	- 58%	594 ± 11	+ 42%
2	26 - 50	18:7	8.1 ± 1.3	6.6 ± 1.3	- 22%	492 ± 25	+ 18%
3	51 - 75	13:12	10.7 ± 1.4	8.5 ± 1.3	REFERENCE	418 ± 5.2	REFERENCE
4	>75	16:9	15.9 ± 3.0	12.4 ± 3.2	+ 46%	344 ± 15	- 18%

Example images depicting an axial slice through the mid-portion of the liver for each group are shown in Figure 25. Notably, higher contrast enhancement in abdominal organs and blood vessels is observed in Group 1, diminishing with increasing age. As per the protocol design, this enhanced contrast is accompanied by an elevated image noise level, attributable to the reduced radiation dose, in Groups 1 and 2. Conversely, the reduced contrast enhancement in Group 4 is offset by a lower noise level. Objective image quality metrics, including mean CT-number in liver parenchyma, image noise, CNR, and SNR, are reported in Table 3, with CNR and SNR also illustrated in Figure 26.

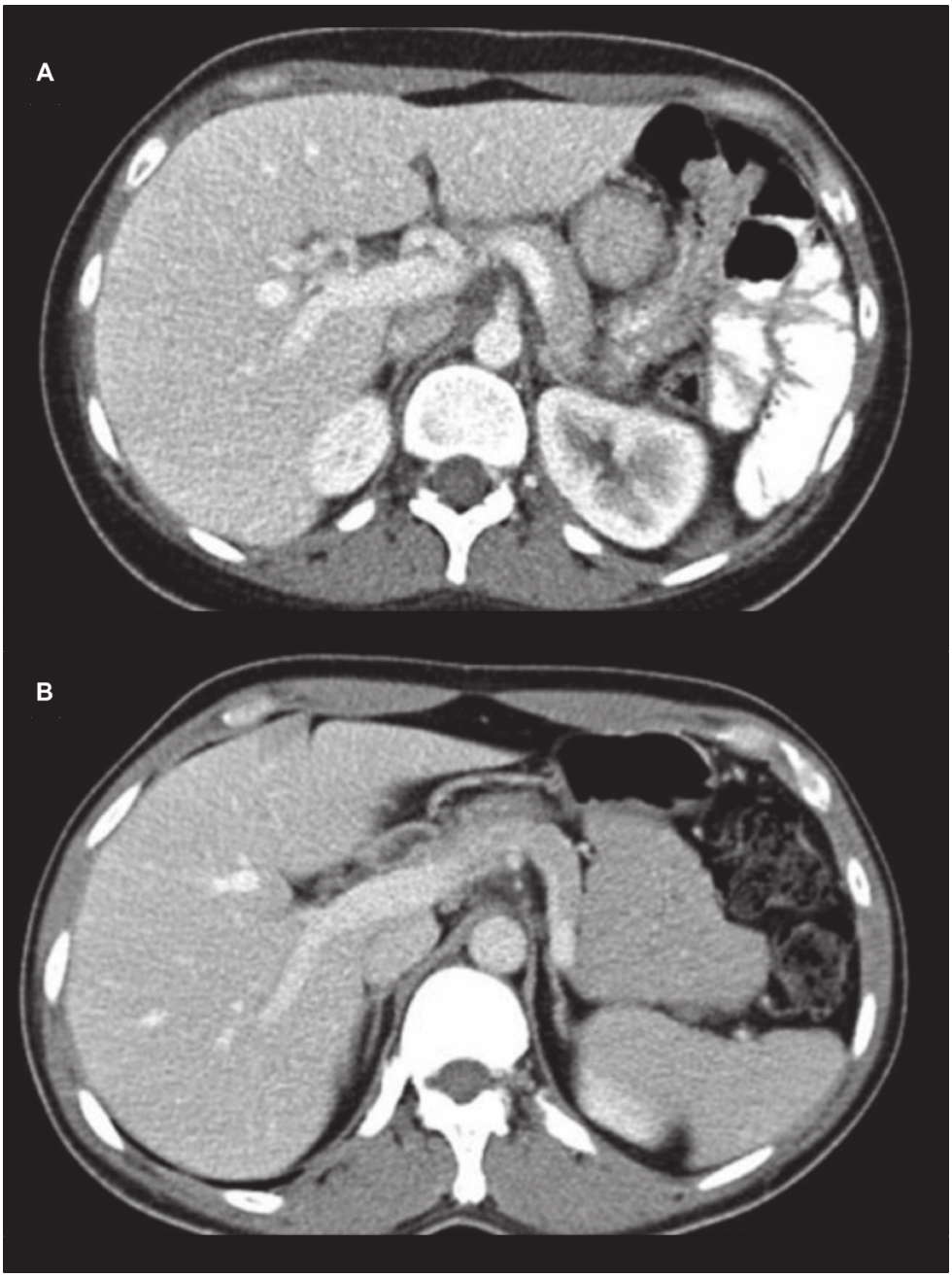
A
B

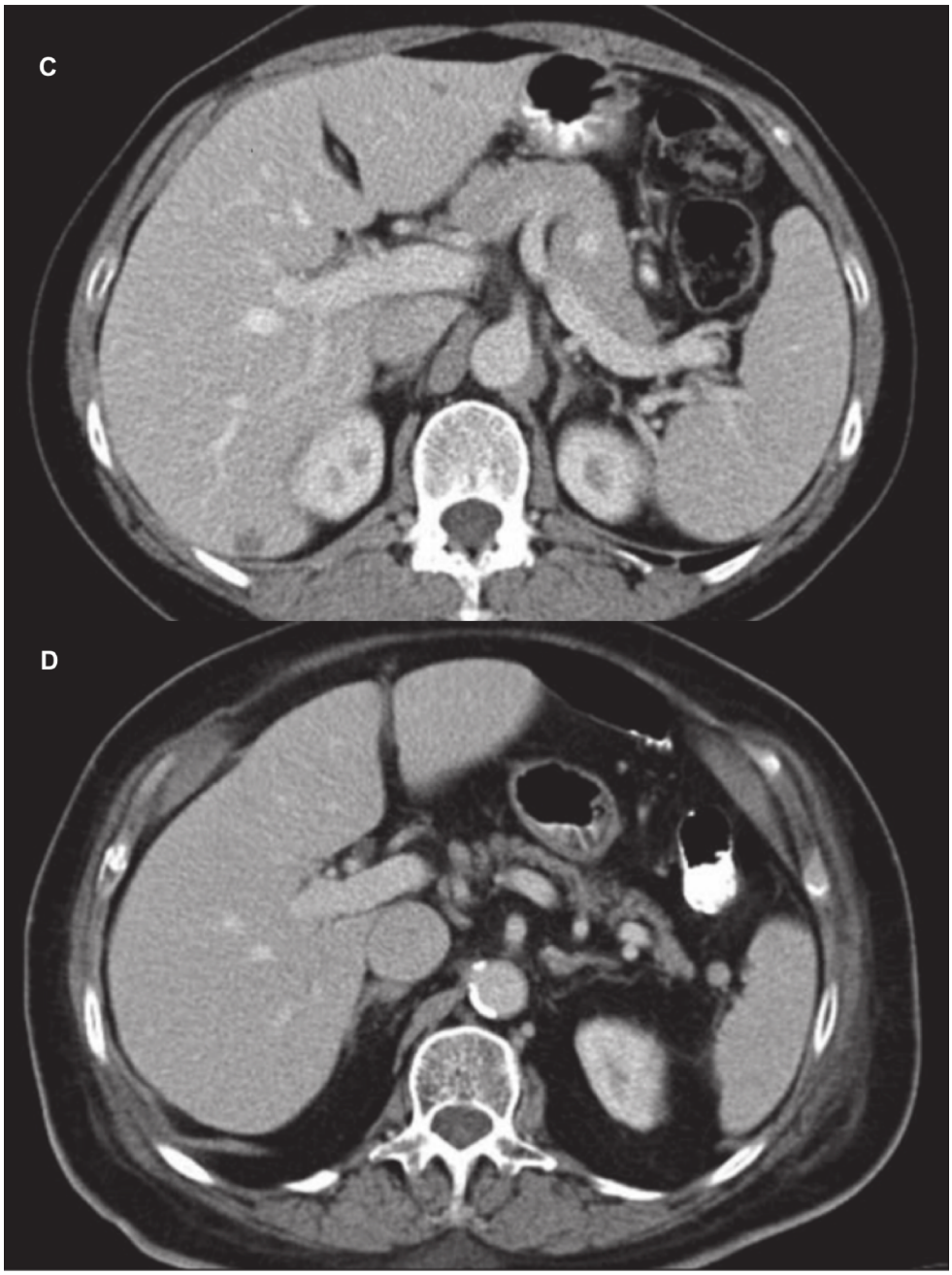

Figure 25 Image examples of patients in the four age-groups
Axial slices at the level of the portal vein are presented, with one patient from each age group included for comparison: A = Group 1, B = Group 2, C = Group 3, and D = Group 4. Observe the variations in noise levels and contrast enhancement between the age groups. Copyright: The authors

Table 3 Mean CT-number in liver parenchyma, Noise, CNR and SNR.
Presented for the four age groups.

Group	Mean CT-number liver (HU)	Noise (HU)	CNR	SNR
1	123 ± 14	16.4 ± 1.7	5.1 ± 0.9	7.6 ± 1.0
2	105 ± 14	14.9 ± 2.3	4.5 ± 1.3	7.3 ± 1.6
3	94 ± 9	12.8 ± 1.9	4.3 ± 1.1	7.5 ± 1.5
4	87 ± 10	10.7 ± 1.5	4.6 ± 1.2	8.4 ± 1.7

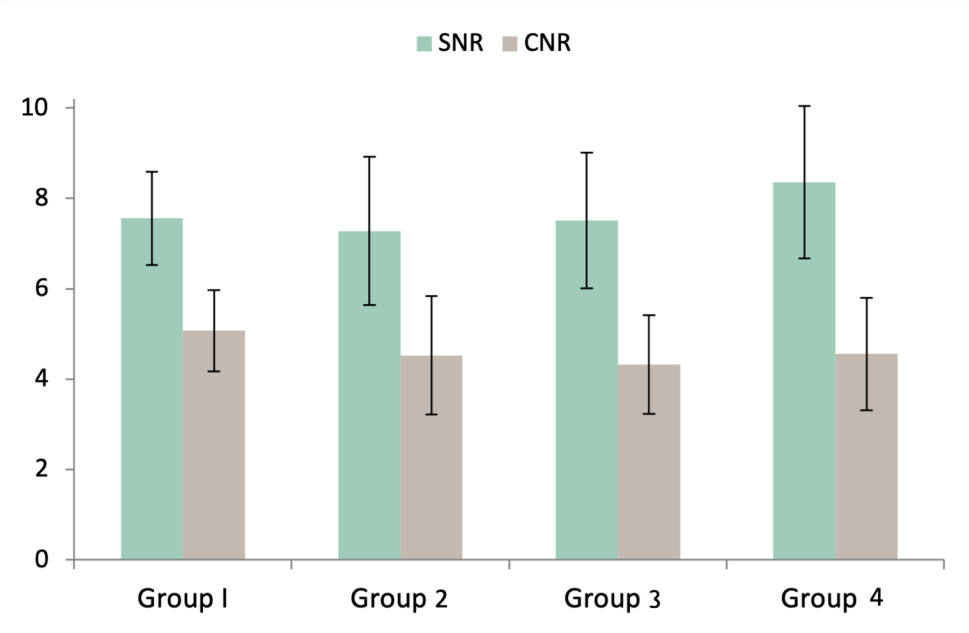

Figure 26 Signal-to-noise ratio (SNR) and contrast-to-noise ratio (CNR)
Mean liver SNR and mean CNR calculated using the contrast between liver parenchyma and a hypothetical metastasis with CT-number=40. Error bars indicate ±1 standard deviation (SD). Copyright: The Authors.

VGC AUC values for each image quality criterion, combined across all readers, are presented in Figure 27. For Group 1, image quality was rated inferior to the reference (Group 3) for all seven criteria, with significantly lower AUC values for four criteria. For Group 2, the AUC was lower than Group 3 in six of seven criteria, achieving significance for only one criterion. No discernible difference was observed between Groups 3 and 4.

When analysing the percentage of grades rated as "acceptable" or higher (3–5 on the Likert scale) for all readers, the results for the respective groups were: Group 1 – 71%; Group 2 – 80%; Group 3 – 85%; and Group 4 – 83%.

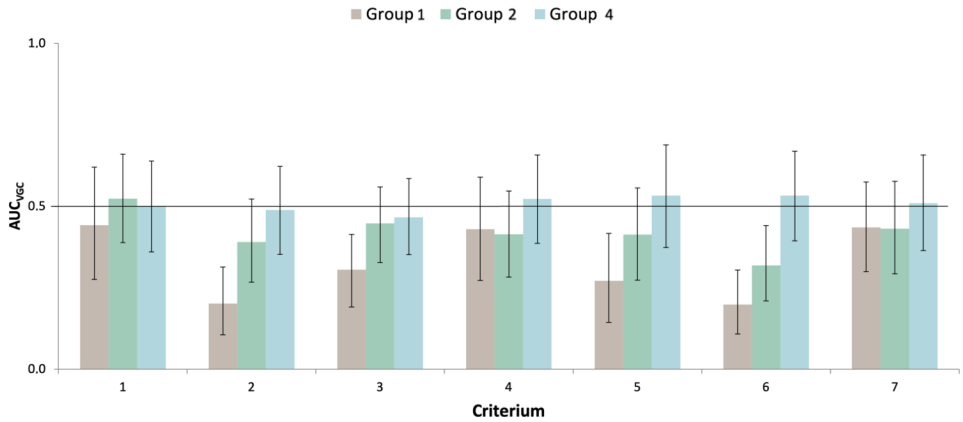

Figure 27 Area under the curve (AUC) values of visual grading characteristic (VGC) analysis
The area under the curve for the groups 1, 2 and 4 when compared to the reference group (Group 3). AUCs for all seven image quality criteria are included. Error bars indicate 95% confidence interval (CI), if this does not cover 0.5 the difference between the evaluated and reference system is significant. Subjective image quality was graded worse for the group with the lowest radiation dose (Group 1), reaching significance for four criteria out of seven. In group 2 image quality was rated significantly worse for one criterion. No difference was seen between group 3 and 4. Copyright: The authors.

A retrospective inter-reader agreement analysis, conducted using ICC following the publication of **Paper I**, demonstrated "good reliability" among the four readers (ICC = 0.79, 95% CI: 0.67–0.86, with two-way random effects and absolute agreement; ICC = 0.84, 95% CI: 0.82–0.86, with two-way random effects and consistency).

Paper II

The CT-numbers of the investigated elements at all available kVp settings are presented in Figure 28. Notably, the curves for Ta, W, and Au remain approximately horizontal, indicating similar attenuation of the X-ray spectrum at both low and high kVp settings. In contrast, the curves for iodine, Gd, and Bi exhibit a decline in CT-number with increasing X-ray energy, with iodine displaying the most pronounced relative difference between low and high kVp levels. This relative difference in CT-numbers between low and high kVp levels corresponds to the DE ratios of the elements. DE ratios for the existing DE settings at the time of the study (80 kV/140 kV and 80 kV/Sn140 kV), as well as simulated DE settings (70 kV/140 kV and 70 kV/Sn140 kV), are detailed in Table 4

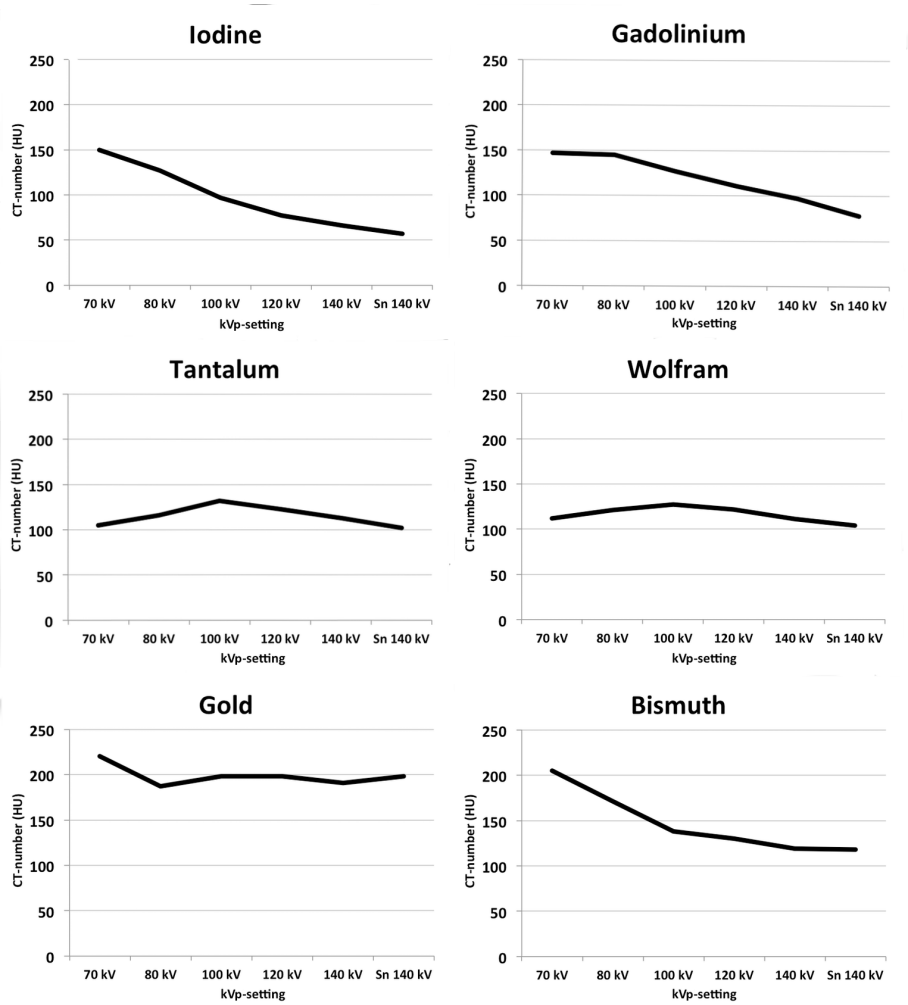

Figure 28 CT-numbers at different peak kilovolt (kVp)-levels

One chart is provided for each investigated element, displaying their CT-numbers at all available kVp levels. Iodine displays the largest relative difference in CT-numbers between low and high kVp settings. Meanwhile, tantalum, tungsten (wolfram), and gold exhibit similar CT-numbers across all kVp levels.Gadolinium and bismuth fall in between, with a modest increase in CT-numbers at lower kVp settings. From: Fält T, et al. Material Decomposition in Dual-Energy Computed Tomography Separates High-Z Elements From Iodine, Identifying Potential Contrast Media Tailored for Dual Contrast Medium Examinations. Journal of Computer Assisted Tomography. 2015;39(6):975–80. Reproduced with permission from Wolters Kluwer Health Inc.

Table 4 K-edges and DE ratios for the examined elements

Chemical Element	K-edge keV	80 kV/140 kV	80 kV/Sn140 kV	70 kV/140 kV	70 kV/Sn140 kV
I	33.2	1.9	2.2	2.3	2.6
Gd	50.2	1.5	1.9	1.5	1.9
Ta	67.4	1.0	1.1	0.9	1.0
W	69.5	1.1	1.2	1.0	1.1
Au	80.7	1.0	0.9	1.2	1.1
Bi	90.5	1.4	1.4	1.7	1.7

Iodine has high DE ratios at all settings, well separated from the DE ratios of Au, Ta, and W. Gd and Bi have DE ratios closer to that of I.

In Figure 29, a scatterplot from the MD software is presented, illustrating the positions of iodine and Au within the chart and the placement of the discriminatory line to achieve optimal separation between these elements in the colour-coded images.

Figure 30 depicts varying degrees of element separation by MD. Au and iodine were fully distinguished by the software, coded in red and green respectively. Bi and iodine exhibited slightly less effective separation, with noticeable noise evident in the colour-coding of iodine. Inferior separation was observed for Gd and iodine. The greater the similarity in DE ratios between two elements, the more pronounced the adverse effect of image noise, significantly impairing the separation of Gd and iodine.

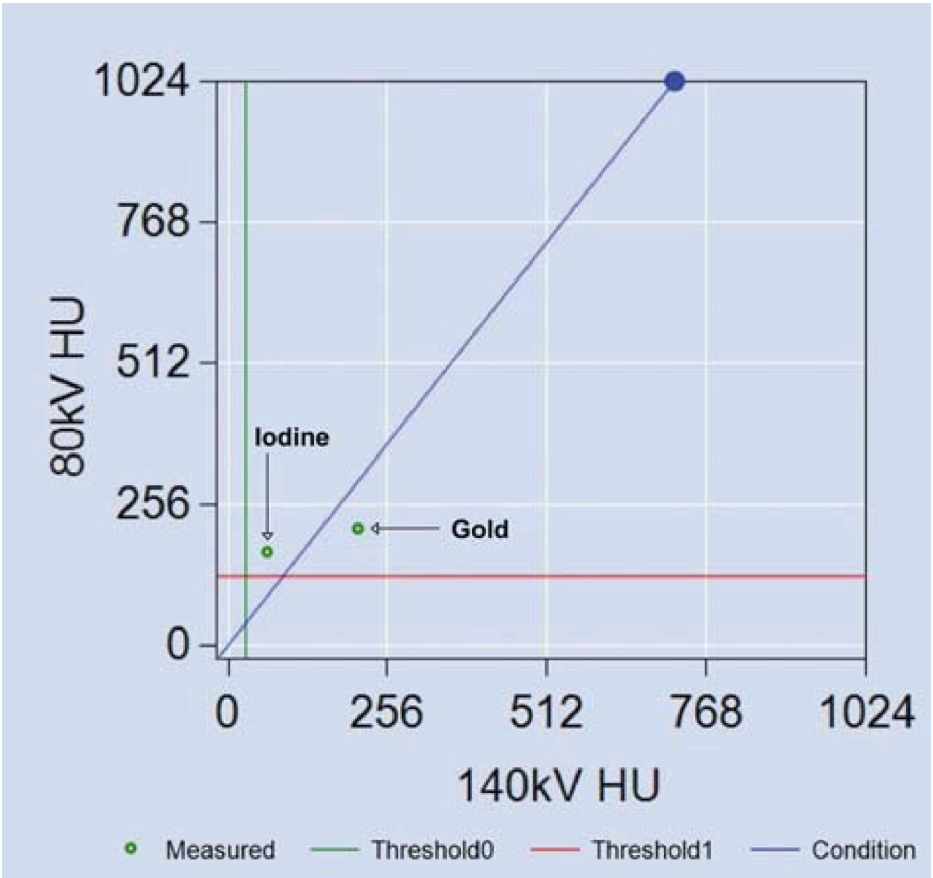

Figure 29 Scatterplot from material decomposition (MD) software

An example of scatterplot produced by the MD software. Iodine and gold are located well apart in the plot due to their varying CT-numbers at low and high kVp-levels. i.e. different dual energy-ratios. The blue discriminatory line was placed manually as were the threshold values. Iodine and gold were successfully separated and colour-coded by the system. From: Fält T, et al. Material Decomposition in Dual-Energy Computed Tomography Separates High-Z Elements From Iodine, Identifying Potential Contrast Media Tailored for Dual Contrast Medium Examinations. Journal of Computer Assisted Tomography. 2015;39(6):975–80. Reproduced with permission from Wolters Kluwer Health Inc.

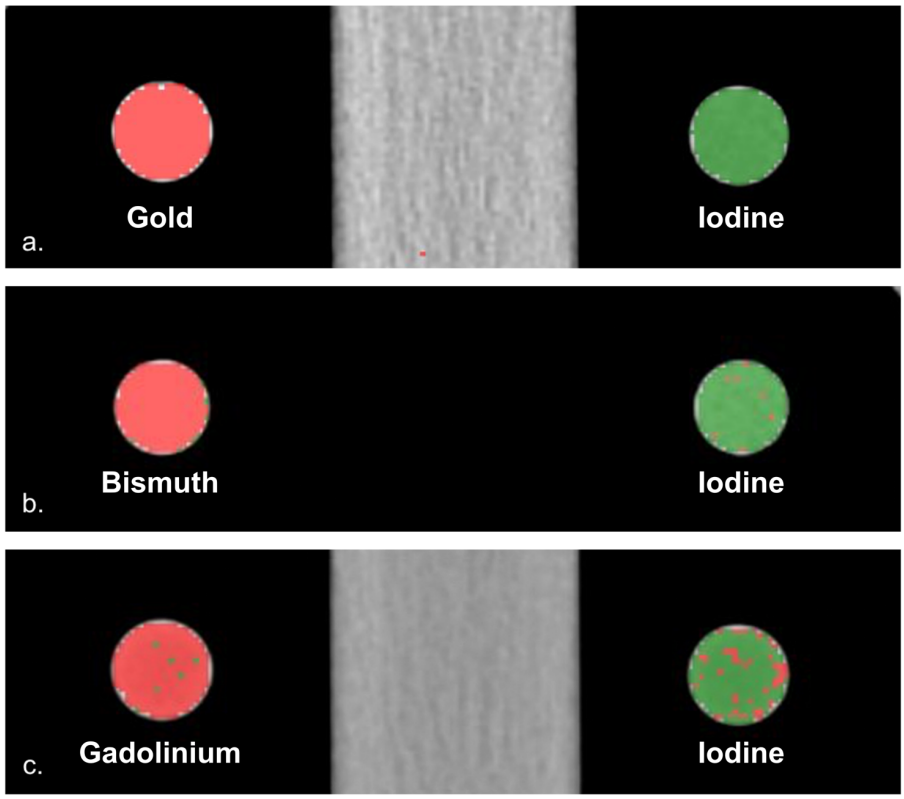

Figure 30 Colour-coded material decomposition (MD) images

CT images of the phantom are presented with overlaid colour-coded MD information. Note the three distinct levels of MD effectiveness. Iodine and gold are fully separated and iodine and bismuth are nearly completely separated, though noise is starting to visibly impair the distinction. Iodine and gadolinium exhibit poor separation, marked by noticeable noisiness. From: Fält T, et al. Material Decomposition in Dual-Energy Computed Tomography Separates High-Z Elements From Iodine, Identifying Potential Contrast Media Tailored for Dual Contrast Medium Examinations. Journal of Computer Assisted Tomography. 2015;39(6):975–80. Reproduced with permission from Wolters Kluwer Health Inc.

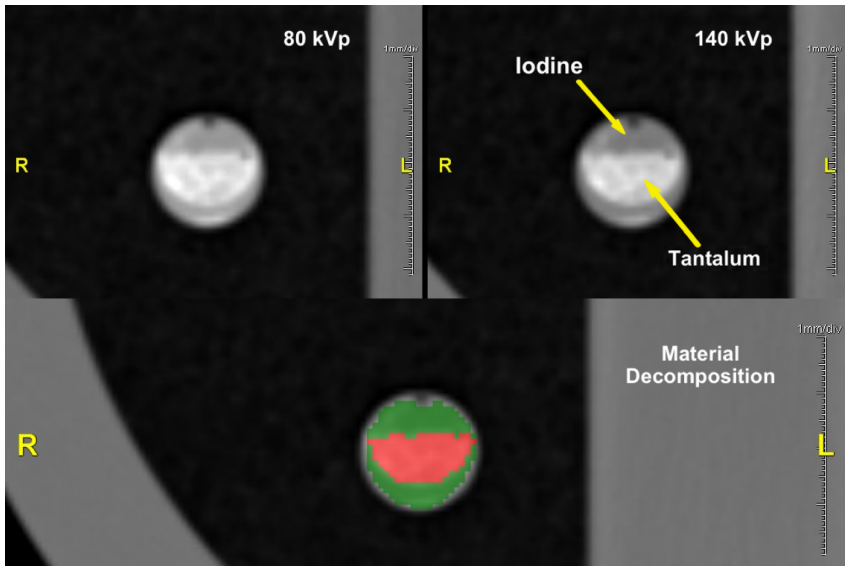

Figure 31 Detailed separation of iodine and tantalum
A syringe containing a semicylindrical cast of tantalum suspended in a gelatinous medium. The tantalum is surrounded by an iodine solution. The CT-number difference between these materials varies distinctly between high and low kVp levels. It is this individual variation with kVp that enables material decomposition. Copyright: The Authors.

Paper III

Following patient selection, one individual from the metastasis group was excluded after the lesions were reclassified as being located on the liver surface. Following this exclusion, 39 patients were enrolled in the study, comprising 19 with hypovascular liver metastases and 20 control patients without metastases. The metastasis group included 10 women and 9 men, with a mean age of 64.9 ± 13.2 years. The control group consisted of 11 women and 9 men, with a mean age of 63.3 ± 13.3 years. A median of 5 additional studies per patient, conducted over a median time span of 25 months, were reviewed to establish the reference standard.

The mean $CTDI_{vol}$ for the actual abdominal CT examinations, from which reduced radiation dose levels were simulated, was 11.5 ± 3.0 mGy with a DLP of 550 ± 172 mGy×cm. The resulting mean $CTDI_{vol}$ values for the simulated dose levels were as follows: DL75 = 8.6 mGy; DL50 = 5.8 mGy and DL25 = 2.9 mGy. The corresponding mean image noise levels were: DL100 = 13.2 ± 2.3 HU; DL75 = 15.4 ± 2.5 HU; DL50 = 17.7 ± 2.9 HU and DL25 = 23.3 ± 3.7 HU.

Figure 32 presents example images illustrating the image quality of the four different dose levels, highlighting the effect of increasing noise levels on the conspicuity of lesions of varying sizes.

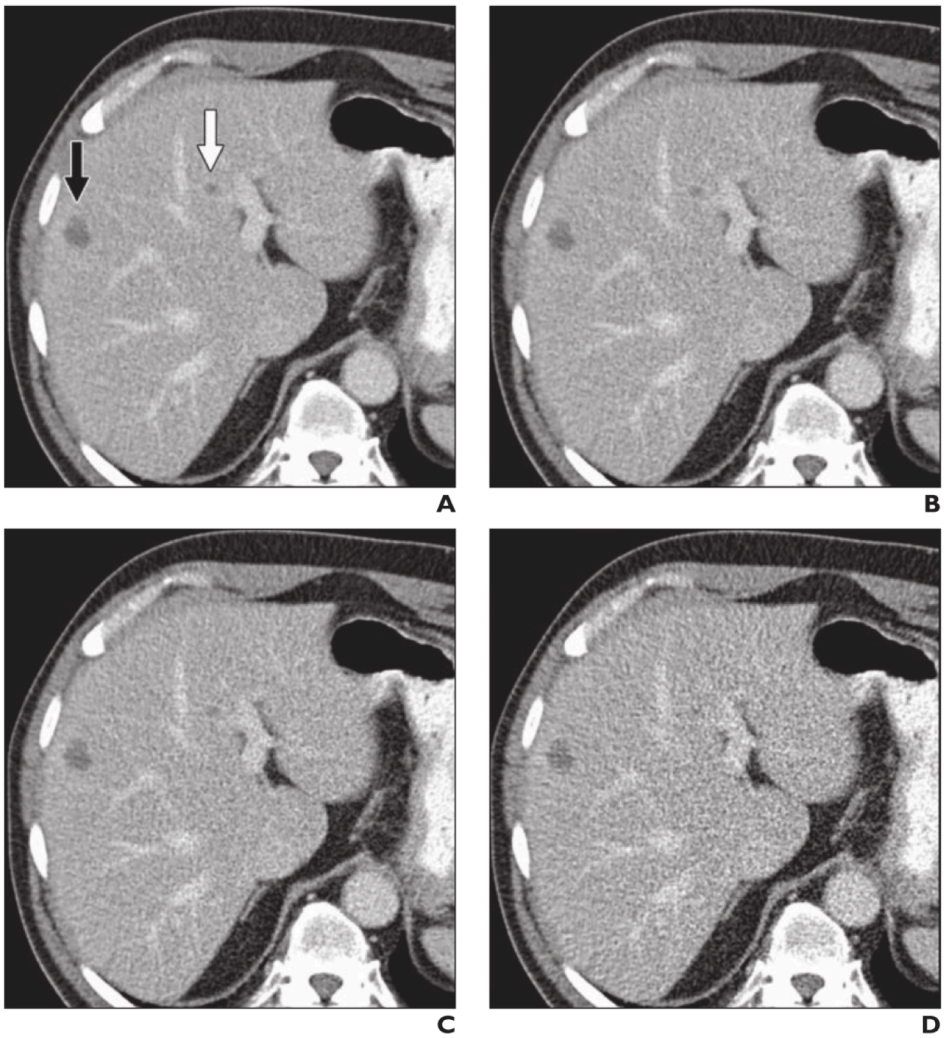

Figure 32 Image quality at different dose levels

Abdominal CT images of a patient with liver metastases. The four simulated radiation dose levels are presented: (A) DL100; (B) DL75; (C) DL50 and (D) DL25. Two metastases are present in the images. The larger metastasis (Black arrow) was detected by all five readers at all dose levels. The conspicuity of the small metastasis (white arrow) was negatively affected by increasing image noise, detected by four readers at the higher dose levels, but not detected by any reader at DL25. From Fält T, et al. Simulated Dose Reduction for Abdominal CT With Filtered Back Projection Technique: Effect on Liver Lesion Detection and Characterization. American Journal of Roentgenology. 2019 Jan;212(1):84–93. Reproduced with permission by American Roentgen Ray Society.

Mean detection rates of all five readers are presented in Table 5. Comparable detection rates exceeding 90% for metastases, as well as for all lesions combined, were observed for DL100 and DL75, whereas DL50 and DL25 exhibited lower detection rates.

Table 5 Detection rates of metastases and benign lesions for the different dose levels
P values from comparison to the reference group DL100 (χ^2)

Group	Metastases >5 mm (n=50)		Benign lesions >5 mm (n=12)		All lesions > 5 mm (n=62)	
	Detection rate (%), mean (range)	p-value	Detection rate (%), mean (range)	p-value	Detection rate (%), mean (range)	p-value
DL100	94 (88 – 100)	REF	87 (83 – 92)	REF	93 (87 – 97)	REF
DL75	92 (88 – 98)	0.39	83 (75 – 92)	0.61	90 (87 – 94)	0.32
DL50	84 (80 – 88)	*<0.01*	78 (67 – 83)	0.23	83 (81 – 87)	*<0.01*
DL25	74 (58 – 84)	*<0.01*	68 (58 – 75)	*0.016*	73 (60 – 82)	*<0.01*

DL: Dose Level

The FOMs from the JAFROC analysis, along with the differences in FOMs between the reduced dose levels and DL100, are detailed in Table 6. The results of the non-inferiority analysis are illustrated in Figure 33. The FOM for DL75 is nearly identical to that of DL100, and with the lower bound of the 95% confidence interval (CI) for the difference between these two FOMs exceeding -0.05, non-inferiority of DL75 is confirmed. In contrast, DL50 and DL25 were deemed inferior to DL100 in the JAFROC analysis, as the 95% CIs for their differences from DL100 extend substantially below the non-inferiority threshold

Table 6 Figures of merit (FOMs) of the JAFROC analysis
The FOM of each dose level and the difference in FOM between reference level DL100 and all other dose levels.

DL	FOM	95% CI	Difference in FOM compared with DL100	95% CI of Difference compared with DL100
100	0.962	0.928-0.997	Reference	Reference
75	0.961	0.927-0.994	-0.002	-0.049 to 0.046
50	0.922	0.865-0.978	-0.041	-0.088 to 0.006
25	0.874	0.797-0.952	-0.088	-0.135 to -0.041

DL: Dose Level, FOM: Figure of Merit, CI: Confidence Interval

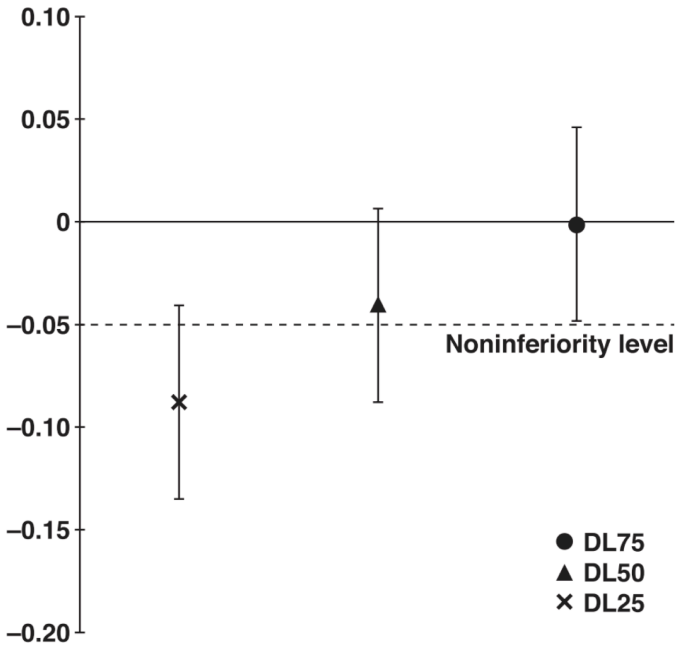

Figure 33 Results from JAFROC noninferiority analysis

The difference in figure of merit (FOM) between the reference dose level (DL100) and the other dose levels. The lower bound of the 95% CI of the difference between DL75 and DL100 does not include the noninferiority level -0.05, and DL75 is therefore considered noninferior to DL100. DL50 and DL25 do not fulfil noninferiority. From Fält T, et al. Simulated Dose Reduction for Abdominal CT With Filtered Back Projection Technique: Effect on Liver Lesion Detection and Characterization. American Journal of Roentgenology. 2019 Jan;212(1):84–93. Reproduced with permission by American Roentgen Ray Society.

Lesion characterisation was also evaluated by applying a cut-off on the Likert scale below grade 3 ("moderate probability of malignancy"), thereby dichotomising lesion ratings into correct and incorrect decisions. The proportions of metastases and benign lesions accurately rated are presented in Table 7, while the number of benign lesions and false positive localisations incorrectly graded as metastases are detailed in Table 8. Contrary to the non-inferiority of DL75 established in the JAFROC analysis, the number of benign lesions incorrectly classified as metastases was elevated at this dose level. When combining benign lesions and false positive markings graded as metastases, the total for DL75 was significantly higher than for DL100.

Table 7 Correctly graded lesions for the five readers using a cutoff level below grade 3 ("moderate probabilty of malignancy")

Lesions	DL100	DL75	DL50	DL25
Metastases graded 3-5	77 (62-88)	76 (60-88)	73 (68-78)	66 (58-80)
p	-	0.83	0.35	*<0.01*
Benign lesions graded 1-2	75 (67-83)	52 (17-75)	58 (25-83)	58 (50-67)
p	-	*<0.01*	*0.05*	*0.05*

All values presented as % mean (range). DL: Dose Level. All *p* values are from comparisons to the reference level DL100 (χ^2 test). *Italics* indicate statistical significance.

Table 8 Mean number of incorrectly graded benign lesions and false-positive localisations for the five readers

Lesions	DL100	DL75	DL50	DL25
Benign lesions graded 3-5	1.4 (0-3)	3.8 (1-8)	2.4 (0-5)	1.2 (1-2)
p	-	0.11	0.37	0.72
False-positive localisations, any grade	2.2 (0-5)	4.4 (1-11)	3.0 (1-8)	3.8 (1-9)
p	-	0.32	0.39	0.39
False-positive localisations graded 3-5	0.4 (0-1)	1.2 (0-2)	0.4 (0-2)	1.2 (1-2)
p	-	0.11	1.00	*0.04*
Non-metastasis localisations (benign lesions + false-positives) graded 3-5	1.8 (0-4)	5.0 (3-9)	2.8 (1-5)	2.4 (1-4)
p	-	*0.03*	0.34	0.49

All values presented as *n* mean (range). DL: Dose Level. All *p* values are from comparisons to the reference level DL100 (Student's *t* test). *Italics* indicate statistical significance.

Inter-reader agreement analysis, conducted using ICC, yielded a value of 0.86 (95% CI: 0.83–0.89), indicating "good reliability" according to the interpretation guidelines of Koo and Li (90).

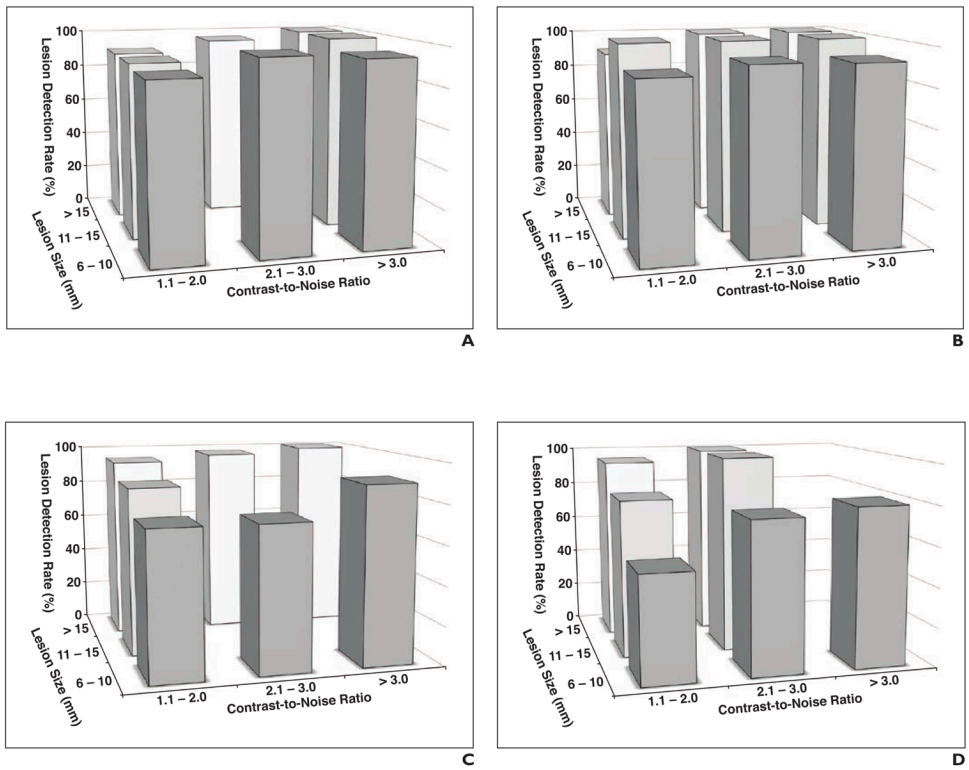

Figure 34 Detection of liver lesions stratified by size and contrast-to-noise ratio (CNR)

The mean percentage of detected liver lesions stratified by size and contrast-to-noise ratio (CNR) into nine subgroups and presented for the four dose levels: (A) DL100, (B) DL75, (C) DL50, and (D) DL25. Subgroups excluded from the graph contained fewer than four lesions (i.e., less than 20 potential reader localisations). At the lowest dose level (D), the detection rate for the smallest lesions with the lowest CNR is apparently reduced compared to similar lesions at higher dose levels. From Fält T, et al. Simulated Dose Reduction for Abdominal CT With Filtered Back Projection Technique: Effect on Liver Lesion Detection and Characterization. American Journal of Roentgenology. 2019 Jan;212(1):84–93. Reproduced with permission by American Roentgen Ray Society.

To evaluate whether the relationship between lesion size, CNR, and lesion detection remained consistent across varying dose levels, lesions were stratified into nine groups based on size and CNR. The proportion of correctly localised lesions within each subgroup was subsequently calculated. The results of this analysis examining the relationship between lesion size, CNR, and detection at different dose levels are presented in Figure 34. The number of lesions within each subset remains limited, rendering the findings tentative. Nevertheless, a clear trend emerges from the charts, indicating that the detection of small lesions with low CNR is adversely affected by the increasing noise levels at lower dose levels. This detrimental effect surpasses the reduction in CNR that correlates with the rising noise.

The $CTDI_{vol}$ of the low-dose phantom scans was 0.25 mGy and the high-dose scan for reference images had $CTDI_{vol}$ of 15.6 mGy.

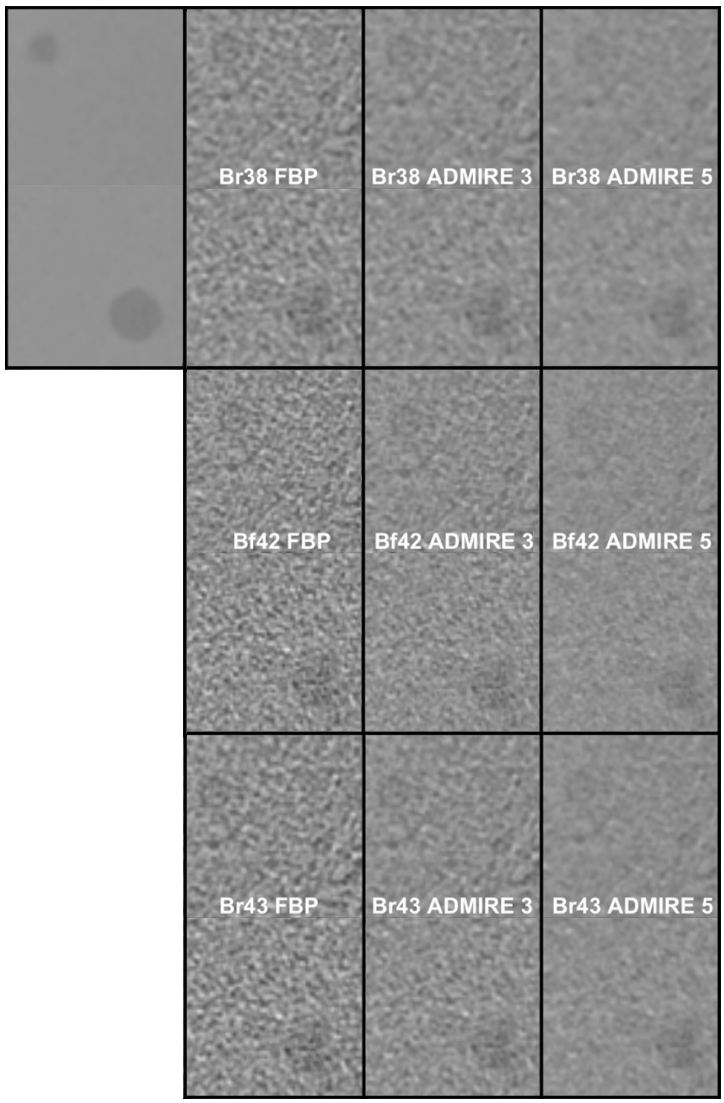

Figure 35 Images produced using the nine different reconstruction methods
Note the difference in noise magnitude as well as texture between the different reconstruction methods. One 8 mm and one 11 mm lesion are also included in the images to demonstrate the challenging detection task. Copyright: The Authors.

Image quality and noise texture of the nine reconstruction methods are illustrated in Figure 35. NPS of all reconstruction methods are presented in Figure 36 and qualitative descriptors of the NPS-curves detailed in Table 9. The higher-frequency noise with a finer texture in images reconstructed with Bf42 is evident in both the example images and the NPS

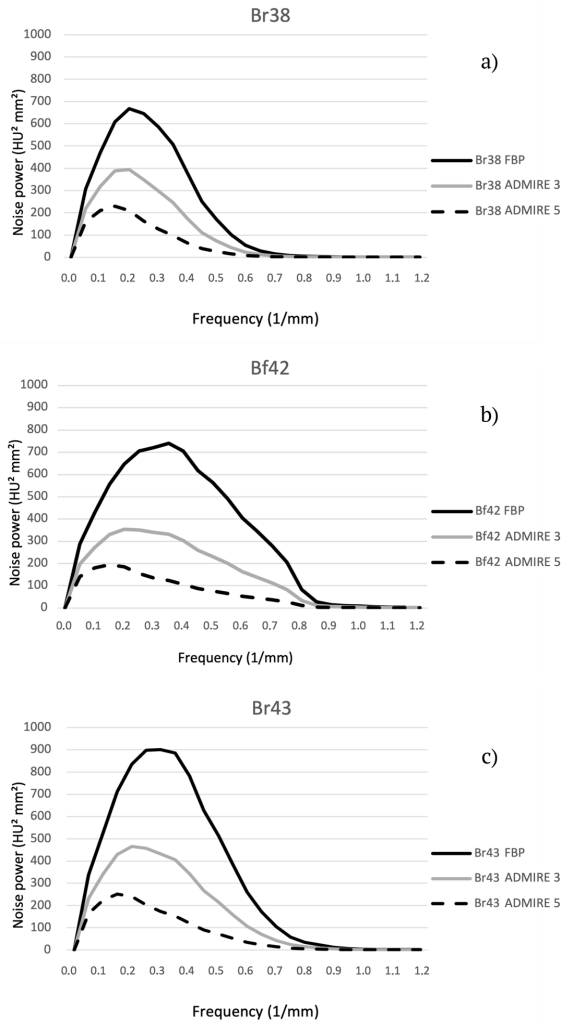

Figure 36 Noise power spectra (NPS) for all nine reconstruction methods
The NPS-curves are presented in a separate graph for each convolution kernel, all including filtered back projection (FBP) as well as ADMIRE strength 3 and 5. The NPS-curves of convolution kernel Bf42 have a different shape compared to the others, with a less steep slope at higher spatial frequencies corresponding to a sharper noise texture and higher spatial resolution. Copyright: The Authors.

Table 9. Quantitative descriptors of the NPS-curve for each reconstruction method

Reconstruction method	Peak Noise Power (HU^2mm^2)	Frequency of Peak Noise Power (mm^{-1})	AUC (HU^2 mm)	Frequency of 10% AUC (mm^{-1})	Frequency of 50% AUC (mm^{-1})	Frequency of 90% AUC (mm^{-1})
Br38 FBP	667	0.20	241	0.09	0.25	0.46
Br38 ADMIRE 3	394	0.20	133	0.08	0.23	0.44
Br38 ADMIRE 5	230	0.15	68	0.07	0.20	0.40
Bf42 FBP	741	0.35	393	0.13	0.37	0.66
Bf42 ADMIRE 3	355	0.20	183	0.11	0.33	0.64
Bf42 ADMIRE 5	195	0.15	82	0.08	0.26	0.60
Bf43 FBP	900	0.30	404	0.12	0.32	0.56
Bf43 ADMIRE 3	466	0.20	201	0.10	0.29	0.54
Bf43 ADMIRE 5	251	0.15	92	0.08	0.24	0.50

NPS: Noise-Power Spectrum, AUC: Area Under Curve

The JAFROC1 FOMs are displayed in Figure 37, with the differences in FOMs between all reconstruction methods and the reference Br38 FBP shown in Figure 38. In the latter figure, a 95% CI excluding "0" indicates a significant difference between the evaluated reconstruction method and the reference. The use of Bf42, whether combined with FBP or ADMIRE, resulted in significantly improved lesion detection when including 8 mm lesions and controls.

When dichotomising the Likert scale grades into detected or undetected lesions by applying a cut-off below grade 2 ("possibly a lesion"), the proportion of detected lesions was significantly higher with Bf42 FBP alone. This reconstruction method also yielded significantly fewer false positive markings rated above the cut-off compared to Br38 FBP (Tables 10 and 11)

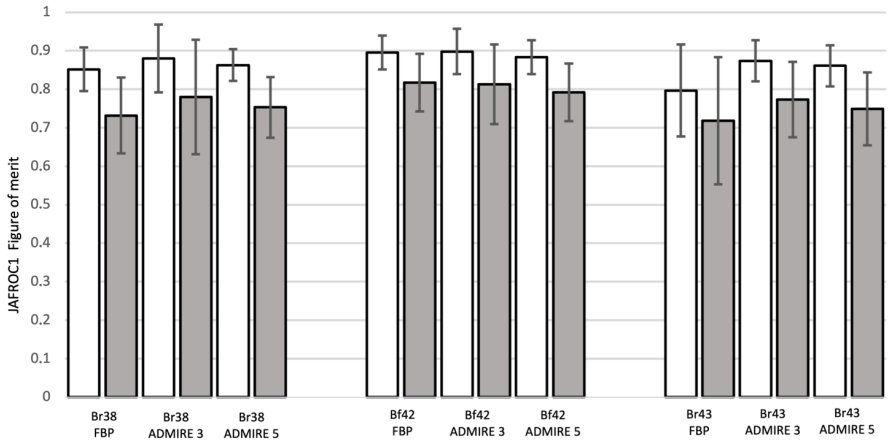

Figure 37 JAFROC1 figures of merit (FOMs) of all nine reconstruction methods
White columns represent JAFROC1 analysis of all image stacks (8 mm lesions, 11 mm lesions and controls) n=80. Grey columns represent analysis of 8 mm lesions and controls, n=60. Error bars represent the 95% confidence interval. Use of Bf42 leads to slightly higher figures of merit compared to the other kernels. Copyright: The Authors.

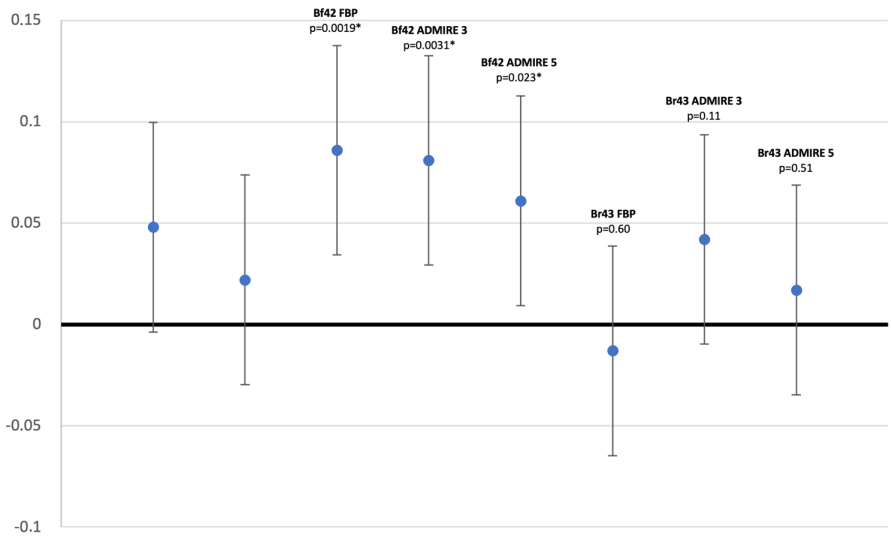

Figure 38 Difference in JAFROC1 figure of merit (FOM) compared to reference
Chart demonstrating the differences in FOM between Br38 FBP and the other eight reconstruction methods when including 8 mm lesions and controls. If the 95% confidence interval (error bars) does not include "0", the difference is significant. Bf42 has significantly higher FOMs combined with FBP as well as ADMIRE 3 and 5.

Table 10 True positive markings rated 2 - 4

Fractions of lesions detected 2 – 4 for all nine reconstruction methods. Comparison to the reference method Br38 FBP. Statistical analysis using McNemar's test. *Italics* denote significant difference.

Reconstruction Method	True Positive Markings rated 2 – 4; All lesions (n=50)	p-value, compared to Br38 FBP	True Positive Markings rated 2 – 4; 8 mm lesions (n=30)	p-value, compared to Br38 FBP	True Positive Markings rated 2 – 4; 11 mm lesions (n=20)
Br38 FBP	67%	Reference	45%	Reference	100%
Br38 ADMIRE 3	68%	0.76	47%	0.76	100%
Br38 ADMIRE 5	68%	0.75	47%	0.75	100%
Bf42 FBP	74%	*0.014*	57%	*0.014*	100%
Bf42 ADMIRE 3	72%	0.05	54%	0.05	100%
Bf42 ADMIRE 5	70%	0.38	49%	0.38	100%
Br43 FBP	66%	0.76	43%	0.76	100%
Br43 ADMIRE 3	70%	0.28	50%	0.28	100%
Br43 ADMIRE 5	66%	0.79	43%	0.79	100%

Table 11 Percentages of cases with false positive markings rated 2 - 4

Statistical analysis using McNemar's test. *Italics* denote significant difference.

Reconstruction method	Percentage of cases with false positive markings rated 2 – 4; All cases incl. controls	p-value, compared to Br38 FBP
Br38 FBP	7.7%	Reference
Br38 ADMIRE 3	5.0%	0.22
Br38 ADMIRE 5	7.0%	0.88
Bf42 FBP	2.3%	*0.0062*
Bf42 ADMIRE 3	5.0%	0.24
Bf42 ADMIRE 5	4.7%	0.15
Bf43 FBP	5.7%	0.40
Bf43 ADMIRE 3	3.3%	*0.037*
Bf43 ADMIRE 5	7.3%	0.40

Inter-reader agreement analysis, conducted using the ICC, demonstrated excellent reliability for all five readers (ICC = 0.95, 95% CI: 0.95–0.96). Intra-reader agreement, assessed for the 80 cases read twice, indicated "good reliability" for four readers and "excellent reliability" for one reader.

Discussion and Future Perspectives

This doctoral thesis approaches optimisation of abdominal CT examinations, and imaging of liver metastases in particular, in different ways.

The results of **Paper I** demonstrate equal CNR and SNR between groups of patients examined using an age-stratified protocol designed to reduce risks specific to patients of different ages – i.e. the risk from ionising radiation being more important when examining young patients and older patients being more at risk of kidney injury from contrast media. Since this protocol was designed, and the study evaluating it was carried out, important progress has been made in the research of risks from low doses of ionising radiation as well as the risk of contrast media induced kidney injury. Since these are the two risk categories the protocol in **Paper I** is meant to balance a review of recent research on both topics will follow:

Recent advances in knowledge: Cancer risk from low radiation doses

Following the groundbreaking study by Pearce et al. in 2012, subsequent research has continued to reinforce the epidemiological evidence linking increased cancer risk to ionising radiation exposure from CT examinations (56). These studies predominantly focus on paediatric head CT scans due to several key factors: 1) head CT is the most frequently performed CT examination in children; 2) the brain exhibits heightened radiosensitivity in children; and 3) children possess a greater proportion of active red bone marrow in the skull compared to adults (92,93).

Insights from National Cohort Studies

A large Australian cohort study, including both individuals exposed and unexposed to CT examinations during childhood, has demonstrated an elevated risk of multiple cancer types (92,94,95). The latest analysis of this cohort identified an increased risk of brain tumours, with an ERR per 100 mGy of 0.8, translating to one additional brain tumour case per 6,391 children undergoing a CT examination (94).

Taiwan's national health database is extensive which makes it particularly suitable for retrospective cohort studies. A 2014 study conducted in Taiwan demonstrated an increased risk of brain tumours (benign and malignant combined) following paediatric head CT scans (Hazard Ratio [HR]: 2.56), but no significantly increased risk of

leukaemia (96) The findings were confirmed in a subsequent study published in 2020, which reported a significantly increased risk of malignant brain tumours (Odds Ratio [OR]: 1.55) (97).

Several national cohort studies have also been conducted in Europe. In a Dutch cohort, a significantly increased risk of malignant brain tumours was identified following paediatric CT examinations (98). Similarly, the latest analysis from a French cohort revealed a significantly increased risk of brain tumours and leukaemia. In contrast, a German cohort study found no statistically significant associations between paediatric CT exposure and cancer risk (99,100).

These national cohorts, combined with data from a total of nine European countries, form a large cohort within the European EPI-CT study. In 2023, analyses were published based on this combined cohort, which included nearly one million individuals who underwent CT examinations before the age of 22. The mean cumulative brain radiation dose was 47 mGy, median age at first examination was 10.7 years, with a median follow-up period of 7.8 years (101). Representing the largest cohort study to date on patients exposed to CT radiation, it reported significant associations for brain tumours, with an ERR per 100 mGy of 1.27, and for haematological malignancies, with an ERR per 100 mGy of 1.96. This equals 1 additional case of brain cancer and 1-2 additional cases of haematological malignancies in 10,000 patients and a follow-up of 10 years (102,103).

Meta-Analyses of Low-Dose Radiation Risks

Lastly, recent meta-analyses have pooled data from various studies exploring cancer risk associated with radiation doses below 100 mGy. In 2017, Lubin et al. conducted a meta-analysis focusing on the risk of thyroid cancer following childhood thyroid irradiation. The included studies analysed different types of medical, non-diagnostic radiation exposure, as well as data from the LSS cohort. For radiation doses to the thyroid gland below 100 mGy a significantly increased risk was observed, with a Relative Risk (RR) of 2.9. The estimated number of excess cases of thyroid cancer was very small, though, at about 10 cases per 10,000 individuals followed for 45 years (104).

Another meta-analysis by Hauptmann et al. (2020), encompassing studies published between 2006 and 2017 that investigated cancer risk following radiation exposure at doses below 100 mGy, reported elevated risks for leukaemia in children (ERR per 100 mGy = 2.84). For adults, the analysis demonstrated increased risks for both leukaemia (ERR per 100 mGy = 0.16) and solid cancers (ERR per 100 mGy = 0.03). This finding is significant, as it highlights a detectable cancer risk associated with exposure to low radiation doses in adulthood, albeit notably lower than that observed following exposure during childhood (105)

In 2021, Berrington de Gonzalez et al. compiled the relevant studies on the risk of leukaemia and brain cancer following CT examinations, primarily in children and young individuals, totalling 17 studies. A meta-analysis of the studies with appropriate data reported an ERR per 100 mGy of 1.78 for leukaemia (statistically significant, based on 5 studies) and 0.79 for brain tumours (statistically significant, based on 4 studies). This finding is particularly important as it specifically examines the cancer risk associated with radiation from CT examination (106).

Conclusions and remaining uncertainties

This review of the literature shows that cancer risks associated with CT examinations have become increasingly well-documented in recent years. However, uncertainties remain regarding the relationship between low-dose radiation exposure and cancer risk. The demonstrated risk associated with a single CT examination is very small over the relatively short follow-up periods in most studies. From the LSS it is known that, unlike leukaemia, solid cancers typically manifest many years after radiation exposure. Therefore, the risk of solid cancers may be underestimated in current cohort studies due to insufficient follow-up durations (107).

While cancer risk is higher following radiation exposure during childhood, a slightly elevated risk has also been observed in adults (105). As adult patients typically undergo more frequent CT examinations, often at higher radiation doses per examination, they can be exposed to a substantial cumulative radiation dose, potentially exacerbating the risk from radiation (108)

Another noteworthy consideration is the biological impact of the low-energy, low-Linear Energy Transfer X-ray radiation used in CT scans. Evidence suggests that this type of radiation may have a relatively higher biological effect compared to higher-energy gamma radiation, to which atomic bomb survivors in Japan were exposed and that is used in radiotherapy. This difference is expressed through variations in the Relative Biological Effectiveness (RBE) (109,110).

The reason behind this increased biological effectiveness lies in the low-energy secondary electrons produced following the primary interaction between photons and atoms in the cells. The low-energy secondary electrons are more likely to interact with atoms nearby, increasing the probability of double-strand breaks (DSBs) in DNA at comparable absorbed radiation doses. This has been demonstrated through both Monte Carlo simulations and radiobiological experiments and DSBs are directly associated with cancer induction (111,112).

As a result, radiation energy levels associated with X-ray in CT examinations may theoretically carry a higher cancer risk per unit dose compared to radiation exposure from atomic bomb detonations, from which much of the risk data previously has been derived. However, the DDREF (assuming a value of 2) has an effect in the opposite

direction, reducing the risk at the doses used in CT examinations. Consequently, there are several factors complicating the estimation of cancer risks associated with CT imaging and further epidemiological studies with longer follow up times are needed to yield objective data.

In conclusion, the association between radiation exposure from, or with magnitude equal to, CT examinations and an increased cancer risk can now be considered well-established. However, uncertainties remain, particularly concerning the cancer risk for patients examined in adulthood and whether the risk of solid cancer types increases with extended follow-up periods.

While the absolute risk associated with a single CT examination is very small, even a minimal risk becomes significant at the population level when a sufficiently large number of patients is exposed. The number of CT examinations is substantial and continues to grow, now contributing significantly to the overall population-level radiation exposure (113,114). In a recent publication, Smith-Bindman et al. estimated the number of CT examinations performed in the United States in 2023 and projected the associated lifetime cancer incidence. A total of 93,000,000 CT examinations were conducted in 61,510,000 patients. Using the National Research Council's Biological Effects of Ionizing Radiation VII (BEIR VII) models, the authors approximated that these examinations could induce approximately 103,000 cancers. Notably, although the risk per examination is highest for younger patients, the largest number of projected cancers occurred in individuals aged 40–59 years at the time of examination. This is attributable to the high number of scans performed in this age group, combined with their relatively long remaining lifespan. The CT examination type associated with the greatest number of induced cancers in adults was abdomen and pelvis, with an estimated 37,000 cases. These figures exceed expectations based on earlier International Commission on Radiological Protection (ICRP) estimates. Projections of future risks should be interpreted with caution; nevertheless, they underscore the critical need for ongoing optimisation of CT examinations, adhering to the "As Low As Reasonably Achievable" (ALARA) principle for radiation dosing. Equally imperative is the rigorous implementation of justification assessments for each CT examination. While it is essential to remain mindful of the risks, for most individual patients, a comprehensive justification assessment typically indicates that the diagnostic benefits outweigh the associated radiation risks.(115)

Contrast Media Induced Kidney Injury – Updated view

When reviewing the literature on this subject, spanning several decades, an intriguing paradox is revealed: despite the large number of studies exploring many different hypotheses, the most fundamental question remains unresolved - does LOCM administration truly increase the risk of kidney injury, and if so, to what extent? This

knowledge gap arises from the paucity of randomized controlled trials. Even more concerning is that many otherwise well-designed studies - examining, for example, differences in nephrotoxicity between contrast agents or the efficacy of prophylactic strategies - have lacked a control group unexposed to contrast media.

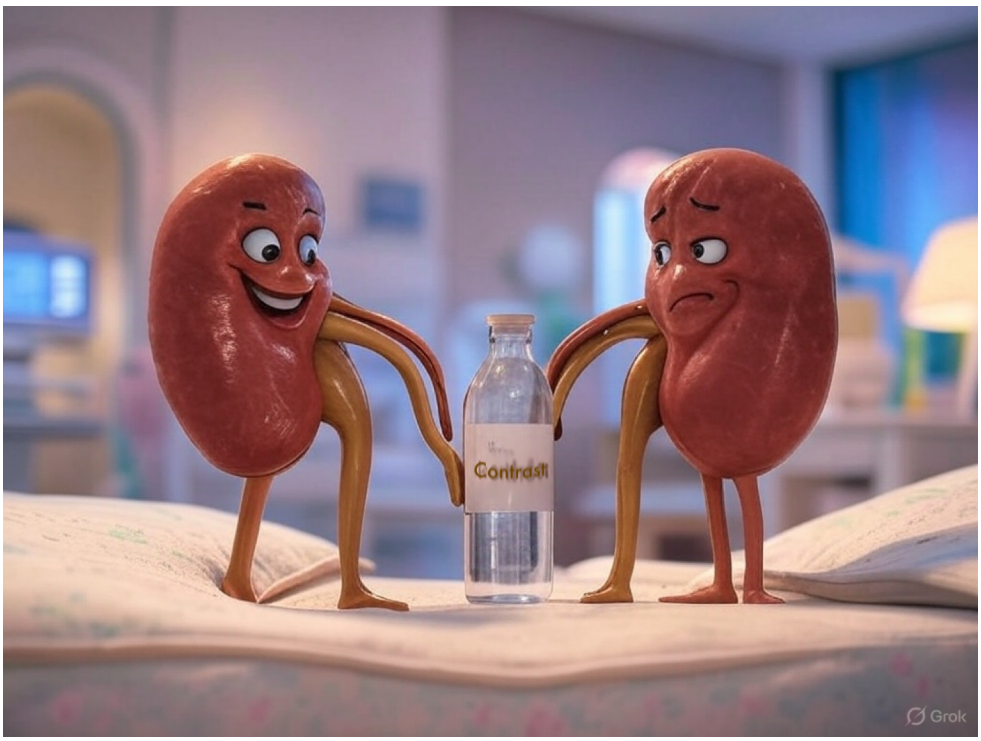

Figure 39 Happy kidney, sad kidney
AI generated image illustrating the polarized views on the risk of kidney injury after intravenously used iodinated low osmolar contrast media. Image generated by Grok after prompt by the Author.

How, then, did this situation develop?

As mentioned in the introduction, in the early days of iodinated contrast media, a general consensus formed that contrast medium exposure carried a risk of subsequent kidney injury, especially in patients with pre-existing reduced kidney function. Rather than seeking to validate this central hypothesis, the research community moved on toward exploring strategies to mitigate this presumed risk and identifying the most significant risk factors.

Another reason for the lack of control groups is that a large part of the research on kidney injury after LOCM administration has focused on cardiac procedures, such as percutaneous coronary interventions (PCI). These procedures are known to carry a risk

of acute kidney injury (AKI) while also being nearly indispensable in certain clinical scenarios involving acute coronary syndromes. Consequently, recruiting a control group of comparable patients who have not been exposed to contrast media presents a significant challenge. Acute cardiac conditions also increase the risk of haemodynamic instability, a known risk factor for AKI.

The consensus that LOCM poses a significant risk for kidney injury in patients with impaired renal function has strongly influenced radiological practice, often resulting in patients with chronic kidney disease (CKD) undergoing imaging without intravenous contrast. This approach has led to a strong selection bias being present in retrospective clinical data, as patients with reduced renal function are disproportionately more often chosen for non-contrast CT scans. This imbalance presents a substantial challenge when designing retrospective observational studies to address existing knowledge gaps.

Considering these challenges, how can this issue be effectively addressed? Conducting randomized controlled trials (RCTs) is challenging for several reasons, primarily ethical concerns, as it would require randomizing some patients to suboptimal imaging, potentially leading to negative health outcomes. Additionally, given that any potential increase in kidney injury risk from contrast media is likely small, an RCT would need to have a large number of participants to detect a statistically significant difference.

Retrospective observational studies circumvent these ethical dilemmas but must contend with the selection bias in the unbalanced clinical data described above.

A promising solution is propensity score matching (PSM), a statistical technique that has gained popularity in recent years. PSM involves retrospectively identifying patients from clinical databases and calculating a propensity score for each individual - representing the likelihood of receiving the treatment under investigation, in this case, contrast-enhanced CT. This score is derived from known confounding variables that influence treatment selection. In this context sex, age and known risk factors for contrast induced kidney injury are considered confounding variables. Once calculated—typically in a large patient cohort—patients who underwent the treatment are matched, often pairwise, with unexposed control patients with corresponding propensity scores. This method effectively creates a well-balanced control group, mimicking the conditions of a randomized study and improving the validity of retrospective analyses (116–118).

Despite their methodological strengths, PSM studies also have notable limitations. A common critique is that PSM can only incorporate known and measurable confounders into calculations, whereas randomization distributes both known and unknown confounders equally between study groups. This limitation may introduce residual confounding from unmeasured variables, potentially biasing analytical outcomes. Additionally, the matching process inherently reduces sample size, which can compromise statistical power (116–119). Furthermore, confounders are typically

dichotomised in propensity score calculations as either present or absent, resulting in diminished granularity that may oversimplify complex relationships (120).

Even considering these limitations, well-executed PSM studies likely constitute the most robust evidence currently available for assessing AKI risk following intravenous LOCM administration. The subsequent section critically examines selected high-quality PSM studies and relevant meta-analyses addressing this clinical question.

The earliest PSM studies on this subject were conducted in 2013 by Davenport et al. and McDonald R. et al. Both investigations stratified patients' kidney function using serum creatinine (SCr) levels rather than eGFR and employed an older, slightly different definition of AKI, making their results difficult to compare with more recent studies. Neither of these large studies demonstrated an increased risk of AKI following LOCM administration throughout their entire study populations. However, the findings diverged regarding subgroups with severely impaired renal function: Davenport et al. observed a significantly elevated incidence of AKI, while McDonald R. et al. found no difference between contrast-exposed and unexposed patients (121,122).

McDonald R. et al. conducted a noteworthy sub-analysis including 4,265 patients who had undergone computed tomography (CT) both with and without LOCM during the study period. These patients effectively served as their own controls, and no increased incidence of AKI was observed following the contrast-enhanced examinations (122).

The largest study to date was published in 2024 by Choi et al., comprising 182,170 matched pairs of patients in South Korea undergoing CT with or without LOCM. This investigation did not demonstrate a significantly increased risk of AKI following LOCM administration when analysing the entire study population. The AKI incidence was 4.1% in the contrast group versus 3.9% in the non-contrast group, with an odds ratio (OR) of 1.036 (95% confidence interval [CI]: 0.968-1.109). Similarly, the risk of dialysis initiation within one month was not elevated, with an incidence of 0.4% in both groups.

However, subgroup analysis revealed statistically significant differences in patients with impaired renal function. Among patients with eGFR 30 - 45 (12,208 matched pairs) and eGFR <30 (6,786 matched pairs), a modest but statistically significant increase in AKI incidence was observed following LOCM exposure. For patients with eGFR 30 - 45, the absolute risk increase was 1.5 percentage points (11.5% vs. 10.0%), while for eGFR < 30, the difference was 2.9 percentage points (19.4% vs. 16.5%).

Unfortunately, the investigators did not conduct subgroup analyses for dialysis risk in these populations with reduced renal function (123).

Among seven additional, large propensity score matching studies stratifying patients according to eGFR and comprising between approximately 5,000 and 41,000 matched

pairs, the majority found no increased risk of AKI following LOCM exposure when analysing entire study populations (124–130). Only one study, by Su et al., demonstrated a significantly higher AKI incidence after LOCM administration, with an absolute risk increase of 2.7 percentage points (10.9% versus 8.2%). Collectively, these studies suggest that there is no elevated risk of AKI after LOCM exposure across the general population undergoing computed tomography (CT) examinations. Furthermore, none of these investigations demonstrated an increased risk of dialysis initiation for the entire population, with most studies employing a 30-day follow-up period.

However, subgroup analyses of patients with severely reduced renal function (eGFR < 30) yielded contrasting results. Consistent with the findings of Choi et al., four of the seven studies identified significantly increased AKI risk in patients exposed to intravenously administered LOCM, with absolute risk increases ranging from 3.1 to 7.9 percentage points (124,127,129,130). Similar results were reported by Harrison et al. in a study specifically investigating patients with eGFR < 30, which found an increased AKI risk with an odds ratio of 1.49 (95% confidence interval: 1.06-2.10). (131)

These findings are important, likely confirming a small, but real risk of AKI following intravenous LOCM administration in patients with eGFR < 30. This risk warrants consideration in clinical practice and should be incorporated into risk-benefit analyses when planning CT examinations for these patients.

Although an increased incidence of AKI is observed in patients with eGFR < 30, the impact on long-term renal function, specifically the risk of dialysis initiation, remains less certain. Throughout the five studies examining this outcome in the eGFR < 30 subgroup, four reported no significant difference, while only one study, Gorelik et al, demonstrated a modest absolute risk increase of 4.9 percentage points (10.9% vs. 6.0%) (124,126,129–131). Overall, the risk of persistent renal impairment requiring dialysis following LOCM-enhanced CT appears to be either minimal or non-existent, even in patients with eGFR <30.

Regarding chronic kidney disease (CKD) category 3, subgroup stratification varied between studies. Some analysed patients with eGFR 30-60 as a single group, while others designated eGFR 30-45 as a separate subgroup. This methodological heterogeneity complicates direct comparison, but studies were approximately evenly divided between those showing an absolute risk increase of a few percentage points and those demonstrating no intergroup difference (123–127,129,130,132).

The findings from the PSM studies reviewed above align with two meta-analyses conducted in 2018 (Aycock et al) and 2022 (Obed et al). These meta-analyses similarly found no evidence of an elevated risk to the general population. However, Obed et al. reported a small but statistically significant increase in risk at eGFR < 30 (4 percentage

points, 19% vs 15%). Neither meta-analysis identified an increased requirement for dialysis following low-osmolar contrast media (LOCM) exposure (133,134).

Lastly, several smaller PSM studies have investigated the risk of acute kidney injury (AKI) and the need for dialysis following LOCM-enhanced CT in patient cohorts with specific risk factors. These include patients in intensive care units, patients with sepsis, patients with preexisting AKI, those already in dialysis, and individuals with cancer. None of these studies demonstrated an increased incidence of AKI or a delayed recovery of preexisting renal impairment following LOCM administration. These results suggest that contrast-enhanced imaging, which is often critical for these patient populations, can be performed without elevating the risk of AKI (135–138).

With a modestly increased risk of AKI in patients with pre-existing severely decreased kidney function exposed to LOCM now established, the question of whether this risk correlates with the dose of CM requires investigation. Well-designed studies analysing this relationship for intravenous LOCM administration in CT examinations are lacking. However, the association between contrast media dose and AKI risk is well-documented in patients undergoing PCI. Using data mainly from this type of examinations the dose-risk relationship has been quantified, with an increased risk of AKI observed when the LOCM dose, expressed in grams of iodine, numerically exceeds the patient's absolute eGFR. This elegantly defined relationship has for many years been used in guidelines published by the Contrast Media Committee of the Swedish Society of Urogenital Radiology.

The applicability of this dose-risk relationship to intravenous LOCM use in CT remains unclear, though. The uncertainty stems from the difficulty in isolating the contribution of CM to AKI following coronary interventions. Other procedural factors, such as catheterization-induced microembolism and more importantly, haemodynamic instability inherent to the clinical setting, confound the association (139).

In the absence of definitive data, a dose-risk relationship for intravenous LOCM in CT remains speculative. However, given the established nephrotoxic potential of LOCM and the observed association between exposure and increased AKI risk in patients with renal impairment, it is plausible to hypothesize a dose-dependent relationship, with higher doses correlating with greater AKI risk, especially in patients with eGFR < 30.

Balancing risks from ionising radiation and contrast medium

Over the past decade, research has established that the risks of cancer induction from ionising radiation during computed tomography (CT) examinations, as well as contrast media-induced kidney injury in patients with severely impaired renal function, are real, albeit lower than previously estimated. This evolving understanding emphasises the necessity of tailoring abdominal CT examination protocols to individual patient risk

profiles. In **Paper I**, the subjective assessment of image quality in the youngest age group, examined at the lowest radiation dose, was found to be inferior compared to other groups. This may be attributable to methodological limitations, as the evaluation focused on the "visually sharp reproduction" of anatomical structures rather than pathological lesions. While this is a standard approach in VGC studies, it may not fully reflect the benefits of increased contrast enhancement for detecting hypovascular liver lesions. Conversely, the absence of significant differences in SNR between the age groups, including the youngest, indicates clinically acceptable image quality throughout. The consistent CNR, calculated based on the contrast between the liver and a hypothetical metastasis, supports this finding, though its reliance on simulated data requires cautious interpretation.

Although the radiation dose from a single CT scan poses a minimal risk, even for young individuals, as noted previously, uncertainties persist regarding the long-term risk of solid cancers from low-dose ionising radiation. This underscores the importance of using the lowest reasonably achievable radiation dose when imaging young patients.

Two subsequent studies have investigated similar age- and risk-stratified protocols aimed at balancing radiation dose and contrast medium dose. Camera et al. (2015) prospectively evaluated a comparable protocol involving three age groups. Although their approach involved substantially higher radiation doses, they achieved similar outcomes, with notably consistent SNR in the liver and uniform subjective image quality in all age groups (140). However, CNR varied between groups, likely due to the calculation method, which relied on the difference in CT-numbers between the liver and subcutaneous fat.

More recently, Martens et al. (2024) investigated a modernised approach to this concept using an animal model with pigs and a CT scanner equipped with automatic tube voltage selection (ATVS). By adjusting ATVS settings, the scanner can prioritise either image noise reduction or enhanced iodine attenuation (accepting a higher noise level). Through matching the low-noise setting with a reduced CM dose and vice versa, they developed a stratified protocol that maintained consistent objective and subjective image quality (141). Collectively, the findings from **Paper I**, alongside those of Camera and Martens, demonstrate that CM and radiation doses can be balanced when individualising CT examinations for specific risk reduction, while preserving equivalent image quality. The most significant implication of this evidence is the potential to harness increased CM information—via higher CM doses or low-kVp scanning—to reduce radiation exposure, particularly in younger patients. At Skåne University Hospital, this principle is reflected in a dedicated abdominal CT protocol for patients under the age of 40 years without suspected malignancy, mirroring the second-youngest group in **Paper I**. This protocol, implemented in clinical practice, achieves a 30% reduction in radiation dose by increasing the CM dose by 20%.

Paper II of this thesis conducted an experimental investigation into the X-ray attenuation properties of high-Z elements and their potential for separation from iodine using MD. The findings indicate that Ta, W and Au exhibit X-ray properties rendering them ideal candidates for CM to be used alongside iodine. These elements were found to have DE ratios (CT-number at low energy divided by CT-number at high energy) around 1, contrasting with iodine's DE ratios of 1.9 -2.6, depending on the DE settings. In image-based MD, iodine and these elements were effectively separated with MD data colour-coded and overlaid onto standard axial images. Ga and Bi, with DE ratios ranging from 1.4 to 1.9, were less distinctly separated from iodine. Nearly complete separation from iodine was achieved for Bi, while separation of Gd was less effective. The outcome for Gd was anticipated, given its K-edge at 50.2 keV, being most proximate to iodine's 33.2 keV. The incomplete separation of Bi, despite its higher Z and K-edge at 90.5 keV, was more unexpected; its high DE ratio of 1.4–1.7 is caused by the entire low-energy X-ray spectrum lying below the K-edge, where attenuation again increases toward the L-edge at around 16 keV (17).

The interest in high-Z elements as potential CM in CT has surged in the last years, driven by technical developments in CT, particularly the introduction of PCDT CT.

Although the specifics of multi-material decomposition using PCDT fall outside the scope of this thesis, it warrants mention as an emerging technology. As previously noted, PCDT segments the energy spectrum of the detected photons into multiple energy bins, generating multiple datasets. The distinct attenuation profiles of elements with varying K-edge energies between these bins enable the decomposition of a greater number of materials. Energy bins can also strategically be positioned on either side of the K-edge of high-Z materials enabling precise identification of these elements, a procedure called K-edge imaging (28,29,142).

Recent investigations have evaluated experimental CM, either as nanoparticles or chelate formulations, incorporating elements such as Gd, Au, W, Ta, Bi, ytterbium (Yb) and hafnium (Hf) (75,79,82,143–147). Although no high-Z element-based CM are currently available for clinical use, advanced developmental stages have been reported for Bi- and Hf-containing chelates (79,147). Ta-based nanoparticles exhibited superior hepatic enhancement compared to LOCM in an animal model, improving liver-to-tumour CNR (148). An experimental W-based CM improved the separation of CM from calcified plaque in phantom models of coronary and carotid arteries. Utilising higher keV data reduced the "blooming" effect of calcium within plaques, enhancing discrimination, while simultaneously optimising the attenuation of the W-based CM, both factors improving MD of calcium and CM (75,149). Ta has long been employed as the radiopaque material in liquid embolic agents for intracranial vascular embolisation, necessitating high concentrations for fluoroscopic visibility during

interventions. This, however, introduces significant beam-hardening artefacts in subsequent CT examinations and complicates the differentiation of iodinated CM from the embolic material in CT angiography. PCDT addresses these challenges, with high-energy bin data reducing artefacts and MD effectively separating iodine from tantalum (150).

Beyond MD, high-Z CM hold potential for broader optimisation of abdominal CT, particularly in reducing radiation dose. High-Z elements offer greater radiation dose efficiency than iodine, providing enhanced attenuation and improved CNR at higher keV levels. This advantage stems from their ability to attenuate higher-energy photons that might otherwise pass through the patient and reach the detector. In contrast, iodine primarily attenuates lower-energy photons, which are more likely to interact with patient tissues and thus less likely to contribute to the detected signal. To maximise the information from low-keV photons, the photon quantity must be increased. This is achieved by increasing the mAs, which consequently raises the radiation dose. This limitation of iodine is particularly pronounced in obese patients, where high-Z CM may facilitate dose reduction

Sequential administration of distinct contrast agents, depicted in separate "phases" within a single scan using MD, can further minimise radiation exposure by obviating the need for multiple acquisitions (75,82). An example of such phase-separated contrast agents in an animal model is illustrated in Figure 40 (151).

Consequently, the findings from **Paper II**, corroborated by subsequent research, underscore multiple potential benefits of high-Z CM in CT. Ongoing intensive research aims to expedite their clinical adoption.

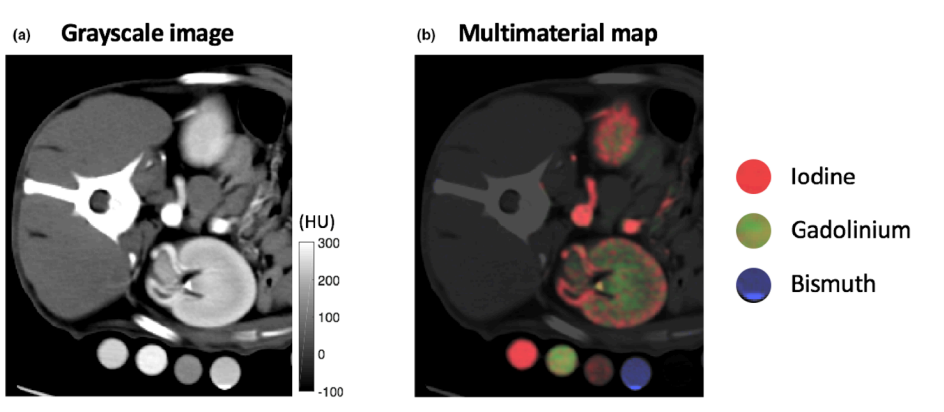

Figure 40 Multimaterial decomposition using photon-counting detector technology CT
In an animal model, Symons et al. performed material decomposition of iodine, gadolinium, and bismuth. Iodine and gadolinium are in "different contrast phases". Used with permission of John Wiley & Sons – Books. From: Symons R, et al. Photon-counting CT for simultaneous imaging of multiple contrast agents in the abdomen: An in vivo study. Medical Physics. 2017 Oct 1;44(10):5120–7.

Papers III and **IV** address, through distinct approaches, the detection of hypovascular liver lesions via CT, either in patients, at different simulated radiation dose levels, or in a phantom model evaluating the effect of different methods of image reconstruction.

In **Paper III**, JAFROC analysis demonstrated non-inferior detection and characterisation of metastases at a modest 25% radiation dose reduction. However, further reductions (50% and 75%) resulted in diminished diagnostic performance. Notably, the characterisation of benign lesions was adversely affected, with an increase in false positive localisations graded as having "moderate probability for malignancy" or higher, already at the 25% dose reduction. These findings are significant, as the ability to exclude disease is as critical as its detection, necessitating diagnostic methods with high specificity alongside sensitivity (152). Furthermore, as there were only 12 benign lesions in the 39 patients all analysis of this type of lesions must be treated with caution. As previously described, an examination protocol with 30% reduced radiation dose is used when examining patients under the age of 40 years at Skåne University Hospital. According to these results, this protocol could potentially lead to a degraded characterisation of benign lesions, leading to false positive findings and unnecessary follow-up examinations. However, as demonstrated in **Paper I**, the protocol also includes an increased CM dose, improving CNR and likely the evaluation of liver lesions. Additionally, the prevalence of benign liver lesions is low in younger patients; a large retrospective study of 45,000 patients undergoing liver ultrasound found benign lesions in 5% of those under 40 years, compared to 18% in those over 40 (153).

A sub-analysis in **Paper III**, stratifying lesions by size and CNR relative to surrounding parenchyma, revealed a noteworthy trend. At the lowest simulated radiation dose, detection of lesions with diameters of 6–10 mm and CNR of 1.1 – 2.0 was apparently reduced compared to higher dose levels (Figure 34). This suggests that elevated noise levels may impair the conspicuity of small lesions beyond the decline in CNR. The convolution kernel employed, B30f, is a soft kernel generating low-frequency noise, which may influence these outcomes.

In **Paper IV**, the influence of noise on the detection of small lesions was further explored. The phantom study, employing JAFROC1 analysis, revealed that a sharper convolution kernel (Bf42) significantly enhanced the detection of small, low-contrast lesions when images were reconstructed with FBP. IR (ADMIRE strength 3) combined with the standard kernel, improved detection to a lesser extent, achieving only borderline significance. Adding IR to images reconstructed with the sharp kernel did not further enhance lesion detection. Notably, the Bf42 kernel also reduced the number of false positive localisations. This kernel exhibited a distinct NPS profile, characterised by a less steep slope at higher frequencies, indicating a greater proportion of high-frequency noise. This was further evidenced by elevated frequency values at the 50^{th} and 90^{th} percentiles of the NPS. Although modulation transfer function (MTF) was not assessed in this study, prior research has demonstrated that sharper kernels improve

spatial resolution in CT images (154–157). This combination of increased high-frequency noise and enhanced spatial resolution is likely the mechanism underlying the improved detection of small, low-contrast lesions, achieved by subtly accentuating lesion edge reproduction.

Lesion detection in images reconstructed with ADMIRE strength 5 was inferior to that with ADMIRE 3 for all three kernels, despite a substantially lower noise magnitude. This discrepancy may be attributed to the prevalence of lower-frequency noise, coupled with a slightly higher CT-number within lesions in ADMIRE 5-reconstructed images, resulting in reduced lesion contrast. A plausible explanation for this elevated CT-number is the denoising and smoothing occurring during the regularisation step of the iterative process, which is intended to preserve edges. However, this process may degrade the edges of small, low-contrast lesions through smoothing rather than preservation (25). Supporting this hypothesis, reduced low-contrast spatial resolution compared to FBP has been observed with ADMIRE and other IR algorithms, including the latest generation of deep learning methods (158–161). Sugisawa et al investigated a way to mitigate this degradation of low-contrast spatial resolution from IR, by combining its use with sharper convolution kernels, and found spatial resolution and NPS comparable to FBP for some combinations of IR and sharp kernel (155). This aligns with the approach in **Paper IV**, where ADMIRE 3 paired with the sharper Bf42 kernel likely improved spatial resolution compared to ADMIRE 3 with a softer kernel.

An interesting finding in **Paper IV** is the marked discrepancy between lesion detection and CNR. The most effective reconstruction method was that in which lesions exhibited the lowest CNR relative to the background. This observation aligns with findings in **Papers I** and **III**, where discrepancies between CNR and reader-based metrics also were noted. In **Paper I**, the subjective image quality analysis using VGC revealed inferior results in the lowest radiation dose group, despite equivalent CNR for all groups. In **Paper III**, the detection rate of the smallest lesions diminished in the lowest radiation dose images, even when compared to lesions of corresponding size and CNR in higher dose images.

CNR is a standard metric, widely employed in studies comparing image quality of different reconstruction methods or examination protocols. Various calculation methods for CNR exist, with the most clinically relevant approach utilising the contrast of pathological structures intended for detection by the evaluated protocol, such as hepatic lesions. In the absence of lesions, the contrast between the liver and other anatomical structures, such as muscle or subcutaneous fat, can serve as a proxy metric (38,162–164). In **Paper I**, an arbitrarily selected HU-value of 40 was used to simulate a hypovascular metastasis and this value was used in CNR calculations. But even when the CNR is calculated in an optimal way, how well does it correlate with more important image quality metrics, such as lesion detection in a study with human readers? There are many examples demonstrating considerable discrepancies between

CNR and low-contrast lesion detection. Jensen et al, in two different studies, compared detection of liver metastases between standard radiation dose images reconstructed with FBP and images acquired at 54 – 65% reduced dose reconstructed with two different types of IR. Although the mean CNR of metastases was higher in the low dose/IR images, the detection of metastases was superior in full dose FBP images - particularly regarding lesions smaller than 1 cm (165,166). Similar discrepancies were reported by Schindera et al. and Pickhardt et al (167,168).

Another commonly used objective image quality metric, SNR, poses challenges in the context of CT. As the "0" point of the HU scale corresponds to the linear attenuation coefficient of water, which lies within the clinically relevant HU range, the "signal" component of SNR represents the contrast between the measured CT-number and water, rather than the total signal. While this may be a relevant metric, it does not reflect a true signal measurement. The signal perceived by CT image readers corresponds to the greyscale assigned to each voxel on the screen, determined by the measured CT-number and the window level settings of the image reading software. These settings comprise a centre value (the greyscale midpoint) and a width (the total HU range between fully white and fully black). Defining the signal as a greyscale level, the true signal becomes the HU difference between the measured CT-number and the value representing fully black. This signal, divided by the noise, yields the true SNR as perceived by the reader. Although this method could be applied in a fixed research set up, its variation with dynamically adjusted window level settings - common in clinical case reading by human observers - limits its utility in such studies.

The limitations of using CNR and SNR as objective image quality metrics have long been recognised. A key weakness is that neither metric accounts for lesion size. Several decades ago, during the early development of signal detection theory and television broadcasting, Alfred Rose introduced the "Rose model." This model describes the contrast required to detect a signal amidst noise, factoring in the signal's size, with the required contrast being inversely proportional to the diameter of a circular signal area (169). However, this model applies only to uncorrelated noise, often termed "white noise," and is not necessarily applicable to CT imaging, with its more complex NPS. Nonetheless, it provides a valuable conceptual framework, underscoring the significance of lesion size in assessing image quality and optimising imaging protocols - a principle clearly illustrated by the findings in **Papers III** and **IV**. In a study evaluating the impact of an IR algorithm on lesion detection, Solomon et al. introduced the "Rose Model Inspired SNR," calculated by multiplying CNR by the square root of lesion area. This straightforward yet insightful approach demonstrated a stronger correlation with lesion detection accuracy than conventional CNR (160). Goodenough and Weaver, in 1984, posited that low-contrast resolution reflects an interplay of spatial resolution, noise, contrast, and lesion size and shape (170). More recent research into diverse image reconstruction techniques, including non-linear iterative methods, has

introduced further challenges to the utility of CNR and SNR as image quality metrics. As shown in **Paper IV**, the magnitude of image noise, when its texture is disregarded, holds limited relevance for lesion detection when comparing different reconstruction methods. In a report by Task Group 233 of the American Association of Physicists in Medicine (AAPM) titled "Performance evaluation of computed tomography systems," Samei et al. assert that CNR is suitable only for basic analyses of low-contrast lesion detectability, and only when comparing images with consistent noise texture and resolution. They advise against using CNR when comparing different kernels or IR to FBP, as it may produce suboptimal or misleading results (171).

This prompts the question of which metrics are most appropriate for assessing image quality in the context of low-contrast lesion detection. Observer studies, wherein radiologists undertake clinically relevant diagnostic tasks, remain the gold standard (172). However, these studies are time-intensive and susceptible to inter- and intra-observer variability. Moreover, when conducted with patient images, the reliability of the reference standard introduces uncertainty regarding lesion presence. Beyond reader studies, various methods with differing levels of automation are in use or under development. The detectability index (d') quantifies the distinguishability of a signal from background noise, incorporating the task transfer function (TTF), a metric of spatial resolution akin to the MTF, and NPS in CT image analysis. Mathematical model observers, such as the non-prewhitening matched filter or the channelized Hotelling observer, are also employed. As a measure of signal detectability with known properties (e.g., size and contrast), d' has shown close agreement with human reader performance in images reconstructed with FBP and non-linear IR. Such analyses are typically conducted using phantoms, though Smith et al. have proposed and validated a method applicable to patient images. This approach uses AI-based liver segmentation to analyse homogeneous regions, calculating NPS, deriving TTF, and subsequently determining d'. This method demonstrated good concordance with an earlier reader study on the same image dataset (173). In a recent review, Hoeijmakers et al. provide an overview of proposed CT image quality assessment methods, encompassing 35 papers describing methods beyond basic CNR and SNR metrics. These methods analyse noise, contrast, spatial resolution, and other factors, many being automated or AI-based. The authors conclude that a transition to advanced, automated, and AI-driven techniques is underway, though a universally accepted reference standard remains lacking. They advocate for a comprehensive image quality score integrating noise, contrast, and spatial resolution, noting the promising role of convolutional neural networks (CNN) trained on large datasets of subjectively assessed images (172).

In conclusion, CNR and SNR are no longer deemed sufficient metrics for assessing image quality, particularly with respect to low-contrast lesion detection. This perspective is substantiated by the findings in **Paper IV**, alongside indications from **Papers I** and **III**. Several more advanced techniques have been developed; however, no

consensus has emerged regarding the optimal methodologies. CNN-based methods hold considerable promise for the future, yet they require training on extensive datasets of images evaluated by human readers, a process that will be time-intensive to compile. Nonetheless, this represents a critical endeavour, and it may be an appropriate focus for radiologists at academic institutions in the near future, especially as the routine interpretation of clinical images in radiology increasingly shifts to other actors. Nevertheless, the inherent conservatism of radiologists and their scepticism toward novel technological advancements suggest that reader-based studies will remain necessary for the foreseeable future. These studies will be essential to validate and progressively enhance confidence in AI-based methods by correlating their outcomes.

Conclusions

Paper I demonstrated that increasing the IV CM dose can compensate for a reduced radiation dose, and vice versa, while preserving CNR and SNR. Subjective image quality was affected by elevated noise levels but remained acceptable for all groups except the one receiving the lowest radiation dose. The discrepancy between objective and subjective image quality may be partly attributable to limitations in the evaluation method, which focused on rating normal anatomical structures. Within the assessed abdominal CT examination protocol, the radiation dose was reduced by 57% for the youngest patients, while the intravenous contrast medium dose was decreased by 18% for the elderly.

In **Paper II**, Ta, W, and Au were effectively separated from iodine by both DE ratios and the image-based MD software, rendering them ideal candidates for dual-CM examinations alongside iodine. Bi, despite its high K-edge, exhibited DE ratios more akin to those of iodine. Nevertheless, it was nearly completely separated from iodine using MD and should also be regarded as a potential, albeit slightly weaker, candidate. Gd proved less suitable due to DE ratios too similar to iodine; however, the use of a lower energy setting of 70 kVp could potentially facilitate its application in dual-CM examinations.

The study in **Paper III** shows non-inferior reader performance regarding detection and characterisation of hypovascular liver metastases at a simulated radiation dose of 8.6 mGy $CTDI_{vol}$, representing 75% of the clinically used standard level. Another complicating and potentially important finding is that characterisation of benign lesions was already negatively affected at DL75, a finding that requires caution due to the limited number of benign lesions included. Additionally, increased image noise disproportionately impaired the detection of small lesions, an effect not fully accounted for by the corresponding reduction in CNR.

In **Paper IV**, a phantom study involving multiple readers demonstrated improved detection of small, low-contrast lesions in low-dose images when utilising a sharper (higher-frequency) reconstruction kernel, with or without IR. The study further suggests that CNR is an unreliable image quality metric and should be applied with caution.

Collectively, the findings in **Papers IV**, **II**, and **I** contribute to the emerging consensus that basic image quality metrics, such as CNR and SNR, are inadequate as proxies for low-contrast lesion detection, particularly when comparing images generated by different reconstruction methods or assessing lesions of varying sizes.

In summary, the results from the four Papers included in this thesis illustrate that abdominal CT examinations can be conducted by balancing the amounts of radiation and contrast media while preserving objective image quality. The detection of liver metastases remains non-inferior with a 25% reduced radiation dose. Collectively, these findings indicate the potential to examine younger patients using lower radiation doses without jeopardising the identification of significant findings. The use of sharper filters in image reconstruction processes may further improve diagnostic image quality. CNR and SNR are inadequate metrics for assessing image quality. Finally, the elements Ta, W, and Au are optimal candidates for incorporation into future contrast media alongside existing iodine-based contrast agents.

Författarens tack!

Min huvudhandledare Peter Leander. Tack för att du trodde på mig och gav mig chansen att påbörja denna resa - och nog ännu större tack för ditt tålamod, när vägen varit slingrig och ibland nästan förlorad. Vi nådde fram till slut!

Världens bästa bihandledare, Marcus Söderberg! En mera positiv, omtänksam, handlingskraftig och noggrann kamrat att arbeta med kan man inte finna. Bra att du inte lät mig ge upp när det var nära. Hoppas vi fortsätter samarbeta, annars kommer jag sakna din intresserade och samtidigt små-skeptiska blick när jag försöker förklara min senaste, halvt genomtänkta idé.

Kasim Abul-Kasim och Mikael Gunnarsson, bihandledare på delar av resan, Tack!

Alla medförfattare och bildgranskare i mina delarbeten. Ni har varit otroligt tappra när ni kämpat er igenom hundratals bilder av ”ingenting”. Det finns många gentjänster att inkassera här.

Peter Hochbergs, verksamhetschef på Bild och Funktion och Lars Bååth, tidigare chef i Malmö - tack för att ni gett mig möjlighet och utrymme att genomföra detta doktorandprojekt!

Professorerna Olle Ekberg och Sophia Zackrisson. Olle, du är ett föredöme, i forskning och vetenskap, men i ännu högre grad genom din uppenbara kärlek till det kliniska arbetet. På sistone dessutom rumskompis! Sophia, en otrolig forskare, men minst lika bra i det lilla sammanhanget. Dina försiktigt påhejande kommentarer hjälpte verkligen när ambitionen sviktade.

Daisy Lee, min närmsta chef och din föregångare Carin Cronberg, tack för all energi ni lagt på att få Gastrosektionen att fungera så bra som möjligt. Ni har båda en drivkraft att inspireras av.

Kollegor på Gastrosektionen, nuvarande och tidigare. Vi har en fin arbetsplats, med hur mycket spännande arbete som helst! Jag slutar aldrig fascineras över hur många intressanta, briljanta personer som korsar ens väg. Ni som för tillfället jobbar någon annanstans - kom tillbaka!

Alla medarbetare på Bild och Funktion och Diagnostisk radiologi. Det är ni som gör att jag trivs så bra på mitt jobb. God stämning sitter inte i väggarna, den skapar vi tillsammans varje dag.

Anders Berg, du fick en AT-läkare med oklara framtidsplaner att inse var man skall jobba. Ingen kan blanda högsta kompetens, skoj, effektivt arbete och fika som du. Ett föredöme.

Jonatan Engman. En gång var vi yngst tillsammans på gastrosektionen, nu kanske medelålders-ast. Alltid med en glad, inte sällan retsam, kommentar. Vidare mot pensionen kompis!

Susanna Holst, vi växte upp på samma gata och hamnade i samma röntgengranskning, ganska galet. Ingen har, eller kan formulera sig med, en skärpa som du.

ST-läkarna jag själv handlett på vägen. Maja Ekman, Nicole McMichael, Sampras Senya och Martina Lundh. Ni lärde mig mycket mera än tvärtom.

Torbjörn Ahl, Peter Østergaard och Fredrik Holmquist, tur att det finns fler DT-nördar i Skåne. Ert intresse för ämnet smittar!

Håkan Sjunnesson - Jag blev så glad när du tackade mig för 23 år sedan, så tack själv!

Mina äldsta vänner Anders Jedholt och Efrain Staino. Ni har båda lämnat Skåne bakom er, med olika distans. Även om vi ses sällan, känns det alltid som det var igår. Snacket fortsätter och ni plockar alltid ner mig på jorden igen. Era familjer skall ni vara oerhört stolta över.

Släkten i Skåne och Finland. Kusiner som alltid varit mina extra syskon. Lotta och Kerstin. Svåger och svägerskor i Finland, alla barnen. Ni är en del av mig och jag en del av er.

Matti-Ukki: Kiitos tuesta, saunasta ja oluesta kesän kirjoitusleirillä! Vaikka et fyysisesti voi olla läsnä arjessamme, olet tärkeä ja rakas osa elämäämme. Paljon lämpimiä ajatuksia!

Johan, min storebror. Jag skulle ju gå min egen väg, men sen blev det ändå ”Katte”, läkarlinjen, ett liv tillsammans med en kirurg. Du var nog alltid en större förebild än jag ville erkänna. Din familj med Anna, Elsa och Elof ligger mig otroligt nära hjärtat. Elsa och Elof, att få vara er farbror är en av mina största lyckor.

Lena, min mamma. Ni hittar inte en bättre person, alltid stöttande med oändlig kärlek. Och din självklara uppfattning att alla skall ha det lika bra har format mig. Kämpa på nu!

Forskning och arbete är ganska viktigt, men under min tid som doktorand har på riktigt viktiga händelser ägt rum. Alvar, Frans och Edit har kommit och vänt allting upp och ner och in och ut. Jag skulle inte vilja ha det på något annat vis. Jag älskar er och är så stolt varje dag - må det bli många tillsammans!

Ursula, en gång pendlarkompis på Pågatågen och nu mitt Allt! Jag älskar dig och alla delar av vårt liv tillsammans. Tack för allt stöd och allt du gjort, utöver det vanliga, på senaste tiden

Figure 41 Low contrast subjects
Three low contrast subjects, the author's favourites, against a very grainy background.

References

1. La Riviere PJ, Crawford CR. From EMI to AI: a brief history of commercial CT reconstruction algorithms. Journal of Medical Imaging. 2021;8(05).
2. Beckmann EC. CT scanning the early days. In: British Journal of Radiology. 2006. p. 5–8.
3. Schulz RA, Stein JA, Pelc NJ. How CT happened: the early development of medical computed tomography. Journal of Medical Imaging. 2021;8(05).
4. Jiang Hsieh. CH 1 - Computed Tomography: Principles, Design, Artifacts, and Recent Advances, Third Edition. In: 3rd ed. 2015.
5. Vaughan Christopher L. Imagining the elephant A Biography of Allan MacLeod Cormack. London: Imperial College Press; 2008.
6. Cormack AM. Representation of a function by its line integrals, with some radiological applications. J Appl Phys. 1963;34(9):2722–7.
7. Radon J. Über die Bestimmung von Funktionen durch ihre Integralwerte längs gewisser Mannigfaltigkeiten. Berichte über die Verhandlungen der Königlich-Sächsischen Akademie der Wissenschaften zu Leipzig, Mathematisch-Physische Klasse. 1917;262–77.
8. Gustschin A. Translation: About a Method of Obtaining Volumetric Images by Means of X-ray Radiation. 2020; Available from: http://arxiv.org/abs/2001.03806
9. Bates S, Beckmann L, Thomas A, Waltham R. Godfrey Hounsfield: Intuitive Genius of CT. London: The British Institute of Radiology; 2012.
10. Ramachandran GN. Reconstruction of Substance from Shadow* 1. Mathematical Theory with Application to Three-Dimensional Radiography and Electron Microscopy. 1971.
11. Brownell GL. A History of Positron Imaging [Internet]. 1999 [cited 2025 Aug 24]. Available from: https://websites.umich.edu/~ners580/ners-bioe_481/lectures/pdfs/Brownell1999_historyPET.pdf
12. Hounsfield GN. Computerized transverse axial scanning (tomography): Part I. Description of system. Vol. 46, British Journal of Radiology. 1973.
13. Ambrose J. Computerized transverse axial scanning (tomography): Part 2. Clinical application*. Vol. 46, British Journal of Radiology. 1973.
14. Hsieh J, Flohr T. Computed tomography recent history and future perspectives. Journal of Medical Imaging. 2021;8(05).

15. Dance DR, Christofides S, Maidment ADA, Mclean ID, Ng KH. Diagnostic Radiology Physics: A Handbook for Teachers and Students. Vienna: International Atomic Energy Agency; 2014.
16. Jiang Hsieh. Computed Tomography: Principles, Design, Artifacts, and Recent Advances. In: Third. 2015.
17. Bandyopadhyay P, Segre CU. http://www.csrri.iit.edu/periodic-table.html. Mucal Periodic Table.
18. Flohr T, Ulzheimer S, Petersilka M, Schmidt B. Basic principles and clinical potential of photon-counting detector CT. Vol. 3, Chinese Journal of Academic Radiology. Springer; 2020. p. 19–34.
19. Nakamura Y, Higaki T, Kondo S, Kawashita I, Takahashi I, Awai K. An introduction to photon-counting detector CT (PCD CT) for radiologists. Jpn J Radiol. 2023;41(3):266–82.
20. Geyer LL, Schoepf UJ, Meinel FG, Nance JW, Bastarrika G, Leipsic JA, et al. State of the Art: Iterative CT reconstruction techniques1. Vol. 276, Radiology. Radiological Society of North America Inc.; 2015. p. 339–57.
21. Hsieh J. Computed Tomography Principles, Design, Artifacts, and Recent Developments. Bellingham, Washington: SPIE; 2022.
22. Seeram E. Computed Tomography Physical Principles, Clinical Applications, and Quality Control. Fourth. Elsevier; 2016.
23. Toda H. X-Ray CT. Singapore: Springer Nature; 2021.
24. Schofield R, King L, Tayal U, Castellano I, Stirrup J, Pontana F, et al. Image reconstruction: Part 1 – understanding filtered back projection, noise and image acquisition. J Cardiovasc Comput Tomogr. 2020;14(3):219–25.
25. Beister M, Kolditz D, Kalender WA. Iterative reconstruction methods in X-ray CT. Vol. 28, Physica Medica. 2012. p. 94–108.
26. Mohammadinejad P, Mileto A, Yu L, Leng S, Guimaraes LS, Missert AD, et al. Ct noise-reduction methods for lower-dose scanning: Strengths and weaknesses of iterative reconstruction algorithms and new techniques. Radiographics. 2021;41(5):1493–508.
27. Tatsugami F, Higaki T, Nakamura Y, Honda Y, Awai K. Dual-energy CT: minimal essentials for radiologists. Vol. 40, Japanese Journal of Radiology. Springer; 2022. p. 547–59.
28. McCollough CH, Leng S, Yu L, Fletcher JG. Dual- and multi-energy CT: Principles, technical approaches, and clinical applications. Radiology. 2015;276(3):637–53.
29. So A, Nicolaou S. Spectral computed tomography: Fundamental principles and recent developments. Vol. 22, Korean Journal of Radiology. Korean Radiological Society; 2021. p. 86–96.
30. Agostini A, Borgheresi A, Mari A, Floridi C, Bruno F, Carotti M, et al. Dual-energy CT: theoretical principles and clinical applications. Vol. 124, Radiologia Medica. Springer; 2019. p. 1281–95.

31. Strauss KJ. Dose indices: everybody wants a number. Vol. 44, Pediatric Radiology. Springer Verlag; 2014. p. 450–9.
32. Hsieh J. Key Performance Parameters of the CT Scanner. In: Computed Tomography Principles, Design, Artifacts and Recent Advances. Third. Bellingham, Washington: SPIE Press; 2015.
33. ICRP. ICRP 103: The 2007 Recommendations of the International Commission on Radiological Protection. Ann ICRP [Internet]. 2007;37:330. Available from: http://ani.sagepub.com/lookup/doi/10.1016/j.icrp.2007.10.001
34. Igarashi K, Imai K, Matsushima S, Yamauchi-Kawaura C, Fujii K. Development and validation of the effective CNR analysis method for evaluating the contrast resolution of CT images. Phys Eng Sci Med. 2024;47(2):717–27.
35. Mori M, Imai K, Ikeda M, Iida Y, Ito F, Yoneda K, et al. Method of measuring contrast-to-noise ratio (CNR) in nonuniform image area in digital radiography. Electronics and Communications in Japan. 2013;96(7):32–41.
36. Bushberg JT, Seibert JA, Leidholdt EMJr, Boone JM. The Essential Physics of Medical Imaging. 4th ed. Philadelphia: Wolters Kluwer; 2021.
37. Verdun FR, Racine D, Ott JG, Tapiovaara MJ, Toroi P, Bochud FO, et al. Image quality in CT: From physical measurements to model observers. Vol. 31, Physica Medica. Associazione Italiana di Fisica Medica; 2015. p. 823–43.
38. Yang S, Bie Y, Pang G, Li X, Zhao K, Zhang C, et al. Impact of novel deep learning image reconstruction algorithm on diagnosis of contrast-enhanced liver computed tomography imaging: Comparing to adaptive statistical iterative reconstruction algorithm. J Xray Sci Technol. 2021;29(6):1009–18.
39. Verdun FR, Racine D, Ott JG, Tapiovaara MJ, Toroi P, Bochud FO, et al. Image quality in CT: From physical measurements to model observers. Vol. 31, Physica Medica. Associazione Italiana di Fisica Medica; 2015. p. 823–43.
40. Båth M, Mansson LG. Visual grading characteristics (VGC) analysis: a non-parametric rank-invariant statistical method for image quality evaluation. British Journal of Radiology [Internet]. 2007;80(951):169–76. Available from: http://bjr.birjournals.org/cgi/doi/10.1259/bjr/35012658
41. Chakraborty DP. New Developments in Observer Performance Methodology in Medical Imaging. Semin Nucl Med. 2011;41(6):401–18.
42. Martinez NE, Jokisch DW, Dauer LT, Eckerman KF, Goans RE, Brockman JD, et al. Radium dial workers: back to the future. Vol. 98, International Journal of Radiation Biology. Taylor and Francis Ltd.; 2022. p. 750–68.
43. Ozasa K, Shimizu Y, Suyama A, Kasagi F, Soda M, Grant EJ, et al. Studies of the mortality of atomic bomb survivors, report 14, 1950-2003: An overview of cancer and noncancer diseases. Vol. 177, Radiation Research. 2012. p. 229–43.
44. Douple EB, Mabuchi K, Cullings HM, Preston DL, Kodama K, Shimizu Y, et al. Long-term radiation-related health effects in a unique human population: Lessons learned from the atomic bomb survivors of Hiroshima and nagasaki. Vol. 5, Disaster Medicine and Public Health Preparedness. 2011.

45. Wakeford R. What about the workers? Vol. 44, Journal of Radiological Protection. Institute of Physics; 2024.
46. Leuraud K, Richardson DB, Cardis E, Daniels RD, Gillies M, O'Hagan JA, et al. Ionising radiation and risk of death from leukaemia and lymphoma in radiation-monitored workers (INWORKS): An international cohort study. Lancet Haematol. 2015;2(7):e276–81.
47. Richardson DB, Leuraud K, Laurier D, Gillies M, Haylock R, Kelly-Reif K, et al. Cancer mortality after low dose exposure to ionising radiation in workers in France, the United Kingdom, and the United States (INWORKS): Cohort study. BMJ. 2023;
48. Shore RE, Beck HL, Boice JD, Caffrey EA, Davis S, Grogan HA, et al. Implications of recent epidemiologic studies for the linear nonthreshold model and radiation protection. Vol. 38, Journal of Radiological Protection. Institute of Physics Publishing; 2018. p. 1217–33.
49. Unscear. Volume III SCIENTIFIC ANNEX C: Biological mechanisms relevant for the inference of cancer risks from low-dose and low-dose-rate radiation. New York; 2021 Dec.
50. Laurier D, Billarand Y, Klokov D, Leuraud K. The scientific basis for the use of the linear no-threshold (LNT) model at low doses and dose rates in radiological protection. Vol. 43, Journal of Radiological Protection. Institute of Physics; 2023.
51. Siegel JA, Welsh JS. Does Imaging Technology Cause Cancer? Debunking the Linear No-Threshold Model of Radiation Carcinogenesis. Technol Cancer Res Treat. 2016;15(2):249–56.
52. Siegel JA, Greenspan BS, Maurer AH, Taylor AT, Phillips WT, Van Nostrand D, et al. The BEIR VII estimates of low-dose radiation health risks are based on faulty assumptions and data analyses: A call for reassessment. Journal of Nuclear Medicine. 2018;59(7):1017–9.
53. Tubiana M. Dose-effect relationship and estimation of the carcinogenic effects of low doses of ionizing radiation: The joint report of the Académie des Sciences (Paris) and of the Académie Nationale de Médecine. Vol. 63, International Journal of Radiation Oncology Biology Physics. Elsevier Inc.; 2005. p. 317–9.
54. Clement C. H. ICRP, 20xx. Scientific evidence relevant to the assessment of solid cancer radiation risk at low dose and low dose rate. ICRP Publication XXX. Ann. ICRP xx(x). ICRP ref: 4904-3744-8231 [Internet]. 2025 [cited 2025 Jul 17]. Available from: https://www.icrp.org/docs/TG91%20Report%20for%20public%20consultation%20final.docx
55. Pearce MS, Salotti J a, Little MP, McHugh K, Lee C, Kim KP, et al. Radiation exposure from CT scans in childhood and subsequent risk of leukaemia and brain tumours: a retrospective cohort study. Lancet. 2012;380(9840):499–505.
56. Pearce MS, Salotti JA, Little MP, McHugh K, Lee C, Kim KP, et al. Radiation exposure from CT scans in childhood and subsequent risk of leukaemia and brain tumours: A retrospective cohort study. The Lancet. 2012;380(9840):499–505.

57. Bonnemain B. History of Contrast Media: Celebrating the Centenary of the Use of Lipiodol in Radiology. Erciyes Medical Journal. 2021;
58. Pollack H M. History of iodinated contrast media. In: Thomsen HS, Muller RN, Mattrey RF, editors. Trends in Contrast Media. 1st ed. Heidelberg: Springer; 1999. p. 3–20.
59. Nyman U, Ekberg O, Aspelin P. Torsten Almén (1931-2016): The father of non-ionic iodine contrast media. Acta radiol. 2016;57(9):1072–8.
60. Katayama H, Yamaguchi K, Takahiro K, Tsutomu T, Seez P, Keiichi M. Adverse Reactions to Ionic and Nonionic Contrast Media - A Report from the Japanese Committee on the Safety of Contrast Media. Radiology. 1990;175(3):621–8.
61. Barrett BJ. Metaanalysis ofthe Relative Nephrotoxicity oflligh-and Low-Osmolality lodinated Contrast Media' Contrast Media.
62. Bednarczuk T, Brix TH, Schima W, Zettinig G, Kahaly GJ. 2021 European Thyroid Association Guidelines for the Management of Iodine-Based Contrast Media-Induced Thyroid Dysfunction. Vol. 10, European Thyroid Journal. S. Karger AG; 2021. p. 269–84.
63. Chiu TM, Chu SY. Hypersensitivity Reactions to Iodinated Contrast Media. Vol. 10, Biomedicines. MDPI; 2022.
64. Kormano M, Dean PB. Extravascular Contrast Material: The Major Component of Contrast Enhancement 1.
65. Breziz M, Greenfeld Z, Herman M, Meyer J. J, Heyman S. N, Rosen S. Experimental Nephrotoxicity of the Radiocontrast Agents Iohexol, Ioxaglate, and Iothalamate - An In Vitro and In Vivo Study. Invest Radiol. 1991;
66. Bae H, Oh H, Park G Bin, Chung YE. Safety of Administering Intravenous CT Contrast Agents Repeatedly or Using Both CT and MRI Contrast Agents on the Same Day: An Animal Study. Korean J Radiol. 2024;25(3):257–66.
67. Deray G, Dubois M, Martinez F, Baumelou B, Beaufils H, Bourbouze R, et al. Renal Effects of Radiocontrast Agents in Rats: A New Model of Acute Renal Failure. Am J Nephrol. 1990;10(6):507–13.
68. Byrd L, Sherman RL. Radiocontrast-Induced Acute Renal Failure: A Clinical and Pathophysiological Review. Medicine. 1979;58(3):270–9.
69. Byrd LH. Computerized Tomography-Induced Acute Renal Failure. Arch Intern Med. 1979;139(4):491.
70. Rao QA, Newhouse JH. Risk of nephropathy after intravenous administration of contrast material: A critical literature analysis. Vol. 239, Radiology. 2006. p. 392–7.
71. Stacul F, Van Der Molen AJ, Reimer P, Webb J a W, Thomsen HS, Morcos SK, et al. Contrast induced nephropathy: Updated ESUR Contrast Media Safety Committee guidelines. Eur Radiol. 2011;21(12):2527–41.
72. Svensk urogenitalradiologisk förenings kontrastmedelsgrupp. Nationella rekommendationer, Jodkontrast, Version 7.2. 2025 Mar.

73. Kidney Disease: Improving Global Outcomes (KDIGO) CKD Work Group. KDIGO 2024 Clinical Practice Guideline for the Evaluation and Management of Chronic Kidney Disease. Kidney Int. 2024;105(4):A1.
74. Kellum JA, Lameire N, Aspelin P, Barsoum RS, Burdmann EA, Goldstein SL, et al. Kidney disease: Improving global outcomes (KDIGO) acute kidney injury work group. KDIGO clinical practice guideline for acute kidney injury. Vol. 2, Kidney International Supplements. Nature Publishing Group; 2012. p. 1–138.
75. Jost G, McDermott M, Gutjahr R, Nowak T, Schmidt B, Pietsch H. New Contrast Media for K-Edge Imaging with Photon-Counting Detector CT. Vol. 58, Investigative Radiology. Lippincott Williams and Wilkins; 2023. p. 515–22.
76. Bandyopadhyay P, Segre C. Mucal on the web [Internet]. [cited 2025 Aug 24]. Available from: http://www.csrri.iit.edu/mucal.html
77. CIAAW Radioactive elements - https://ciaaw.org/radioactive-elements.htm.
78. Yu SB, Watson AD. Metal-Based X-ray Contrast Media. Chem Rev. 1999;99(9):2353–78.
79. Frenzel T, Bauser M, Berger M, Hilger CS, Hegele-Hartung C, Jost G, et al. Characterization of a Novel Hafnium-Based X-ray Contrast Agent. Invest Radiol. 2016;51(12):776–85.
80. Mongan J, Wang R, Jones EF, Yeh BM. In Vivo Differentiation of Complementary Contrast Media. Radiology. 2012;265(1):267–72.
81. Qu M, Ehman E, Fletcher JG, Huprich JE, Hara AK, Silva AC, et al. Toward biphasic computed tomography (CT) enteric contrast: material classification of luminal bismuth and mural iodine in a small-bowel phantom using dual-energy CT. J Comput Assist Tomogr. 2012;36(5):554–9.
82. Yeh BM, FitzGerald PF, Edic PM, Lambert JW, Colborn RE, Marino ME, et al. Opportunities for new CT contrast agents to maximize the diagnostic potential of emerging spectral CT technologies. Vol. 113, Advanced Drug Delivery Reviews. Elsevier B.V.; 2017. p. 201–22.
83. Söderberg M, Gunnarsson M, Nilsson M. Simulated dose reduction by adding artificial noise to measured raw data: Avalidation study. Radiat Prot Dosimetry. 2010;139(1–3):71–7.
84. European_Guidelines_Quality_Criteria_Computed_Tomography_Eur_16252.
85. Båth M, Hansson J. VGC analyzer: A software for statistical analysis of fully crossed multiple-reader multiple-case visual grading characteristics studies. Radiat Prot Dosimetry. 2016;169(1):46–53.
86. Chakraborty DP. Analysis of Location Specific Observer Performance Data : Validated Extensions of the Jackknife Free-Response (JAFROC) Method 1. 2006;1187–93.
87. Chakraborty DP, Yoon H jun. JAFROC analysis revisited : figure-of-merit considerations for human observer studies. 2009;7263:1–12.
88. Hillis SL, Schartz KM. Multireader sample size program for diagnostic studies: demonstration and methodology. Journal of Medical Imaging. 2018;5(04):1.

89. Kirkwood BR, Sterne JAC. Essential Medical Statistics. Second. Malden, Ma: Blackwell Publishing company; 2003.
90. Koo TK, Li MY. A Guideline of Selecting and Reporting Intraclass Correlation Coefficients for Reliability Research. J Chiropr Med. 2016;15(2):155–63.
91. Hallgren KA. Computing Inter-Rater Reliability for Observational Data: An Overview and Tutorial. Tutor Quant Methods Psychol. 2012;8(1):23–34.
92. Brady Z, Forsythe A, McBain-Miller J, Scurrah KJ, Smoll N, Lin Y, et al. Ct dosimetry for the australian cohort data linkage study. Radiat Prot Dosimetry. 2020;191(4):423–38.
93. Thierry-Chef I, Ferro G, Le Cornet L, Dabin J, Istad TS, Jahnen A, et al. Dose estimation for the european epidemiological study on pediatric computed tomography (EPI-CT). Radiat Res. 2021;196(1):74–99.
94. Smoll NR, Brady Z, Scurrah KJ, Lee C, De González AB, Mathews JD. Computed tomography scan radiation and brain cancer incidence. Neuro Oncol. 2023;25(7):1368–76.
95. Mathews JD, Forsythe A V., Brady Z, Butler MW, Goergen SK, Byrnes GB, et al. Cancer risk in 680 000 people exposed to computed tomography scans in childhood or adolescence: Data linkage study of 11 million Australians. BMJ (Online). 2013;346(7910).
96. Huang WY, Muo CH, Lin CY, Jen YM, Yang MH, Lin JC, et al. Paediatric head CT scan and subsequent risk of malignancy and benign brain tumour: A nation-wide population-based cohort study. Br J Cancer. 2014;110(9):2354–60.
97. Li IG, Yang YH, Li YT, Tsai YH. Paediatric computed tomography and subsequent risk of leukaemia, intracranial malignancy and lymphoma: a nationwide population-based cohort study. Sci Rep. 2020;10(1).
98. Meulepas JM, Ronckers CM, Smets AMJB, Nievelstein RAJ, Gradowska P, Lee C, et al. Radiation exposure from pediatric CT scans and subsequent cancer risk in the Netherlands. J Natl Cancer Inst. 2019;111(3):256–63.
99. Foucault A, Ancelet S, Dreuil S, Caër-Lorho S, Ducou Le Pointe H, Brisse H, et al. Childhood cancer risks estimates following CT scans: an update of the French CT cohort study. Eur Radiol. 2022;32:5491–8.
100. Krille L, Dreger S, Schindel R, Albrecht T, Asmussen M, Barkhausen J, et al. Risk of cancer incidence before the age of 15 years after exposure to ionising radiation from computed tomography: results from a German cohort study. Radiat Environ Biophys. 2015;54(1):1–12.
101. Bernier MO, Baysson H, Pearce MS, Moissonnier M, Cardis E, Hauptmann M, et al. Cohort profile: The EPI-CT study: A European pooled epidemiological study to quantify the risk of radiation-induced cancer from paediatric CT. Int J Epidemiol. 2019;48(2):379–381g.
102. Bosch de Basea Gomez M, Thierry-Chef I, Harbron R, Hauptmann M, Byrnes G, Bernier MO, et al. Risk of hematological malignancies from CT radiation exposure in children, adolescents and young adults. Nat Med. 2023;29(12):3111–9.

103. Hauptmann M, Byrnes G, Cardis E, Bernier MO, Blettner M, Dabin J, et al. Brain cancer after radiation exposure from CT examinations of children and young adults: results from the EPI-CT cohort study. Lancet Oncol. 2023;24(1):45–53.
104. Lubin JH, Adams MJ, Shore R, Holmberg E, Schneider AB, Hawkins MM, et al. Thyroid cancer following childhood low-dose radiation exposure: A pooled analysis of nine cohorts. Journal of Clinical Endocrinology and Metabolism. 2017;102(7):2575–83.
105. Hauptmann M, Daniels RD, Cardis E, Cullings HM, Kendall G, Laurier D, et al. Epidemiological studies of low-dose ionizing radiation and cancer: Summary bias assessment and meta-analysis. J Natl Cancer Inst Monogr. 2020;2020(56):188–200.
106. Berrington A, Gonzalez DE, Pasqual E, Veiga L. Epidemiological studies of CT scans and cancer risk: the state of the science. 2021.
107. Gale RP. Radiation and leukaemia: Which leukaemias and what doses? Vol. 58, Blood Reviews. Churchill Livingstone; 2023.
108. Brambilla M, Vassileva J, Kuchcinska A, Rehani MM. Multinational data on cumulative radiation exposure of patients from recurrent radiological procedures: call for action. Eur Radiol. 2020;30(5):2493–501.
109. Bellamy M, Eckerman K. Relative Biological Effectiveness of Low-Energy Electron and Photons. 2013.
110. Nikjoo H, Lindborg L. RBE of low energy electrons and photons. Vol. 55, Physics in Medicine and Biology. 2010.
111. Freneau A, Dos Santos M, Voisin P, Tang N, Bueno Vizcarra M, Villagrasa C, et al. Relation between DNA double-strand breaks and energy spectra of secondary electrons produced by different X-ray energies. Int J Radiat Biol. 2018;94(12):1075–84.
112. Yachi Y, Yoshii Y, Matsuya Y, Mori R, Oikawa J, Date H. Track Structure Study for Energy Dependency of Electrons and X-rays on DNA Double-Strand Break Induction. Sci Rep. 2019;9(1).
113. Eurostat. https://ec.europa.eu/eurostat/statistics-explained/index.php?title=Healthcare_resource_statistics_-_technical_resources_and_medical_technology.
114. EPA. https://www.epa.gov/radiation/radiation-sources-and-doses.
115. Ståhlbrandt H, Björnfot I, Cederlund T, Almén A. CT and MRI imaging in Sweden: retrospective appropriateness analysis of large referral samples. Insights Imaging. 2023;14(1).
116. Baek S, Park SH, Won E, Park YR, Kim HJ. Propensity score matching: A conceptual review for radiology researchers. Vol. 16, Korean Journal of Radiology. Korean Radiological Society; 2015. p. 286–96.
117. Benedetto U, Head SJ, Angelini GD, Blackstone EH. Statistical primer: Propensity score matching and its alternatives. Vol. 53, European Journal of Cardio-thoracic Surgery. European Association for Cardio-Thoracic Surgery; 2018. p. 1112–7.

118. McDonald RJ, McDonald JS, Kallmes DF, Carter RE. Behind the numbers: Propensity score analysis-a primer for the diagnostic radiologist. Vol. 269, Radiology. 2013. p. 640–5.
119. D'agostino RB. Estimating Treatment Effects Using Observational Data.
120. Reiffel JA. Propensity Score Matching: The 'Devil is in the Details' Where More May Be Hidden than You Know. Vol. 133, American Journal of Medicine. Elsevier Inc.; 2020. p. 178–81.
121. Davenport MS, Khalatbari S, Dillman JR, Cohan RH, Caoili EM, Ellis JH. Contrast material-induced nephrotoxicity and intravenous low-osmolality iodinated contrast material. Radiology. 2013;267(1):94–105.
122. Mcdonald RJ, Mcdonald JS, Bida JP, Carter RE, Fleming CJ, Misra S, et al. Intravenous Contrast Material-induced Nephropathy: Causal or Coincident Phenomenon? radiology.rsna.org n Radiology. 2013;267.
123. Choi B, Heo S, McDonald JS, Choi SH, Choi WM, Lee JB, et al. Risk of Contrast-Induced Acute Kidney Injury in Computed Tomography A 16 Institutional Retrospective Cohort Study. Invest Radiol. 2024;
124. Lee CC, Chan YL, Wong YC, Ng CJ, Chang CH, Hung CC, et al. Contrast-enhanced CT and Acute Kidney Injury: Risk Stratification by Diabetic Status and Kidney Function. Radiology. 2023;307(5).
125. McDonald JS, McDonald RJ, Carter RE, Katzberg RW, Kallmes DF, Williamson EE. Risk of intravenous contrast material-mediated acute kidney injury: A propensity score-matched study stratified by baseline-estimated glomerular filtration rate. Radiology. 2014;271(1):65–73.
126. McDonald RJ, McDonald JS, Carter RE, Hartman RP, Katzberg RW, Kallmes DF, et al. Intravenous contrast material exposure is not an independent risk factor for dialysis or mortality. Radiology. 2014;273(3):714–25.
127. Hinson JS, Ehmann MR, Fine DM, Fishman EK, Toerper MF, Rothman RE, et al. Risk of Acute Kidney Injury After Intravenous Contrast Media Administration. Ann Emerg Med. 2017;69(5):577-586.e4.
128. Ehmann MR, Mitchell J, Levin S, Smith A, Menez S, Hinson JS, et al. Renal outcomes following intravenous contrast administration in patients with acute kidney injury: a multi-site retrospective propensity-adjusted analysis. Intensive Care Med. 2023;49(2):205–15.
129. Su TH, Hsieh CH, Chan YL, Wong YC, Kuo CF, Li CH, et al. Intravenous ct contrast media and acute kidney injury: A multicenter emergency department-based study. Radiology. 2021;301(3):571–81.
130. Gorelik Y, Bloch-Isenberg N, Heyman SN, Khamaisi M. Renal Functional Recovery Confounding the Assessment of Contrast Nephropathy: Propensity Score Analysis. Am J Nephrol. 2021;52(1):76–83.
131. Harrison LL, Kouli O, Geddes CC, Stoumpos S. Intravenous contrast exposure in stable CKD 4 and 5 patients and adverse renal outcomes: a propensity-score matched study.

132. Kene M, Arasu VA, Mahapatra AK, Huang J, Reed ME. Acute kidney injury after ct in emergency patients with chronic kidney disease: A propensity score-matched analysis. Western Journal of Emergency Medicine. 2021;22(3):614–22.
133. Obed M, Gabriel MM, Dumann E, Vollmer Barbosa C, Weißenborn K, Schmidt BMW. Risk of acute kidney injury after contrast-enhanced computerized tomography: a systematic review and meta-analysis of 21 propensity score–matched cohort studies. Vol. 32, European Radiology. Springer Science and Business Media Deutschland GmbH; 2022. p. 8432–42.
134. Aycock RD, Westafer LM, Boxen JL, Majlesi N, Schoenfeld EM, Bannuru RR. Acute Kidney Injury After Computed Tomography: A Meta-analysis. Vol. 71, Annals of Emergency Medicine. Mosby Inc.; 2018. p. 44-53.e4.
135. Miyamoto Y, Iwagami M, Aso S, Yasunaga H, Matsui H, Fushimi K, et al. Association between intravenous contrast media exposure and non-recovery from dialysis-requiring septic acute kidney injury: a nationwide observational study. Intensive Care Med. 2019;45(11):1570–9.
136. Yan P, Zhang NY, Luo XQ, Wang M, Deng YH, Wu T, et al. Is intravenous iodinated contrast medium administration really harmful in hospitalized acute kidney injury patients: a propensity score-matched study. Eur Radiol. 2021;32:1163–72.
137. Latcha S, Plodkowski AJ, Zheng J, Jaimes EA. Rate and risk factors for AKI after CT scans in a cancer cohort. Clin Nephrol. 2019;91(3):147–54.
138. Williams LMS, Walker GR, Loewenherz JW, Gidel LT. Association of Contrast and Acute Kidney Injury in the Critically Ill: A Propensity-Matched Study. In: Chest. Elsevier Inc; 2020. p. 866–76.
139. Caspi O, Habib M, Cohen Y, Kerner A, Roguin A, Abergel E, et al. Acute Kidney Injury After Primary Angioplasty: Is Contrast-Induced Nephropathy the Culprit? J Am Heart Assoc. 2017;6(6).
140. Camera L, Romano F, Liccardo I, Liuzzi R, Imbriaco M, Mainenti PP, et al. Balancing Radiation and Contrast Media Dose in Single-Pass Abdominal Multidetector CT. Acad Radiol. 2015;
141. Martens B, Jost G, Mihl C, Nijssen EC, Wildberger JE, Schmidt B, et al. Individualized Scan Protocols in Abdominal Computed Tomography: Radiation Versus Contrast Media Dose Optimization. Invest Radiol. 2022;57(6):353–8.
142. Greffier J, Viry A, Robert A, Khorsi M, Si-Mohamed S. Photon-counting CT systems: A technical review of current clinical possibilities. Vol. 106, Diagnostic and Interventional Imaging. Elsevier Masson s.r.l.; 2025. p. 53–9.
143. Rathnayake S, Mongan J, Torres AS, Colborn R, Gao DW, Yeh BM, et al. In vivo comparison of tantalum, tungsten, and bismuth enteric contrast agents to complement intravenous iodine for double-contrast dual-energy CT of the bowel. Contrast Media Mol Imaging. 2016;11(4):254–61.
144. Ren L, Rajendran K, McCollough CH, Yu L. Quantitative accuracy and dose efficiency of dual-contrast imaging using dual-energy CT: a phantom study. Med Phys. 2020;47(2):441–56.

145. Soesbe TC, Lewis MA, Nasr K, Ananthakrishnan L, Lenkinski RE. Separating High-Z Oral Contrast From Intravascular Iodine Contrast in an Animal Model Using Dual-Layer Spectral CT. Acad Radiol. 2019;26(9):1237–44.
146. Kim J, Bar-Ness D, Si-Mohamed S, Coulon P, Blevis I, Douek P, et al. Assessment of candidate elements for development of spectral photon-counting CT specific contrast agents. Sci Rep. 2018;8(1).
147. Zhang Y, Deng J, Lang M, Shu G, Pan J, Zhang C, et al. Large-scale synthesis of non-ionic bismuth chelate for computed tomography imaging in vivo. Biomaterials. 2025;318.
148. Heimer MM, Sun Y, Bonitatibus PJ, Luitjens J, Hong CW, Okwelogu N, et al. Performance of an Intravascular Tantalum Oxide–Based Nanoparticle Computed Tomography Contrast Agent in Preclinical Hepatic Tumor Detection. Invest Radiol. 2025;
149. Sartoretti T, Mcdermott MC, Stammen L, Martens B, Moser LJ, Jost G, et al. Tungsten-Based Contrast Agent for Photon-Counting Detector CT Angiography in Calcified Coronaries: Comparison to Iodine in a Cardiovascular Phantom. Invest Radiol. 2024;59(10):677–83.
150. Maurer CJ, Berlis A, Stangl FJ, Behrens L. In Vivo Discrimination of Iodine and Tantalum-Based Liquid Embolics After Intracranial or Spinal Embolization Using Photon-Counting Detector CT. Clin Neuroradiol. 2025;
151. Symons R, Krauss B, Sahbaee P, Cork TE, Lakshmanan MN, Bluemke DA, et al. Photon-counting CT for simultaneous imaging of multiple contrast agents in the abdomen: An in vivo study. Med Phys. 2017;44(10):5120–7.
152. Chakraborty DP, Berbaum KS. Observer studies involving detection and localization : Modeling , analysis ,. Med Phys. 2004;31(8):2313–30.
153. Kaltenbach TEM, Engler P, Kratzer W, Oeztuerk S, Seufferlein T, Haenle MM, et al. Prevalence of benign focal liver lesions: ultrasound investigation of 45,319 hospital patients. Abdominal Radiology. 2016;41(1):25–32.
154. Winslow J, Zhang Y, Samei E. A method for characterizing and matching CT image quality across CT scanners from different manufacturers: Med Phys. 2017;44(11):5705–17.
155. Sugisawa K, Ichikawa K, Urikura A, Minamishima K, Masuda S, Hoshino T, et al. Spatial resolution compensation by adjusting the reconstruction kernels for iterative reconstruction images of computed tomography. Physica Medica. 2020;74:47–55.
156. Robins M, Solomon J, Richards T, Samei E. 3D task-transfer function representation of the signal transfer properties of low-contrast lesions in FBP- and iterative-reconstructed CT. Med Phys. 2018;45(11):4977–85.
157. Bujila R, Fransson A, Poludniowski G. Practical approaches to approximating MTF and NPS in CT with an example application to task-based observer studies. Physica Medica. 2017;33:16–25.

158. Solomon J, Lyu P, Marin D, Samei E. Noise and spatial resolution properties of a commercially available deep learning-based CT reconstruction algorithm. Med Phys. 2020;47(9):3961–71.

159. Greffier J, Frandon J, Larbi A, Beregi JP, Pereira F. CT iterative reconstruction algorithms: a task-based image quality assessment. Eur Radiol. 2020;30(1):487–500.

160. Solomon J, Mileto A, Ramirez-Giraldo JC, Samei E. Diagnostic Performance of an Advanced Modeled Iterative Reconstruction Algorithm for Low-Contrast Detectability with a Third-Generation Dual-Source Multidetector CT Scanner: Potential for Radiation Dose Reduction in a Multireader Study. Radiology. 2015;275(3):735–45.

161. Solomon J, Wilson J, Samei E. Characteristic image quality of a third generation dual-source MDCT scanner: Noise, resolution, and detectability. Med Phys. 2015;42(8):4941–53.

162. Park J, Shin J, Min IK, Bae H, Kim YE, Chung YE. Image Quality and Lesion Detectability of Lower-Dose Abdominopelvic CT Obtained Using Deep Learning Image Reconstruction. Korean J Radiol. 2022;23(4):402–12.

163. Caruso D, De Cecco CN, Schoepf UJ, Schaefer AR, Leland PW, Johnson D, et al. Can dual-energy computed tomography improve visualization of hypoenhancing liver lesions in portal venous phase? Assessment of advanced image-based virtual monoenergetic images. Clin Imaging. 2017;41:118–24.

164. Kanan A, Pereira B, Hordonneau C, Cassagnes L, Pouget E, Tianhoun LA, et al. Deep learning CT reconstruction improves liver metastases detection. Insights Imaging. 2024;15(1).

165. Jensen CT, Wagner-Bartak NA, Vu LN, Liu X, Raval B, Martinez D, et al. Detection of Colorectal Hepatic Metastases Is Superior at Standard Radiation Dose CT versus Reduced Dose CT. Radiology [Internet]. 2019;290(2):400–9. Available from: http://pubs.rsna.org/doi/10.1148/radiol.2018181657

166. Jensen CT, Gupta S, Saleh MM, Liu X, Wong VK, Salem U, et al. Reduced-Dose Deep Learning Reconstruction for Abdominal CT of Liver Metastases. Radiology. 2022;303(1):90–8.

167. Schindera ST, Odedra D, Raza SA, Kim TK, Jang HJ, Szucs-Farkas Z, et al. Iterative Reconstruction Algorithm for CT : Can Radiation Dose Be Decreased While Low-Contrast Detectability Is Preserved? Radiology. 2013;269(2):511–8.

168. Pickhardt PJ, Lubner MG, Kim DH, Ruma JA, Muñoz A, Chen G hong, et al. Abdominal CT With Model-Based Iterative Reconstruction (MBIR): Initial Results of a Prospective Trial Comparing Ultralow-Dose With Standard-Dose Imaging. American Journal of Roentgenology. 2012;199(6):1266–74.

169. Burgess AE. The Rose model, revisited. J Opt Soc Am. 1999;16(3):633–46.

170. Goodenough DJ, Weaver KE. Factors related to low contrast resolution in CT scanners. Computerized Radiology. 1984;8(5):297–308.

171. Samei E, Bakalyar D, Boedeker KL, Brady S, Fan J, Leng S, et al. Performance evaluation of computed tomography systems: Summary of AAPM Task Group 233. Med Phys. 2019;46(11):e735–56.

172. Hoeijmakers EJI, Martens B, Wildberger JE, Flohr TG, Jeukens CRLPN. Objective assessment of diagnostic image quality in CT scans: what radiologists and researchers need to know. Vol. 16, Insights into Imaging. Springer Science and Business Media Deutschland GmbH; 2025.
173. Smith TB, Abadi E, Solomon J, Samei E. Development, validation, and relevance of in vivo low-contrast task transfer function to estimate detectability in clinical CT images. Med Phys. 2021;48(12):7698–711.

Printed by Media-Tryck, Lund 2025 NORDIC SWAN ECOLABEL 3041 0903

About the author

Tobias Aho Fält is a radiologist, working mainly with gastrointestinal and abdominal radiology, at Skåne Univerity Hospital.

LUND UNIVERSITY

FACULTY OF MEDICINE

Department of Translational Medicine

Lund University, Faculty of Medicine
Doctoral Dissertation Series 2025:110
ISBN 978-91-8021-763-7
ISSN 1652-8220